

**DIRECT GROWTH OF  $\text{Hg}_{1-x}\text{Cd}_x\text{Te}$  BY COLD  
WALL, PYROLYTIC OMVPE**

SukRyong Hahn

B.S., Chonnam National University, Korea, 1981

M.S., Chonnam National University, Korea, 1983

A dissertation submitted to the faculty of the  
Oregon Graduate Institute of Science & Technology  
in partial fulfillment of the  
requirements for the degree of  
Doctor of Philosophy  
in  
Applied Physics

July, 1993

The dissertation "Direct Growth of  $\text{Hg}_{1-x}\text{Cd}_x\text{Te}$  by Cold Wall, Pyrolytic OMVPE" by SukRyong Hahn has been examined and approved by the following Examination Committee:

---

Jim Parsons, Dissertation Advisor  
Associate Professor

---

Reinhart Engelmann  
Professor

---

Anthony Bell  
Associate Professor

---

Jim Gates  
FLIR systems, Inc.

*To my family*

## Acknowledgments

First of all and most of all I would like to thank my advisor, Prof. Jim Parsons, for his guidance, support, understanding, patience and encouragement, which have made my time here fruitful and rewarding. He also has been a best advisor to me in terms of life style and showed me a well established example of healthy and hard-working life.

I deeply thank to professors Reinhart Engelmann, Tony Bell, and Mr. Jim Gates for being members of examination committee.

I wish to take this opportunity to thank Dr. H.R. Vydyanath for his research fund to II-VI OMVPE reactor construction and Hall effect measurements from Aerojet Electronics and to thank Prof. John Abele for his help of Hall effect measurements from Lewis & Clark College. I want to thank FLIR systems, Inc. for financial support to this program. Prof. O.M. Stafsudd of University of California at Los Angeles deserves special thank for measurements of Multiple Angle Incident ellipsometry. Dr. Fred Sun, Chemical and Biological Department of OGI, also deserves special thank for his FTIR measurements.

I would also like to thank Doug. Davis at machine shop, Allan Ryall at scientific glass-blowing shop, Jerry Boehme at electronics shop, and John Hunt for technical support and services.

I extend thanks to my fellow students, H.S. Chen, J. Wu, A.K. Chaddha for their help and friendship, and especially Karen Oatis for revising the manuscript.

I would also like to extend thanks to my former advisor Prof. W.T. Kim, Chonnam National University, Korea, for his constant encouragement during the course of my studies.

I thank my mother and the late my father who are so special in their love, sacrifice and encouragement which have sustained and inspired me. Finally I like to express my thanks to my wife and two boys for their enduring and gracious love. They shared with me all the important moments in my life at OGI.

## Table of Contents

Dedication.....	iii
Acknowledgments.....	iv
List of Figures.....	viii
List of Tables.....	xi
Abstract.....	xii
List of Acronyms.....	xiv
1. Introduction.....	1
2. Background of $\text{Hg}_{1-x}\text{Cd}_x\text{Te}$	
2.1 Physical Properties.....	5
2.2 Crystal Growth Techniques of $\text{Hg}_{1-x}\text{Cd}_x\text{Te}$	
2.2.1 Bulk Crystals.....	16
2.2.2 Epitaxial Layers.....	20
2.2.3 OMVPE.....	23
3. II-VI OMVPE System and ARIIV Reactor Design	
3.1 OMVPE system.....	29
3.2 ARIIV Reactor Design.....	33
3.3 Inverted-Vertical Reactor Design Purpose and Function.....	41
4. Growth and Characterization Procedures	
4.1 Substrate and Epilayers Growth Preparation.....	44
4.2 Cadmium Telluride Growth.....	45
4.3 Mercury Telluride Growth.....	46
4.4 Mercury Cadmium Telluride Growth.....	47
4.5 Characterization Procedures.....	49
5. Experimental Results and Discussion	

5.1 CdTe Epilayer Growth.....	52
5.2 HgTe Epilayer Growth.....	62
5.3 Hg <sub>1-x</sub> Cd <sub>x</sub> Te Epilayer Growth	
5.3.1 Growth Rate of Hg <sub>1-x</sub> Cd <sub>x</sub> Te Layers.....	65
5.3.2 Thickness and Composition Uniformity.....	73
5.3.3 Surface Morphology.....	75
5.3.4 Defect Etching.....	82
5.3.5 Electrical Properties of Hg <sub>1-x</sub> Cd <sub>x</sub> Te Epilayers.....	82
6. Conclusion.....	91
7. Bibliography.....	92
8. Vita.....	97

## List of Figures

1.1 Infrared detectors as a function of wavelength.....	2
2.1 Energy gap as a function of composition in $\text{Hg}_{1-x}\text{Cd}_x\text{Te}$ .....	6
2.2 Crystal structure of $\text{Hg}_{1-x}\text{Cd}_x\text{Te}$ .....	8
2.3 Lattice constant and density versus alloy composition $x$ in $\text{Hg}_{1-x}\text{Cd}_x\text{Te}$ .....	10
2.4 Temperature dependence of Hall coefficients for typical $n$ - and $p$ -type $\text{Hg}_{1-x}\text{Cd}_x\text{Te}$ .....	13
2.5 $(T, x)$ phase diagram of $\text{Hg}_{1-x}\text{Cd}_x\text{Te}$ .....	18
3.1 Block diagram of OMVPE reactor system for II-VI epitaxial layer growth.....	31
3.2 Simplified schematic diagram of OMVPE reactor system for II-VI epitaxial growth.....	32
3.3 Cross-sectional drawing of the ARIIV reactor tube assembly.....	35
3.4 Cross-sectional view of fused quartz pedestal.....	38
3.5 Enlarged view of the fused quartz pedestal, substrate, mask, and heater assembly.....	40
5.1 Cleaved cross-sections used to measure the thickness of CdTe/InSb using Nomarski contrast; (a) $T_s=290^\circ\text{C}$ and (b) $T_s=300^\circ\text{C}$ .....	53
5.2 Growth rate of CdTe epilayer as a function of substrate temperature.....	54
5.3 Growth rate of CdTe epilayer as a function of the flow rate of MATE.....	55
5.4 Double crystal x-ray rocking diffraction curves for (a) CdTe/InSb epilayer and (b) InSb substrate.....	57
5.5 Electron channeling contrast pattern of CdTe epilayer.....	58
5.6 Double crystal x-ray rocking diffraction curves for (a) CdTe/CdTe epilayer and (b) CdTe substrate.....	60
5.7 Surface morphology grade as a function of ratio of DMCD to MATE flow rate.....	61

5.8	Nomarski contrast micrograph of CdTe epilayers showing microterraces (a) and pits (b).....	63
5.9	Growth rate of HgTe epilayer as a function of substrate temperature.....	64
5.10	Nomarski contrast micrograph of HgTe epilayer showing pits (a) 910x and (b) 448 x.....	66
5.11	Nomarski contrast micrograph of HgTe epilayer showing hillocks; (a) 177 x and (b) 910 x.....	67
5.12	Typical Fourier Transform of Infrared transmission curve of $Hg_{1-x}Cd_xTe$ epilayer grown on CdTe substrate.....	68
5.13	Nomarski contrast micrograph of cleaved cross-sections on two different composition samples after etching with Hähnert etchant.....	69
5.14	Growth rate and composition as a function of the flow rate of DMCD .....	70
5.15	Growth rate of $Hg_{1-x}Cd_xTe$ as a function of the flow rate of MATE .....	72
5.16	Thickness ( $\text{\AA}$ ) and compositional uniformity profile of initial stages in $Hg_{1-x}Cd_xTe$ epilayer growth with use of (a) a single Hg inlet and (b) dual Hg inlets were used. The parenthesis represent the refractive index of $Hg_{1-x}Cd_xTe$ .....	74
5.17	Compositional (x) uniformity of 4 $\mu\text{m}$ thick $Hg_{1-x}Cd_xTe$ epitaxial layer over 6.45 $\text{cm}^2$ CdTe substrate.....	76
5.18	Nomarski contrast micrograph of $Hg_{1-x}Cd_xTe$ epilayer showing hillocks; (a) $Q_{Te}=1.55$ sccm and (b) $Q_{Te}=3.1$ sccm at $T_s=330$ $^\circ\text{C}$ .....	78
5.19	Nomarski contrast micrograph of $Hg_{1-x}Cd_xTe$ epitaxial layers showing (a) as-grown $Hg_{1-x}Cd_xTe$ and (b) Hg-splattered $Hg_{1-x}Cd_xTe$ surface.....	79
5.20	Cross-sectional drawing of the modified ARIIV reactor tube assembly.....	80
5.21	Electron channeling contrast pattern of $Hg_{1-x}Cd_xTe$ epitaxial layer grown on CdTe substrate .....	81
5.22	Normarski contrast micrograph showing subgrain boundaries in $Hg_{1-x}Cd_xTe$ (a,b ) and subgrain boundaries in the CdTe substrate (c).....	83
5.23	The Hall coefficient $R_H$ as a function of reciprocal temperature for <i>n</i> -type $Hg_{1-x}Cd_xTe$ ( $x=0.126$ ) sample .....	84
5.24	The Hall mobility and the Hall carrier concentration as a function of reciprocal temperature for <i>n</i> -type $Hg_{1-x}Cd_xTe$ ( $x=0.126$ ) sample.....	86

5.25	The Hall coefficient $R_H$ as a function of reciprocal temperature for $p$ -type $Hg_{1-x}Cd_xTe$ ( $x=0.266$ ) sample .....	87
5.26	The Hall mobility and the Hall carrier concentration as a function of reciprocal temperature for $p$ -type $Hg_{1-x}Cd_xTe$ ( $x=0.266$ ) sample.....	88

## List of Tables

2.1	Physical properties of $\text{Hg}_{1-x}\text{Cd}_x\text{Te}$ .....	17
2.2	Process parameter comparison between unassisted pyrolysis and photocatalysis.....	26
5.1	Electrical properties of $\text{Hg}_{1-x}\text{Cd}_x\text{Te}$ grown by cold wall, pyrolytic OMVPE.....	90

## ABSTRACT

### Direct Growth of $\text{Hg}_{1-x}\text{Cd}_x\text{Te}$ by Cold Wall, Pyrolytic OMVPE

SukRyong Hahn, Ph. D

Supervising Professor : James D. Parsons

Mercury Cadmium Telluride ( $\text{Hg}_{1-x}\text{Cd}_x\text{Te}$ ) is an important semiconductor alloy for infrared detector applications, because its band gap (-0.16 eV - 1.6 eV at 4.2 K) is a function of Hg to Cd ratio. The fabrication of staring arrays for infrared radiation detection with uniform wavelength sensitivity requires the large area thickness and compositionally uniform  $\text{Hg}_{1-x}\text{Cd}_x\text{Te}$  alloys with excellent electronic properties.

Low temperature vapor phase epitaxy growth techniques have been proposed as a preferred approach for thick and thin film single crystal  $\text{Hg}_{1-x}\text{Cd}_x\text{Te}$  synthesis. Thus, we have attempted here, for the first time the direct growth of  $\text{Hg}_{1-x}\text{Cd}_x\text{Te}$  alloys by cold wall, pyrolytic OMVPE, using a newly designed ARIIV reactor that increases Hg incorporation, imposes uniformity, and avoids the need for high temperature processing to create alloys by interdiffusion approach.

The reactor was characterized in terms of the measured properties of CdTe, HgTe, and  $\text{Hg}_{1-x}\text{Cd}_x\text{Te}$  epilayers grown in it. The growth rate of CdTe, HgTe, and  $\text{Hg}_{1-x}\text{Cd}_x\text{Te}$  were correlated with substrate temperature, reactant flow rates (DMCd, MATe and elemental Hg) and reactor design. The growth rate of the  $\text{Hg}_{1-x}\text{Cd}_x\text{Te}$  layers at  $T_s=300$  °C, which was experimentally optimized condition, decreased from 4 to 0.75  $\mu\text{m}/\text{h}$ , but the composition of the  $\text{Hg}_{1-x}\text{Cd}_x\text{Te}$  epilayers increased from  $x=0.126$  to  $x=0.359$  as the DMCd flow rate increased from 0.0075 to 0.06 sccm at fixed MATe flow rate of 1.55 sccm.

Thickness and compositional mapping of thin  $\text{Hg}_{1-x}\text{Cd}_x\text{Te}$  epilayers, by employing the multiple angle of incidence ellipsometry technique, showed excellent uniformity with  $990 \pm 20 \text{ \AA}$  for thickness uniformity and  $x = 0.602 \pm 0.002$  for compositional uniformity. The compositional uniformity of a  $4 \text{ \mu m}$  thick  $\text{Hg}_{1-x}\text{Cd}_x\text{Te}$  epilayer ( $x = 0.152$ ) also revealed exceptional uniformity, with  $\Delta x = \pm 0.002$  over a  $6.45 \text{ cm}^2$  area of the CdTe substrate.

The Hall effect measurements on as-grown  $\text{Hg}_{1-x}\text{Cd}_x\text{Te}$  showed  $n$ -type characteristics for  $x < 0.25$  and  $p$ -type characteristics for  $x \geq 0.25$ . The electron carrier concentrations and the electron mobilities for  $n$ -type  $\text{Hg}_{1-x}\text{Cd}_x\text{Te}$  materials were in the range  $(0.4 - 2.6) \times 10^{16} \text{ cm}^{-3}$  and  $(2.0 - 4.1) \times 10^4 \text{ cm}^2/\text{V}\cdot\text{sec}$ , respectively, at  $77 \text{ K}$ . The relatively constant carrier concentration and rather poor mobilities as a function of temperature was determined to be subgrain boundaries in the CdTe substrates.

## List of Acronyms

<i>ARI:</i>	Annular Reactant Inlet
<i>ARIIV:</i>	Annular Reactant Inlet Inverted-Vertical
<i>CCD:</i>	Charged Coupled Device
<i>CdTe:</i>	Cadmium Telluride
<i>CdZnTe:</i>	Cadmium Zinc Telluride
<i>CID:</i>	Charge Injection Device
<i>DAG:</i>	Direct Alloy Growth
<i>DCXRC:</i>	Double Crystal X-ray Diffraction
<i>DETe:</i>	Diethyltelluride
<i>DIPTe:</i>	Diisopropyltelluride
<i>DMCd:</i>	Dimethylcadmium
<i>DPTe:</i>	Dipropyltelluride
<i>DTBTe:</i>	Ditertiarybutyltelluride
<i>ECCP:</i>	Electron Contrast Channeling Patterns
<i>ESCA:</i>	Electron Spectroscopy for Chemical Analysis
<i>FPA:</i>	Focal Plane Array
<i>FTIR:</i>	Fourier Transform Infrared
<i>FWHM:</i>	Full Width at Half Maximum
<i>GaAs:</i>	Gallium Arsenide
<i>HgTe:</i>	Mercury Telluride
<i>Hg<sub>1-x</sub>Cd<sub>x</sub>Te:</i>	Mercury Cadmium Telluride
<i>ID:</i>	Inside Diameter
<i>I<sub>light</sub>:</i>	Intensity of light
<i>IMP:</i>	Interdiffused Multi-layer Process

<b><i>InSb:</i></b>	Indium Antimonide
<b><i>IR:</i></b>	Infrared
<b><i>ISOVPE:</i></b>	Isothermal Vapor Phase Epitaxy
<b><i>IV:</i></b>	Inverted-Vertical
<b><i>LPE:</i></b>	Liquid Phase Epitaxy
<b><i>LWIR:</i></b>	Long Wavelength Infrared (8-14 $\mu\text{m}$ )
<b><i>MAI:</i></b>	Multiple Angle of Incidence
<b><i>MATe:</i></b>	Methylallyltelluride
<b><i>MBE:</i></b>	Molecular Beam Epitaxy
<b><i>MFC:</i></b>	Mass Flow Controller
<b><math>\mu\text{m/h}</math>:</b>	Epilayer Growth Rate per Hour
<b><i>MOCVD:</i></b>	Metal Organic Vapor Phase Epitaxy
<b><i>MOSFET:</i></b>	Metal-Oxide-Semiconductor Field-Effect Transistor
<b><i>MWIR:</i></b>	Middle Wavelength Infrared (3-5 $\mu\text{m}$ )
<b><i>OD:</i></b>	Outside Diameter
<b><i>OMVPE:</i></b>	Organometallic Vapor Phase Epitaxy
<b><i>Q:</i></b>	Flow Rate
<b><i>Q<sub>Cd</sub>:</i></b>	Flow Rate of DMCD
<b><i>Q<sub>Te</sub>:</i></b>	Flow Rate of MATe
<b><i>R<sub>g</sub>:</i></b>	Growth Rate
<b><i>SCCM:</i></b>	Standard Cubic Centimeter per Minute
<b><i>SEM:</i></b>	Scanning Electron Microscopy
<b><i>SLPM:</i></b>	Standard Liters Per Minute
<b><i>SSR:</i></b>	Solid State Recrystallization
<b><i>TCE:</i></b>	Trichloroethane
<b><i>THM:</i></b>	Traveling Heater Method
<b><i>T<sub>s</sub>:</i></b>	Substrate Temperature

***VPE:***

Vapor Phase Epitaxy

## 1. INTRODUCTION

Mercury cadmium telluride ( $\text{Hg}_{1-x}\text{Cd}_x\text{Te}$ ) is an important semiconductor alloy for infrared detector applications, because its bandgap (-0.16 to 1.6 eV, at 4.2 K) is a function of Hg to Cd ratio as shown in Fig. 1.1.  $\text{Hg}_{1-x}\text{Cd}_x\text{Te}$  sensitivity covers the entire spectral range from 0.8  $\mu\text{m}$  (CdTe) to over 20  $\mu\text{m}$ . This range is ideally suited for infrared detectors because the two atmospheric transmission windows for infrared wavelengths are at middle wavelength infrared (MWIR: 3-5  $\mu\text{m}$ ) and at long wavelength infrared (LWIR: 8-14  $\mu\text{m}$ ) [1 - 4]. The energy gaps which can detect infrared signals in these wavelength ranges are 0.25 - 0.4 eV for MWIR signals and 0.1-0.15 eV for LWIR signals. The  $\text{Hg}_{1-x}\text{Cd}_x\text{Te}$  composition of special importance for detectors in the 8-14  $\mu\text{m}$  range, where it has unrivaled performance, is  $x \cong 0.2$ .

$\text{Hg}_{1-x}\text{Cd}_x\text{Te}$  photodiodes, as detectors for infrared radiation, are conventionally fabricated from high purity *p*-type material, whereas photoconductors are fabricated from high purity *n*-type material. Although the photodiode device is much more difficult to fabricate, due to the requirement for a *p-n* junction, it can be used in the form of large focal plane arrays (FPA). These arrays, when coupled to charge coupled devices (CCD's), charge injection devices (CID's), or MOSFET *x-y* addresses, allow for a more efficient detector system compared to the photoconductors because of the lower power [5].

The fabrication of a large number of IR radiation detector elements (metal-insulator-semiconductor photodiodes or photoconductors) in array form depends on an ability to obtain a thin layer of this material with excellent electronic properties and uniformity. The uniformity requirement is difficult to meet by traditional bulk crystal methods such as Bridgeman technique [6-8], solid state

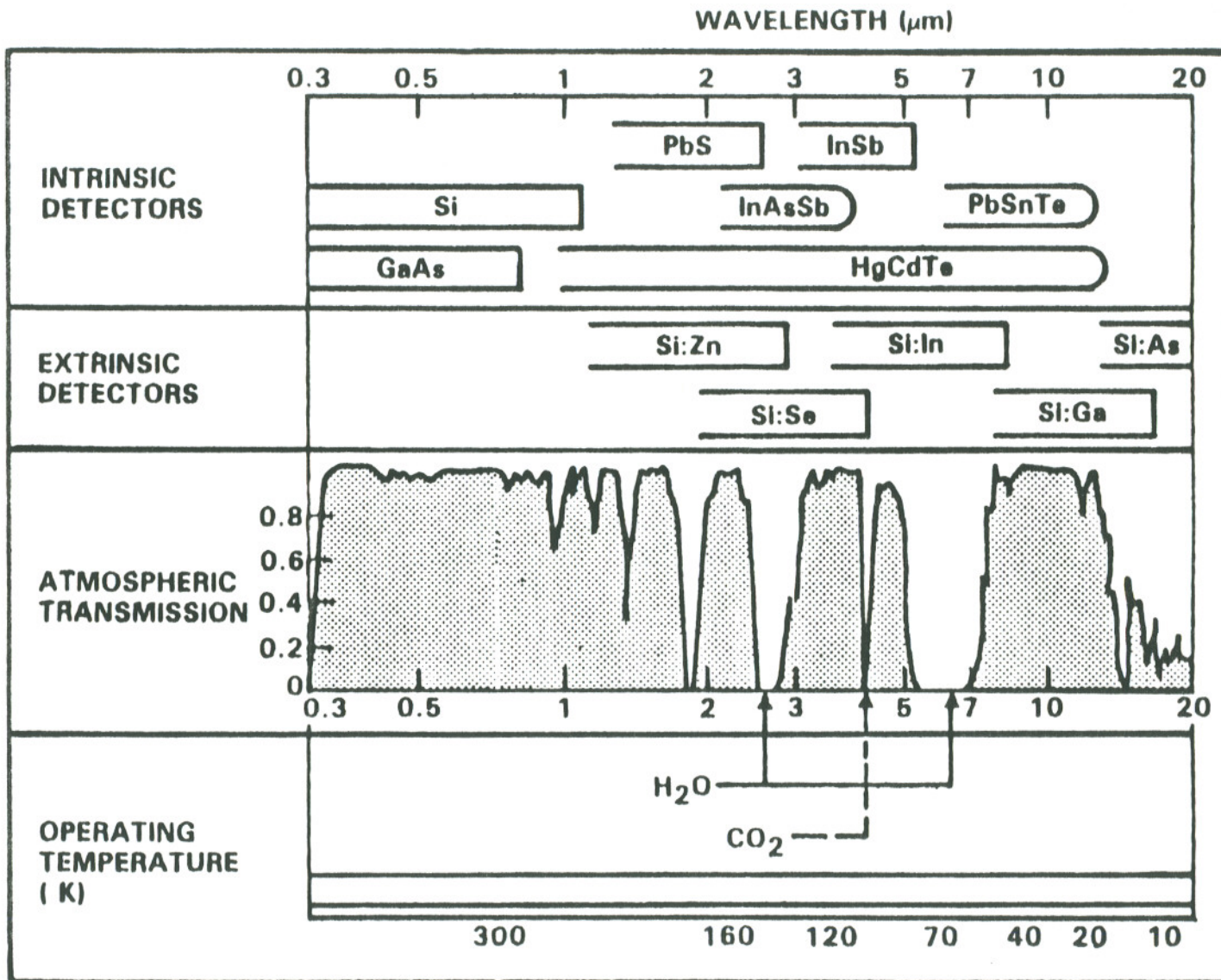


Figure 1.1 Infrared detectors as a function of wavelength.

recrystallization (SSR) [9], and traveling heater method (THM) [10]. Epitaxial growth techniques have been utilized as an alternative for this reason.

In the past two decades, the development of  $\text{Hg}_{1-x}\text{Cd}_x\text{Te}$  for IR detector focal plane arrays has emphasized methods of thin-film epitaxial growth such as liquid phase epitaxy (LPE) [11], isothermal vapor phase epitaxy (ISOVPE) [12], organo-metallic vapor phase epitaxy (OMVPE) [13], and molecular beam epitaxy (MBE), because of the known and accepted advantages of such configurations. These advantages include (1) the possible use of commercially available existing substrate materials; (2) growth of two or more epitaxial layers in sequence on the same substrate allows the preparation of complete detector structures, including heterojunctions, in a single growth process or series of growth processes; (3) epitaxial layers made by these growth techniques can be more uniform in composition, compared to bulk  $\text{Hg}_{1-x}\text{Cd}_x\text{Te}$ ; and (4) the use of high-resistivity (semi-insulating) CdTe or other wide bandgap semiconductors as substrate material allows backside illumination of the detector, through the substrate, so that the required contacts to the individual detectors of an array can be made from the top side by flip-chip or other suitable bonding techniques without interfering with the array optics.

The LPE process has three important limitations: (1) LPE can only be employed to grow  $\text{Hg}_{1-x}\text{Cd}_x\text{Te}$  epilayers on substrates that are thermally and chemically stable in a Hg or Te solvent; (2) LPE grown epilayers have graded compositions in the direction of growth due to the high temperatures employed by the process; and (3) impurities used to increase the resistivity of CdTe and (CdZn)Te substrates diffuse into LPE grown  $\text{Hg}_{1-x}\text{Cd}_x\text{Te}$  epilayers during growth, thereby causing unpredictable changes in the conductivity of both the substrate and the epilayer.

Low temperature vapor phase epitaxy (VPE) is a preferred approach for thick and thin film single crystal  $\text{Hg}_{1-x}\text{Cd}_x\text{Te}$  synthesis. The advantages of this VPE film approach are (1) substrates other than CdTe (also difficult to grow) can be used, e.g. InSb; and (2) the electrical and compositional uniformity of epilayers is generally far superior to bulk material. Further, thick in-situ CdTe buffer layers can be grown on cheaper, more readily available substrates, and the  $\text{Hg}_{1-x}\text{Cd}_x\text{Te}$  epilayers can subsequently be grown on the buffer layers; then the initial substrate can be removed from the buffer and  $\text{Hg}_{1-x}\text{Cd}_x\text{Te}$  layers.

Organometallic vapor phase epitaxy (OMVPE) would be the preferred VPE approach for epitaxial growth of  $\text{Hg}_{1-x}\text{Cd}_x\text{Te}$  epilayers ( $0 \mu\text{m} < \text{thickness} \leq 100 \mu\text{m}$ ), if the Hg to Cd ratio could be easily controlled. A major advantage of OMVPE is low temperature synthesis ( $\leq 300 \text{ }^\circ\text{C}$ ); thus, better uniformity can be obtained through the layer, lower vacancy concentration can be obtained in the layer, and any suitable substrate can be used. Thus, we have attempted here, for the first time the direct growth of  $\text{Hg}_{1-x}\text{Cd}_x\text{Te}$  compounds by cold wall, pyrolytic OMVPE, using the metalorganic reactants dimethylcadmium  $[(\text{CH}_3)_2\text{Cd} : \text{DMCd}]$  and methylallyltelluride  $[\text{C}_4\text{H}_8\text{Te} : \text{MATE}]$ , and a newly designed annular reactant inlet inverted vertical (ARIIV) reactor that increases Hg incorporation, imposes uniformity, and avoids the need for high temperature processing to create alloys by interdiffusion approach.

The overall technical approach to CdTe, HgTe, and  $\text{Hg}_{1-x}\text{Cd}_x\text{Te}$  growth is described in the next chapter. Chapter 3 presents a detailed technical approach used for this study. The procedures of epilayer growth and characterization are described in Chapter 4. The characterization results of as-grown II-VI epilayers are discussed in Chapter 5, followed by conclusions in Chapter 6.

## 2. BACKGROUND OF $\text{Hg}_{1-x}\text{Cd}_x\text{Te}$

### 2.1 Physical Properties

$\text{Hg}_{1-x}\text{Cd}_x\text{Te}$  has been extensively studied since Lawson et al. reported that the ternary alloy could be synthesized from HgTe and CdTe [14]. The energy gap of  $\text{Hg}_{1-x}\text{Cd}_x\text{Te}$  varies between  $E_g = 1.6$  eV (CdTe) and  $-0.3$  eV (HgTe) at 4.2 K. The energy gap of  $\text{Hg}_{1-x}\text{Cd}_x\text{Te}$  is direct and increases linearly from  $-0.3$  eV to  $1.6$  eV as  $x$  increases from 0 (HgTe) to 1 (CdTe) as shown in Fig. 2.1. The  $\Gamma_6$  state, which is the conduction band minimum in CdTe and other zinc-blende semiconductors, lies at a lower energy in HgTe than the  $\Gamma_8$  state, which is the valence band maximum in CdTe. Thus the energy gap  $E_0$  is negative in HgTe. The usual light-hole valence band becomes the conduction band and the conduction band becomes the light-hole valence band. Because of the  $k \cdot p$  interaction [15] the conduction band and light-hole valence bands are nonparabolic. The right hand portion of Figure 2.1 illustrates the region near the  $\Gamma$  point when the energy gap is relatively wide, where it is parabolic.

The composition dependence of energy gap, the  $\Gamma_6 - \Gamma_8$  transition, at 0 and 300 K is illustrated in Fig. 2.1. This figure shows the temperature coefficient [ $= \partial E_g / \partial T$ ] of the energy gap for CdTe is negative, which is usual for most semiconductors, but is positive for Hg rich compositions. The compositional and temperature dependencies for  $x$  values equal to or less than 0.40, which is the region of most interest in IR detector fabrication, have been extensively studied to measure the composition or the  $x$  value at a given temperature without destroying the  $\text{Hg}_{1-x}\text{Cd}_x\text{Te}$ . The two primary optical properties of interest in epitaxial  $\text{Hg}_{1-x}\text{Cd}_x\text{Te}$  layers are absolute percent transmittance and spectral cut-onwavelength and shape. The spectral cut-on as determined using IR spectroscopy is a measure

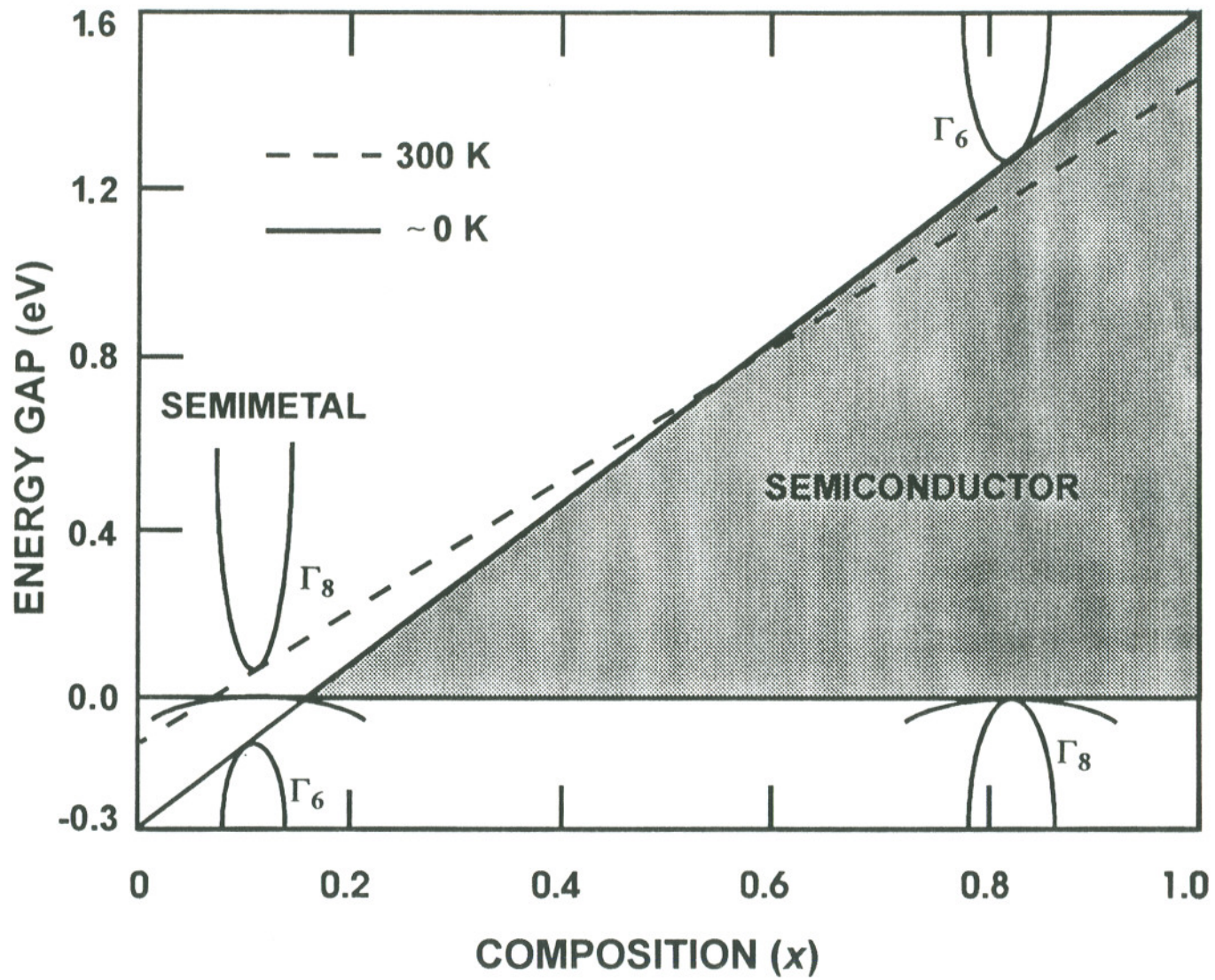


Figure 2.1 Energy gap as a function of composition in  $\text{Hg}_{1-x}\text{Cd}_x\text{Te}$  [16].

of the  $x$  value of the  $\text{Hg}_{1-x}\text{Cd}_x\text{Te}$  at a given temperature. A revised empirical relation in the composition range of  $x \leq 0.6$  and  $x = 1$  was proposed by Hansen *et al.* [17].

$$E_g = 1.24/\lambda_c (\mu\text{m}) = -0.302 + 1.93x + 5.35(10^{-4})T(1-2x) - 0.801x^2 + 0.832x^3 \dots \text{Eq. 2.1}$$

where  $E_g$  is the energy gap in electron volts,  $x$  is the composition variable, and  $T$  is the absolute temperature. The composition of  $\text{Hg}_{1-x}\text{Cd}_x\text{Te}$  is measured by using Equation 2.1 if the cut-on wavelength and the measuring temperature are known.

The thickness of  $\text{Hg}_{1-x}\text{Cd}_x\text{Te}$  epitaxial layer is measured by the interference pattern observed on the IR spectral transmission curves. The periodicity of the interference pattern is directly related to layer thickness, which is given by expression,

$$d (\mu\text{m}) = 10^4/2n(\Delta\nu), \dots \text{Eq. 2.2}$$

where  $d$  is the layer thickness in  $\mu\text{m}$ ,  $n$  is refractive index of layer, and  $\Delta\nu$  is average separation per cycle (i.e., distance between successive peaks) from the interference pattern in wave numbers. The values for the refractive indices of  $\text{Hg}_{1-x}\text{Cd}_x\text{Te}$  are available from the reference *Properties of Mercury Cadmium Telluride* [18].

The structure of  $\text{Hg}_{1-x}\text{Cd}_x\text{Te}$  is the zinc-blende, which is composed of four atoms in the unit cell, as shown in Figure 2.2. This figure shows that the cations (Hg or Cd) are distributed randomly over the cation sites [(0 0 0), (0 1/2 1/2), (1/2 0 1/2), (1/2 1/2 0)] and the anion (Te) occupies the other sites [(1/4 1/4 1/4), (1/4 3/4 3/4), (3/4 1/4 3/4) (3/4 3/4 1/4)]. The lattice constant of HgTe is 6.463 Å ( $x=0$ )

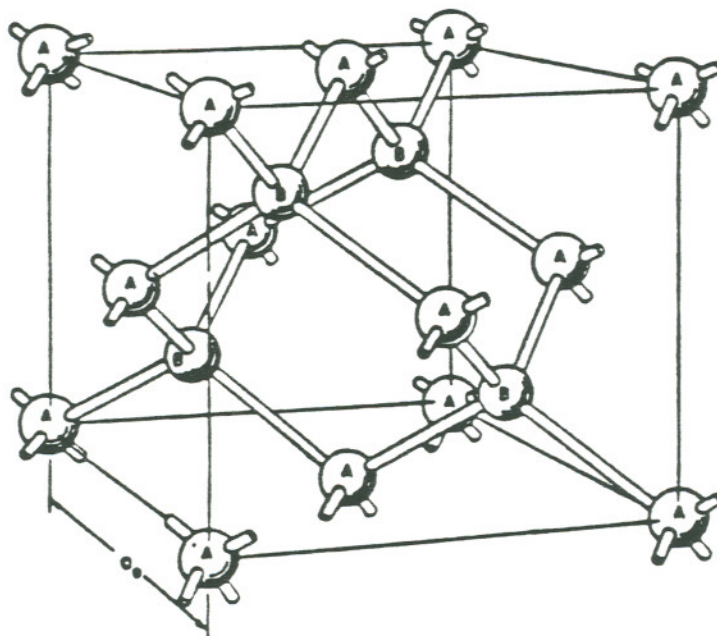


**Figure 2.2** Crystal structure of  $\text{Hg}_{1-x}\text{Cd}_x\text{Te}$ ; A site: Cd or Hg and B site: Te [19].

and that of CdTe ( $x=1$ ) is 6.482 Å at room temperature.

The dependence of lattice constant and density is shown in Figure 2.3. The lattice constant variation as a function of composition shows a small deviation from Vegard's law, which is linear with composition, but the variation of density is linear with composition. Because of this linearity of density with composition, density measurement of  $\text{Hg}_{1-x}\text{Cd}_x\text{Te}$  is often used in determining the composition indirectly by weighing the substrate before and after epitaxial film deposition. The lattice mismatch between CdTe and  $\text{Hg}_{0.8}\text{Cd}_{0.2}\text{Te}$  is about 0.3% [21,22]. It is natural that CdTe is chosen as a substrate of  $\text{Hg}_{1-x}\text{Cd}_x\text{Te}$  epitaxial films because of this small lattice mismatch.

The electrical properties of  $\text{Hg}_{1-x}\text{Cd}_x\text{Te}$  could be indirectly obtained by measuring the Hall coefficient  $R_H$ . The drift currents carried by both holes and electrons add to give a larger total if both are present in the same material. The current density  $\mathbf{J}$  carried by drifting carriers is

$$\mathbf{J} = nq\mathbf{v}_d, \dots\dots\dots \text{Eq. 2.3}$$

where  $n$  is the number of carriers of charge  $q$  per unit volume and  $\mathbf{v}_d$  is the drift velocity; if there are different kinds of carriers present they contribute separately to the current density.

The electrical conductivity  $\sigma$  of a sample is defined as the current that flows across unit cube when the field and hence voltage between opposite faces is unity. Thus for a semiconductor where both electrons and holes are present,

$$\sigma = ne\mu_e + pe\mu_h \dots\dots\dots \text{Eq. 2.4}$$

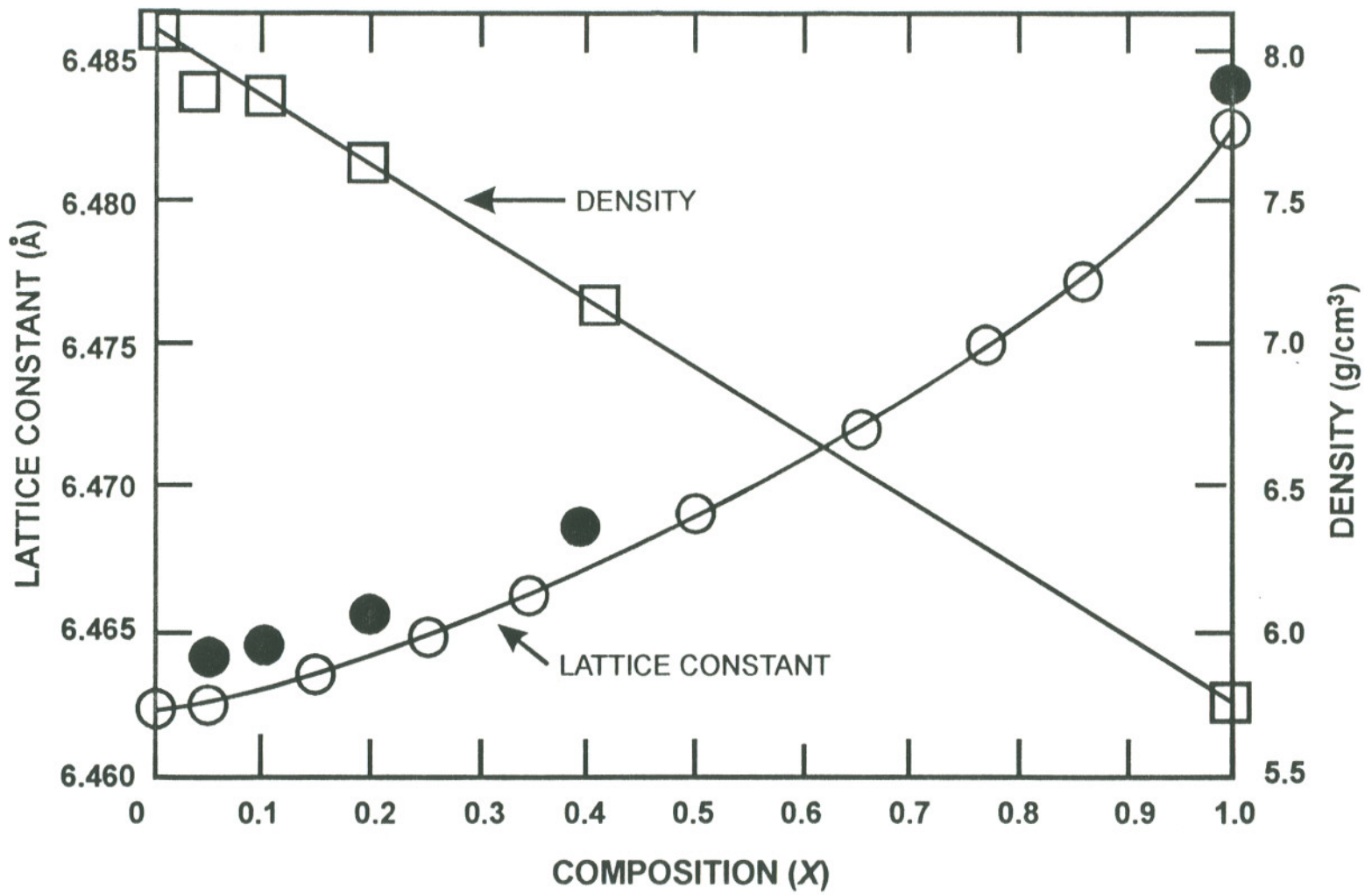


Figure 2.3 Lattice constant and density versus alloy composition  $x$  in  $\text{Hg}_{1-x}\text{Cd}_x\text{Te}$  [20].

where  $n$  is the electron carrier concentration,  $p$  is the hole carrier concentration,  $e$  is the charge  $1.6 \times 10^{-19}$  C, and  $\mu_e$  and  $\mu_h$  are the mobilities of electrons and holes, respectively. When a current of density  $\mathbf{J}$  flows in a semiconductor perpendicular to a magnetic field  $\mathbf{B}$ , there is a force on the electrons and holes perpendicular to both  $\mathbf{B}$  and  $\mathbf{J}$ , and a transverse current tends to flow. The process is known as the *Hall effect*, and provides a way of estimating the majority-carrier density and sign, and is also the basis of devices for measuring magnetic field and for multiplying two signals. The Hall coefficient depends on the applied current and voltage and the intensity of applied magnetic field.

For p-type semiconductor, in case of weak magnetic field, the Hall coefficient  $R_H$  is

$$R_H = (r/ep) S, \dots\dots\dots \text{Eq. 2.5}$$

where  $r$  is scattering factor, which includes the lattice scattering and the ionized impurity scattering, and  $S$  is the symmetry factor [23].

$S$  is also described by the following formula using the ratio  $K$ , the longitudinal effective mass to the transverse effective mass,

$$S = 3K(K+2)/(2K+1)^2, \dots\dots\dots \text{Eq. 2.6}$$

where  $K$  depends on the band structure of materials. When the band structure of a material is parabolic,  $S$  becomes 1 because  $K$  has the value of 1 at  $k = 0$ . The generalized formula for electrons and holes, from Equation 2.5, becomes

$$R_H = (R_n \sigma_n^2 + R_p \sigma_p^2)/(\sigma_n + \sigma_p)^2. \dots\dots\dots \text{Eq. 2.7}$$

If we consider the scattering factor  $r$  and the symmetry factor  $S=1$  and use Equation 2.4, the Hall coefficient is described as follows,

$$R_H = r(p - nb^2)/e(p + nb)^2, \dots\dots\dots \text{Eq. 2.8}$$

where  $b$  is the mobility ratio of electrons to holes. Because the scattering factor  $r$  is approximately unity for  $\text{Hg}_{1-x}\text{Cd}_x\text{Te}$  [23, 24], the Hall coefficient of  $\text{Hg}_{1-x}\text{Cd}_x\text{Te}$  can be described by

$$R_H = (p - nb^2)/e(p + nb)^2. \dots\dots\dots \text{Eq. 2.9}$$

The temperature dependence of the Hall coefficients of  $n$  and  $p$ -type  $\text{Hg}_{1-x}\text{Cd}_x\text{Te}$ , which is a narrow energy gap semiconductor, show totally different characteristics according to Capper's model [25]. Unlike  $n$ -type  $\text{Hg}_{1-x}\text{Cd}_x\text{Te}$ , for which no evidence of donor freeze out has been reported,  $p$ -type  $\text{Hg}_{1-x}\text{Cd}_x\text{Te}$  generally shows appreciable acceptor freeze out at low temperatures. Lou *et al.* [26] classified  $p$ -type  $\text{Hg}_{1-x}\text{Cd}_x\text{Te}$  into two cases, i.e., anomalous phenomena and classical phenomena. The anomalous phenomena of  $p$ -type  $\text{Hg}_{1-x}\text{Cd}_x\text{Te}$  shows a dip or double inversion in the temperature dependence of the Hall coefficient with increasing temperature [27 - 29]. In case of classical phenomena, it is generally accepted that the temperature dependence of the Hall coefficient for  $p$ -type narrow energy gap semiconductors reveals the type transition [30], that is, a conversion from  $n$ - to  $p$ -type characteristics as the temperature decreases, as shown in Figure 2.4. From Figure 2.4, AB is the intrinsic region that the electron conduction is dominant, BCD is the mixed conduction region in which electrons and holes contribute to conduction, DE is the ionized acceptor region, and EF is the region of acceptor freeze out. The Hall coefficient in the region AB,

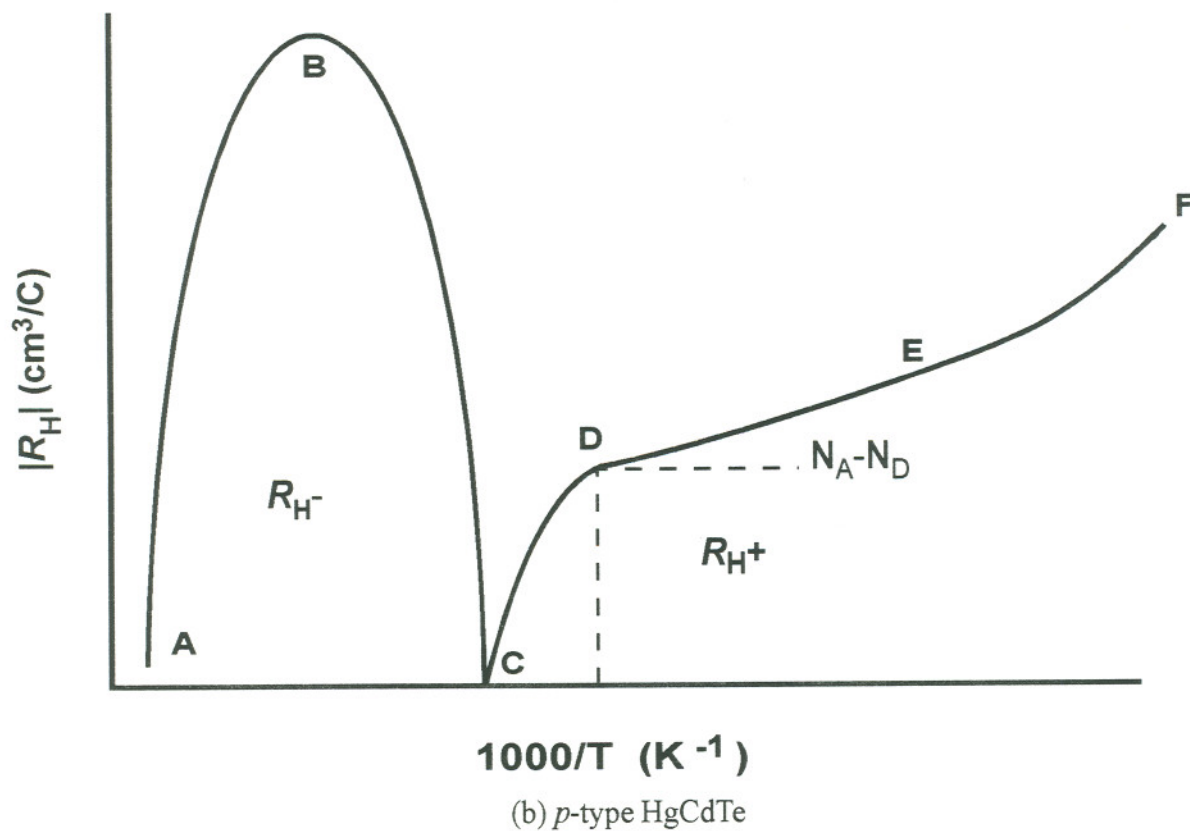
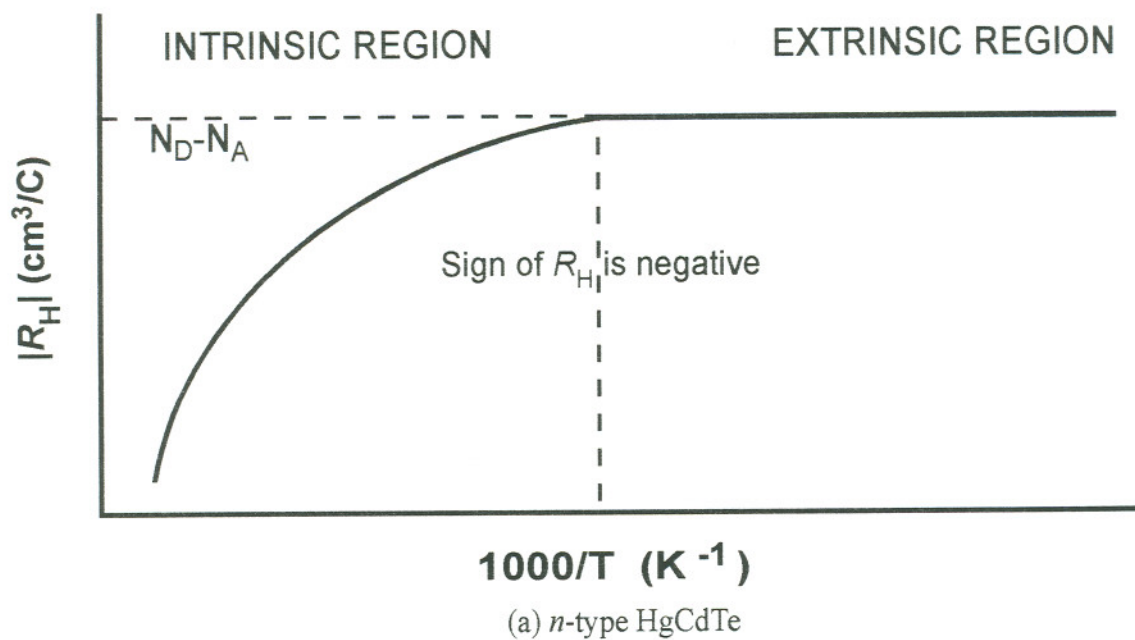


Figure 2.4 Temperature dependence of Hall coefficients for typical *n*- and *p*-type HgCdTe [30].

in terms of intrinsic carrier concentrations  $n_i$ , is described by

$$R_H = -1/en_i, \dots\dots\dots \text{Eq. 2.10}$$

where  $n_i$  is a function of temperature  $T$  and composition  $x$  [31], which is expressed by

$$n_i(x, T) = (5.585 - 3.820x + 0.001753T - 0.001364xT) \cdot 10^{14} \cdot E_g^{3/4} T^{3/2} \exp(-E_g/2kT). \dots\dots\dots \text{Eq. 2.11}$$

The Hall coefficient of both electrons and holes, in region BCD, is

$$R_H = (p-nb^2)/e(p+nb)^2. \dots\dots\dots \text{Eq. 2.12}$$

In region DEF, which acceptors are dominant, the Hall coefficient is described as

$$R_H = 1/ep. \dots\dots\dots \text{Eq. 2.13}$$

In determining the electrical transport properties of  $\text{Hg}_{1-x}\text{Cd}_x\text{Te}$  by Hall measurement, anomalous effects can sometimes occur and lead to results which are difficult to interpret. The main reasons for this anomalous behavior are the large ratio of electron mobility to hole mobility as well as the tendency to form  $n$ -type conducting regions either within the bulk or at the surface of the  $p$ -type  $\text{Hg}_{1-x}\text{Cd}_x\text{Te}$  samples. Zemel *et al.* [32] studied this problem by investigating the magnetic field dependence of the Hall coefficient in association with a layer model. Accurate results on concentration and mobility of both electrons and holes can be obtained.

The electrical properties and the controllability of these properties in epitaxially grown materials are as important as the crystallographic properties in fabricating electrical devices. The most important factor to be considered prior to the application of a certain material is the doping characteristics.

There are basically two methods for doping  $\text{Hg}_{1-x}\text{Cd}_x\text{Te}$  semiconductors, one using intrinsic defects of the material by controlling stoichiometry and the other using extrinsic dopants by substituting foreign elements with different numbers of valence electrons. To help understand point defects (intrinsic defects) in  $\text{Hg}_{1-x}\text{Cd}_x\text{Te}$  crystals, which have important effects on the electrical properties of  $\text{Hg}_{1-x}\text{Cd}_x\text{Te}$  epitaxial or bulk crystals, these defects will be discussed in some detail.

There are various types of point defects in  $\text{Hg}_{1-x}\text{Cd}_x\text{Te}$  crystals. Major point defects are vacancies ( $V_{\text{Hg}}$  and  $V_{\text{Te}}$ ), interstitials ( $\text{Hg}_\text{I}$  and  $\text{Te}_\text{I}$ ), antisites ( $\text{Te}_{\text{Hg}}$  and  $\text{Hg}_{\text{Te}}$ ), and foreign elements (interstitial and substitutional).

Among these defects, the Hg vacancy is the most abundant defect at the processing temperatures of most growth techniques, due to the high equilibrium vapor pressure of Hg and the retrograde solubility of Te (specially for  $\text{Hg}_{1-x}\text{Cd}_x\text{Te}$  prepared at higher temperature). In most cases,  $\text{Hg}_{1-x}\text{Cd}_x\text{Te}$  is grown under Te-rich conditions to avoid the high Hg pressure of the Hg-rich process. If the  $\text{Hg}_{1-x}\text{Cd}_x\text{Te}$  crystal (bulk or epitaxial film grown at temperatures higher than 400 °C) is rapidly cooled to room temperature, there will be excess Te and Hg vacancies due to the higher solubility of Te at the growth temperature. This excess Te causes precipitates under low temperature annealing conditions, if it is not properly annihilated. Also the Hg vacancy is the most important defect related to the electrical properties of the material. Hg vacancies in  $\text{Hg}_{1-x}\text{Cd}_x\text{Te}$  are responsible for the observed shallow acceptor level; thus they will impact the electron and hole mobility. They are also responsible for dislocation formation and propagation as well as self diffusion and impurity diffusion.

The majority of undoped bulk and epitaxial (LPE or ISOVPE)  $\text{Hg}_{1-x}\text{Cd}_x\text{Te}$  alloys grown at higher temperature ( $\geq 400$  °C) exhibit p-type characteristics and the origin of this p-type behavior is generally believed to be due to the existence of doubly ionized Hg vacancies [33].

The other physical properties of  $\text{Hg}_{1-x}\text{Cd}_x\text{Te}$  which are proper to IR detection are: (1) the high absorption coefficient ( $\alpha \cong 1,000$   $\text{cm}^{-1}$ ), (2) low intrinsic carrier concentrations ( $\cong 10^{14}$  -  $10^{15}$   $\text{cm}^{-3}$ ) and high electron mobility ( $\cong 10^4$  -  $10^5$   $\text{cm}^2/\text{V}\cdot\text{sec}$ ) in n-type  $\text{Hg}_{1-x}\text{Cd}_x\text{Te}$ , and (3) a small radiative carrier life time ( $\cong 0.1$  -  $10$   $\mu\text{s}$ ) for n-type  $\text{Hg}_{1-x}\text{Cd}_x\text{Te}$  [33]. The physical properties, including additional characteristics of  $\text{Hg}_{1-x}\text{Cd}_x\text{Te}$ , are summarized in Table 2.1 [18].

## 2.2 Crystal Growth Techniques of $\text{Hg}_{1-x}\text{Cd}_x\text{Te}$

### 2.2.1 Bulk Crystals

The liquid/solid quasi-equilibrium methods of crystal growth have always been considered for high quality semiconductor compounds due to their potentially better crystal structure. However, for a ternary alloy of  $\text{Hg}_{1-x}\text{Cd}_x\text{Te}$ , with a large difference in liquidus and solidus compositions along a given thermal tie line (Figure 2.5 [34]), the slow moving interface of these near equilibrium processes invariably result in compositional grading through the crystal.

Several modified bulk crystal growth methods such as slush growth, SSR growth [9], and THM [10, 13], have been used subsequent to the development of Bridgman growth by Wooley *et al.* [21], in order to find slices of excellent compositional uniformity at certain composition.

In the vertical Bridgman (Stockbarger) method of crystal growth, directional freezing results in a compositional variation along the growth axis [35]. Bartlett *et al.* [36, 37] reported that the compositional variation along the longitudinal and

Table 2.1 Physical properties of  $\text{Hg}_{1-x}\text{Cd}_x\text{Te}$  [18].

	HgTe	$\text{Hg}_{0.8}\text{Cd}_{0.2}\text{Te}$	CdTe
Lattice structure	cubic (ZnS)	cubic (ZnS)	cubic (ZnS)
Lattice constant a (300 K) [ $\text{\AA}$ ]	6.463	6.4645	6.482
Density $\gamma$ (300 K) [ $\text{g}\cdot\text{cm}^{-3}$ ]	8.076	7.63	5.85
Opt. phonons (77 K)			
LO ( $\text{cm}^{-1}$ )	138	157	170
TO ( $\text{cm}^{-1}$ )	118	150	142
Energy gap (eV)			
$E_g$ (300 K)	-0.15	0.165	1.505
$E_g$ (77 K)	-0.25	0.09	1.60
$E_g$ (0 K)	-0.30	0.064	1.605
Effective mass (77 K)			
$M_c^*/m_0$	0.029	0.005	0.096
$M_v^*/m_0$	0.35 - 0.7	0.2 - 0.6	0.66
Mobilities (77 K)			
$\mu_n$ ( $\text{cm}^2/\text{V}\cdot\text{sec}$ )		$2.5 \times 10^5$	
$\mu_p$ ( $\text{cm}^2/\text{V}\cdot\text{sec}$ )		$7 \times 10^2$	
Intrinsic carr. conc.			
$n_i$ (300 K) [ $\text{cm}^{-3}$ ]		$2 \times 10^{16}$	
$n_i$ (77 K) [ $\text{cm}^{-3}$ ]		$2 \times 10^{13}$	
Melting point (K)	943	1050	1365
Thermal exp. coeff.			
$\alpha$ (300 K) [ $10^{-6}\text{K}^{-1}$ ]	4	4.3	5.5
$\alpha$ (77 K) [ $10^{-6}\text{K}^{-1}$ ]	2		
Thermal conductivity			
C (300 K) [ $\text{Wcm}^{-1}\text{K}^{-1}\text{s}^{-1}$ ]	0.04		0.07
C (77 K) [ $\text{Wcm}^{-1}\text{K}^{-1}\text{s}^{-1}$ ]	0.15		0.4

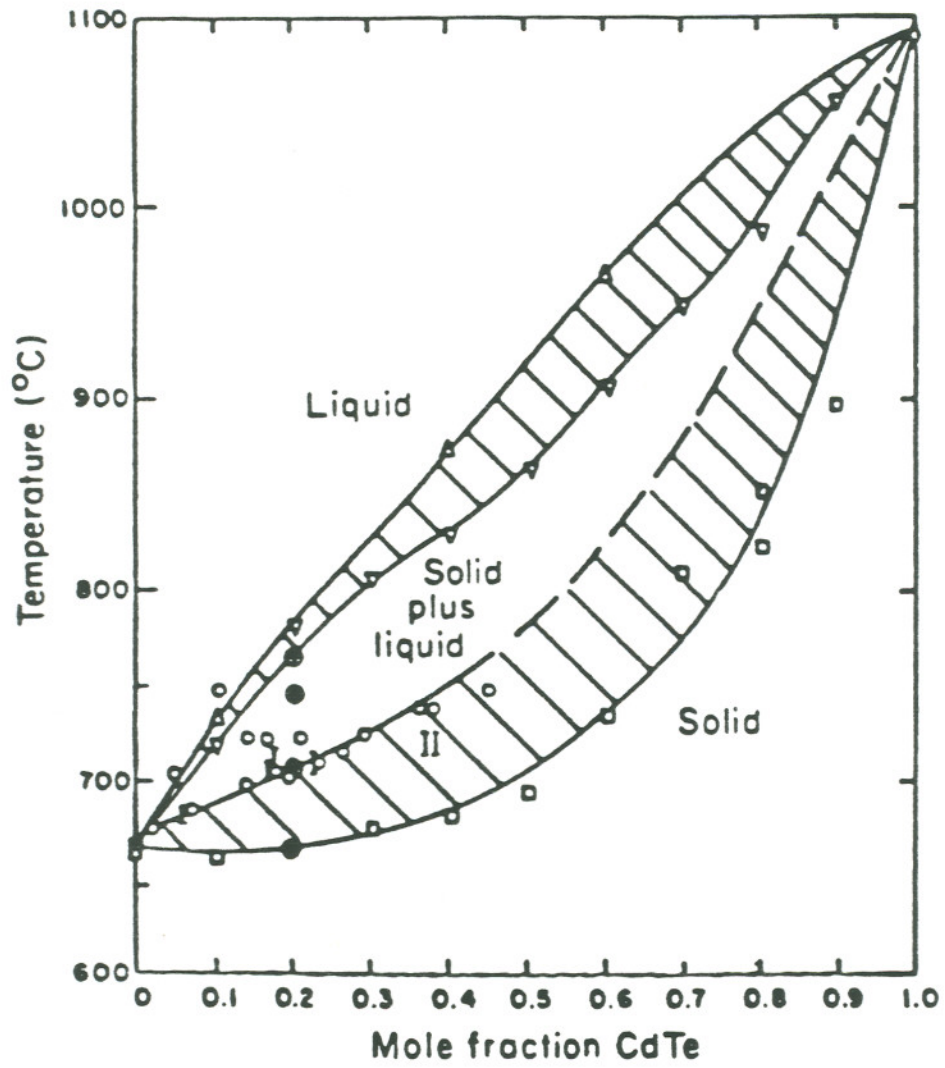


Figure 2.5 (T,x) phase diagram of  $\text{Hg}_{1-x}\text{Cd}_x\text{Te}$  [33].

radial directions depends upon the crystal growth rates. They also showed that mixing conditions in the melt (related to sizes of raw material charging the crucible, temperature gradient of growth furnace, and gravity) make it difficult to grow crystals free of compositional grading by the vertical Bridgman method.

Slush growth, a new method of taking advantage of the CdTe-HgTe pseudobinary alloys, was proposed by Harman [38]. In this method, a charge of alloy is prepared by conventional methods and lowered quickly to a new position in a vertical furnace so that the bottom part of the liquid is quickly frozen. Harman reported that a high quality single crystal is found in the solid region adjacent to the portion of the solid/liquid interface just prior to cooling. This slush growth method was adapted by Cominco for the production of bulk, detector grade  $Hg_{1-x}Cd_xTe$ . This method produces a very narrow homogeneous zone in a very short distance, when a steady state is reached.

The use of very high quenching rates [36] induces macroscopic defects such as coring or intergranular precipitates in the crystalline structure. The quench-anneal process can minimize the short-range segregation. Once quenched to a fine grained, reasonably homogeneous alloy free of voids and other mechanical problems, it is necessary to recrystallize into a more or less single-crystal boule from which useful slices for fabrication can be taken. This SSR growth increases the size of grains, but does not improve the long-range homogeneity.

To solve the difficult metallurgical problems of  $Hg_{1-x}Cd_xTe$ , which are the growth of homogeneous, pure, and large oriented crystals, the THM process has been developed [39-41]. This method, which can be considered as a continuous LPE process, allows a crystal to reach a steady state, to benefit from the advantages of low temperature growth, to have its charge purified, and to easily use an oriented seed. In this process, a molten zone is made to migrate through a solid, homogeneous source material by the slow movement of the ampoule relative

to the heater. Matter transport occurs by convection and diffusion across the solvent zone under the influence of the temperature gradient resulting from the movement. THM is known as the most effective technique for achieving material of electronic device grade, i.e., for IR detector arrays, among the bulk crystal growth methods of  $\text{Hg}_{1-x}\text{Cd}_x\text{Te}$ . Although THM has some strong advantages, it cannot produce single crystals larger than 1 inch in diameter within a reasonable amount of time and with a reasonable cost.

### 2.2.2 Epitaxial Layers

Bulk  $\text{Hg}_{1-x}\text{Cd}_x\text{Te}$  crystals grown by different techniques are usually used in the simple detector fabrication of photoconductive or photovoltaic devices. The highest performance of modern devices, however, often requires more sophisticated structures that can only be achieved by epitaxial growth techniques. Epitaxial techniques offer important advantages in comparison with bulk growth, i.e., lower temperatures and mercury vapor pressures, shorter growth times, and reduced precipitation problems which enable the growth of large-area samples with good lateral homogeneity. These advantages make it possible to grow multiple layer structures with sharp interfaces, superlattice, and quantum well structures for possible control of long wavelength tunneling currents. The above advantages have prompted research in a variety of epitaxial techniques, including LPE [11], VPE [12], OMVPE [13], and MBE [42 - 46].

$\text{Hg}_{1-x}\text{Cd}_x\text{Te}$  epitaxial layers are generally grown on lattice matched CdTe or  $\text{Cd}_{1-x}\text{Zn}_x\text{Te}$  ( $x=0.04 - 0.06$ ) substrates. Because of the difficulties encountered in obtaining high quality, large area substrates, several laboratories initiated projects that sought to synthesize an alternate substrate for  $\text{Hg}_{1-x}\text{Cd}_x\text{Te}$ . Cost considerations and the possibility of large-scale production have stimulated interest in hybrid structures for epitaxy, e.g. CdTe epitaxial layers on

commercially available GaAs substrates [42]. The CdTe buffer layer forms a transition region between the substrates and the active layers used for the devices.

At present, LPE is the most mature method of device-quality layer fabrication. Due to the relatively low cost and the simplicity with which a growth apparatus can be assembled on a laboratory scale, LPE has received the most attention. Individualized techniques differ in respect to the melt composition, the methods of bringing the substrate into contact with the melt, and the growth mode. Both Hg and Te are suitable solvents in the LPE growth technique. The major difference between growth in Hg- and Te-rich liquids is that the Hg vapor pressure over the melt is much higher in the former case. LPE growth from Te-rich solution has been carried out more extensively than that from Hg-rich liquids not only because of lower Hg vapor pressure, but also because of the relatively high solubility of Hg and Cd elements in the Te liquid at low temperatures. The partial pressure of Hg must be controlled in the growth system in order to obtain compositional uniformity, reproducibility and stability.

The use of Hg as a solvent has certain advantages: Hg is the purest metal that is readily available, and both *n*- and *p*-type layers with low net doping levels and little deviation from stoichiometry can be grown. The low solubility of CdTe makes the growth rate low and is the reason for melt depletion during growth. This results in composition changes as growth proceeds. The problem can be overcome by the use of large melt mass, which can result in excellent composition uniformity of layers from run to run.

Difficulties in extending best laboratory results for LPE to production scale are well known for  $\text{Hg}_{1-x}\text{Cd}_x\text{Te}$  epilayers [47]. The relatively poor morphology and the difficulties in controlling composition gradients and establishing true heterojunctions in this relatively high temperature growth technique, makes the outlook for reproducible growth of long wavelength photovoltaic arrays uncertain.

ISOVPE for  $\text{Hg}_{1-x}\text{Cd}_x\text{Te}$  crystals was developed in the mid 1960s [48, 49]. In this method, substrate and source are usually placed in parallel to each other in a closed ampoule and then the temperature is elevated to between 450 °C and 650 °C. The growth proceeds because the dissociation partial pressures of Hg and Te over HgTe exceed the equilibrium values of  $\text{Hg}_{1-x}\text{Cd}_x\text{Te}$ . During the deposition process, interdiffusion of deposited HgTe and CdTe occurs, resulting in growth of graded gap  $\text{Hg}_{1-x}\text{Cd}_x\text{Te}$  layers. The composition profile depends on temperature and time of deposition, the Hg pressure and on the system geometry. The optimum growth conditions are reached when the temperature of the growth zone and the pressure of Hg closely approach the Te-rich boundary line.

MBE is well established as a powerful method for growing thin films, quantum well structures, and superlattices. MBE is a material growth technique in which crystalline epitaxial films are grown by depositing atoms layer-by-layer upon a substrate in vacuum. Heated effusion cells produce beams of atoms or molecules which condense on the substrate to form the desired compound. The use of MBE for  $\text{Hg}_{1-x}\text{Cd}_x\text{Te}$  is complicated, in comparison with III-V compounds, by the rapid and incongruent decomposition of material that occurs at elevated temperatures and by the high vapor pressure of Hg necessary to maintain stoichiometric integrity. The very high vapor pressure of Hg limits the substrate temperatures. Above 200 °C, the vapor pressure of Hg is too high to be compatible with MBE, while below about 170 °C the mobility of adatoms on the substrate surface is sufficiently reduced that poor crystallinity results. The electrical, optical and structural properties of  $\text{Hg}_{1-x}\text{Cd}_x\text{Te}$  epilayers indicate their excellent quality within a certain area (9 - 16 cm<sup>2</sup>). Disadvantages of MBE include the high cost and low throughput of present research machines [47]. The slow growth rate of  $\text{Hg}_{1-x}\text{Cd}_x\text{Te}$  alloy due to low Hg sticking coefficient at low temperature, and the

high consumption of elemental Hg are also major difficulties in MBE growth of  $\text{Hg}_{1-x}\text{Cd}_x\text{Te}$  alloys.

### 2.2.3 OMVPE

OMVPE used in this study is a promising epitaxial growth technique because it has the potential for high throughput as well as reduced substrate temperatures compared to LPE. There are several potential advantages of growing  $\text{Hg}_{1-x}\text{Cd}_x\text{Te}$  at a lower temperature using OMVPE growth. Diffusion processes are reduced at lower temperatures, resulting in sharper  $\text{Hg}_{1-x}\text{Cd}_x\text{Te}/\text{CdTe}$  interfaces. The equilibrium density of Hg vacancies decreases sharply with temperature [50]. These Hg vacancies can participate in substitutional diffusion and are sites for incorporation of impurities. Since the equilibrium vapor pressure of Hg over  $\text{Hg}_{1-x}\text{Cd}_x\text{Te}$  depends exponentially on temperature, the use of a lower growth temperature can result in a significant reduction in the consumption of high purity Hg with a concomitant reduction in the generation of toxic mercury waste. Finally the consumption of the expensive and toxic organotellurium compound may be reduced by using a less stable species.

The OMVPE process, applied to  $\text{Hg}_{1-x}\text{Cd}_x\text{Te}$  epilayer growth, involves the use of a carrier gas to transport the organometallic compound of Cd and either vaporized elemental Hg or an organometallic Hg compound with a hydride or organometallic compound of Te into a reaction chamber containing a heated substrate. The gas phase reactant mixture is subsequently pyrolyzed under appropriate experimental conditions of temperature, pressure, and relative concentrations of the reactants to produce the II-VI ternary composition desired. The initial mixing of gaseous reactants normally takes place at room temperature; pyrolysis occurs in the vicinity of the substrate at elevated temperatures (up to ~ 600 °C) in a suitable reaction chamber, with the heated substrate (and/or its

support) normally supplying the required thermal energy to promote the pyrolysis reaction. Somewhat different procedures are required when elemental Hg, instead of an organometallic Hg compound, is used as the reactant.

The  $\text{Hg}_{1-x}\text{Cd}_x\text{Te}$  composition is controlled primarily by the concentration ratios of the reactants used. For example, if DMCD, MATE, and elemental Hg, are used as reactants, as used in this experiment, the simultaneous formation of CdTe and HgTe by pyrolysis in  $\text{H}_2$  produces a  $\text{Hg}_{1-x}\text{Cd}_x\text{Te}$  ternary alloy. The composition is determined by the relative concentrations of the three organometallic compounds or the two organometallic compounds with elemental Hg and by the rates of CdTe and HgTe formation.

The OMVPE process for  $\text{Hg}_{1-x}\text{Cd}_x\text{Te}$  semiconductor thin film growth has several unique advantages. The most important advantage of this process is its tremendous flexibility. Basically simple apparatus design and operating procedures provides a high degree of process control. Multilayer structures can readily be grown on a given substrate in almost any desired combination of composition, thickness, and electrical properties in a single sequence of operations in the same apparatus by appropriate switching of reactants and dopants into and out of the carrier gas stream. The growth chamber, whether of the vertical or horizontal configuration, is typically made of clear fused quartz and thus provides the crystal grower with almost completely unobstructed visual access to the growth site at the substrate surface, at least in the critical early stages of layer growth. Intentional impurity doping of the grown layers, in the form of appropriate organometallic compounds or hydrides, can be accomplished by the simple expedient of adding suitable doping compounds directly to the carrier gas stream along with the main reactants. The handling of reactants is simple because the reactants employed are either gaseous or liquid at room temperature. Only one high-temperature control region is required over the entire reactor system.

The OMVPE process for  $\text{Hg}_{1-x}\text{Cd}_x\text{Te}$  layer growth also has some distinct disadvantages. The most serious one to date has been the difficulty in obtaining organometallic compounds (specifically, metal alkyls) and metal hydrides of adequate purity for use in growth of ultrahigh-purity semiconductors that challenge the best quality produced by other epitaxial growth techniques and fully exploit the inherent potential of the OMVPE process.

There are two OMVPE approaches to  $\text{Hg}_{1-x}\text{Cd}_x\text{Te}$  layer growth; (1) photo- or plasma-assisted and (2) unassisted pyrolytic. The first approach uses photo or plasma stimulation to decompose Cd and Te alkyls. The second approach, which is the one we use, is better suited to uniform  $\text{Hg}_{1-x}\text{Cd}_x\text{Te}$  layer growth because the  $\text{Hg}_{1-x}\text{Cd}_x\text{Te}$  composition is completely controlled by the arrival rate of the growth species at the growth surface. Photo- or plasma-assisted OMVPE, on the other hand, requires simultaneous control of several variables to grow  $\text{Hg}_{1-x}\text{Cd}_x\text{Te}$  alloy with uniform composition. In addition, many impurities contained in Cd and Te alkyls (which contain elements that are electrically active in  $\text{Hg}_{1-x}\text{Cd}_x\text{Te}$ ) will not decompose below 500 °C, unless they are photo- or plasma-stimulated to do so. A more detailed comparison of these approaches, photocatalysis and unassisted pyrolysis, is presented in the table 2.2.

To date, two OMVPE growth techniques for  $\text{Hg}_{1-x}\text{Cd}_x\text{Te}$  materials, using unassisted pyrolytic approach, have been developed for producing layers with high quality and a uniformity in composition that is suitable for large device arrays. These are the interdiffused multi-layer process (IMP) [51-53] and the more traditional direct alloy growth (DAG) [13, 54-57] process. In the IMP process, alternate layers of HgTe and CdTe are sequentially grown under conditions optimized for the respective binaries, then homogenized by heat treatment at higher temperatures. This enables the growth of uniform layers over large area. The lattice mismatch between HgTe and CdTe, however, is about 0.3% and the

**Table 2.2** Process parameter comparison between unassisted pyrolysis and photocatalysis.

<b>Characteristics</b>	<b>Unassisted Pyrolysis</b>	<b>Photocatalysis</b>
Large area uniformity	Uniform $T_s$	Uniform $T_s$ Uniform light intensity
Junction abruptness	Low $T_s$ /High $R_g$	Low $T_s$ /High $R_g$
Thickness control	Control Q	Control Q, $T_s$ , and $I_{light}$
Alloy composition	Control Q	Control Q, $T_s$ , $I_{light}$ and stimulated gas reactions
Background impurities	Reduced incorporation due to low $T_s$	Development of higher purity reactants
Chemical doping	Control Q	Control Q, $T_s$ , $I_{light}$ and light stimulated gas reactions.

possibility of defect generation exists at the CdTe-HgTe interface when the individual layer thicknesses are above a critical value of  $\approx 1500 \text{ \AA}$ . Also the nucleation of CdTe on HgTe may be difficult to control for thin layers of  $\approx 100 \text{ \AA}$ . In DAG process, all precursors are simultaneously introduced into the reactor to grow the  $\text{Hg}_{1-x}\text{Cd}_x\text{Te}$  alloy of the required composition. The control of layer composition over a large area has been reported to be difficult using this process. However, more advanced device structures with abrupt interfaces and uniform doping with depth are easier to achieve with this process.

The first  $\text{Hg}_{1-x}\text{Cd}_x\text{Te}$  epilayers by OMVPE growth technique were made by Irvine *et al.* [13] using a horizontal reactor at atmospheric pressure. Diethyltelluride (DETe), dimethylcadmium (DMCd), and elemental Hg were used as reactants and  $\text{H}_2$  gas as carrier gas. The composition of  $\text{Hg}_{1-x}\text{Cd}_x\text{Te}$  epilayers was from  $x=0$  to  $x=0.3$  at a substrate temperature of  $410 \text{ }^\circ\text{C}$ . After this report, many researchers have concentrated on the development of a repeatable  $\text{Hg}_{1-x}\text{Cd}_x\text{Te}$  ( $0 < x \leq 0.7$ ) photodiode and HgTe/CdTe superlattice growth process, which is important for the high-speed far-infrared detectors that can be operated at or near room temperature. A key requirement for a successful growth process is a low substrate temperature ( $T_s$ ), to reduce defect concentrations and especially to minimize diffusion effects.

In the OMVPE growth of  $\text{Hg}_{1-x}\text{Cd}_x\text{Te}$  the lower limit to the growth temperature is governed by the pyrolyzing efficiency of the tellurium source. Typical growth temperature for  $\text{Hg}_{1-x}\text{Cd}_x\text{Te}$  grown by OMVPE are between  $360 - 400 \text{ }^\circ\text{C}$  using DMCd as the Cd source and diisopropyltelluride (DIPTe) as the tellurium alkyl [58-60]. Stability considerations by Hoke *et al.* [61] have shown that increasing the chain length of the simple alkyls beyond two carbon atoms had very little effect on reducing the decomposition temperature of the alkyl. However, methyl substitution at the  $\alpha$ -carbon atom had a dramatic effect on the useful

growth temperatures for HgTe, typically from 410 °C for DETe and dipropyltelluride (DPTe) to 350 - 370 °C for DIPTe and to 280 - 300 °C for ditertiarybutyltelluride (DTBTe). Instability in the organometallic can also be achieved by introducing unsaturation into the organic group attached to the Te atom. Thus Korenstein *et al.* [62] have grown HgTe at 180 °C using diallyltelluride (DATE) and Lichtmann *et al.* [63] have used MATE to grow CdTe at 250 °C reporting growth rates as high as 30  $\mu\text{m/h}$  at 290 °C. More recently Bhat *et al.* [64] have made a study of the use of MATE growing mainly HgTe although a few preliminary layers of  $\text{Hg}_{1-x}\text{Cd}_x\text{Te}$  were grown. They showed smooth surfaces at 320 °C but detailed characterization of epitaxial quality is not yet available. The stability of these precursors has yet to be fully assessed.

### 3. II-VI OMVPE SYSTEM AND ARIIV REACTOR DESIGN

#### 3.1 OMVPE System

The conventional reactor configuration of  $\text{Hg}_{1-x}\text{Cd}_x\text{Te}$  OMVPE system has shown problems, with respect to reproducibly growing clean, low defect density, large area ( $\geq 14 \text{ cm}^2$ ),  $\text{Hg}_{1-x}\text{Cd}_x\text{Te}$  alloy epilayers having precisely controlled  $x$  ( $0 \leq x \leq 1$ ), with compositional uniformities better than  $\pm 1\%$  of the second decimal place in  $x$  and excellent electrical uniformities ( $\pm 1\%$ ). Since these are necessary for the purpose of this study, we designed and constructed an all stainless steel reactor system and a modified inverted-vertical (IV) chamber (to be discussed in the next section) which can facilitate the delivery of Hg to the growth surface, without sacrificing the uniform growth characteristics obtained in IV reactor; because the thickness, composition and doping uniformities obtained in the IV reactor configuration exceed uniformity requirements for staring arrays [65-67].

The main components of an OMVPE reactor system designed for  $\text{Hg}_{1-x}\text{Cd}_x\text{Te}$  epilayer growth are (1) a source of high-purity carrier gas, in most instances (but not necessarily)  $\text{H}_2$ ; (2) temperature-controlled reactant source bubblers, usually in the form of specially designed stainless steel or commercially available stainless steel; (3) gas flow manifold and control system, including appropriate multiple gas flow paths with suitable valving and electronic mass-flow controllers, for achieving the desired reactant concentrations at the proper times in the substrate region; (4) a reaction chamber made of high-purity fused quartz for good visibility into the layer growth region, enclosing the substrate-supporting fused quartz pedestal and including a means of heating the substrate directly and controlling its temperature; and (5) a gas exhaust line, with appropriate filters for particle removal and provision for burn-off of  $\text{H}_2$  and an evacuation pump for the gas

manifold system. These components are shown schematically in the block diagram in Figure 3.1.

In simplified form, the OMVPE reactor system designed for the growth of epitaxial  $\text{Hg}_{1-x}\text{Cd}_x\text{Te}$  layers on suitable substrates is shown in Figure 3.2. Ultra high-purity  $\text{H}_2$  from a Nano-chem purifier and semiconductor grade Ar were directed, by suitable valving and parallel gas lines, toward a series of electronic mass-flow controllers (MFC). As shown at the center of Figure 3.2, two of these carrier gas paths, after passing through MFC, join the input line of the gas manifold. This input line is connected to the main reactant bubblers of DMCD and MATE and the bubbler of hydrazine ( $\text{N}_2\text{H}_4$ ). The bubblers were maintained by thermostatted refrigeration baths at the desired temperature. Temperature control of the elemental Hg bubbler and the Hg delivery line, extending from the bubbler to the annular chamber ("reactor" in the Figure 3.2), was achieved by wrapping electrical heater tape around both components. This purpose was to prevent Hg condensation in the Hg delivery line, which was  $10^\circ\text{C}$  warmer than the Hg bubbler, during the growth. The reactor in the Figure 3.2 is an inverted-vertical configuration (to be discussed in detail in the next section). The filtered gas exhaust line and burn-off unit at the upper right of particle trap were located at the top of the hood which houses the OMVPE reactor system. The rotary-vane vacuum system was connected to the reactor for system leak checking.

The gas lines of the system were made exclusively of Type 316 stainless steel tubing, which was carefully cleaned and properly pickled and passivated on the interior surface prior to assembly. All permanent joints were formed by heliarc welding, or VCR fittings. Gas-activated solenoid-operated fast-response valves were used exclusively in the manifold system, with a low-dead-space construction to minimize the mass-flow inertia of the gas handling of the system and to

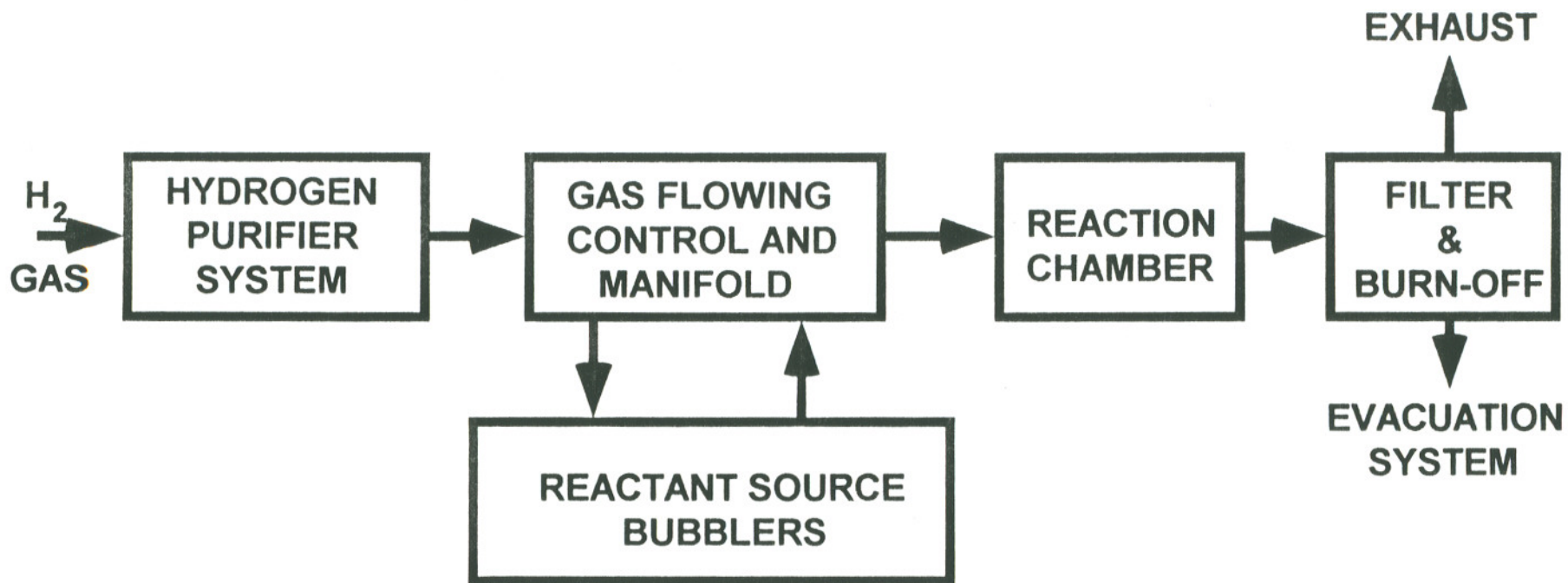


Figure 3.1 Block diagram of OMVPE reactor system for II-VI epitaxial layer growth

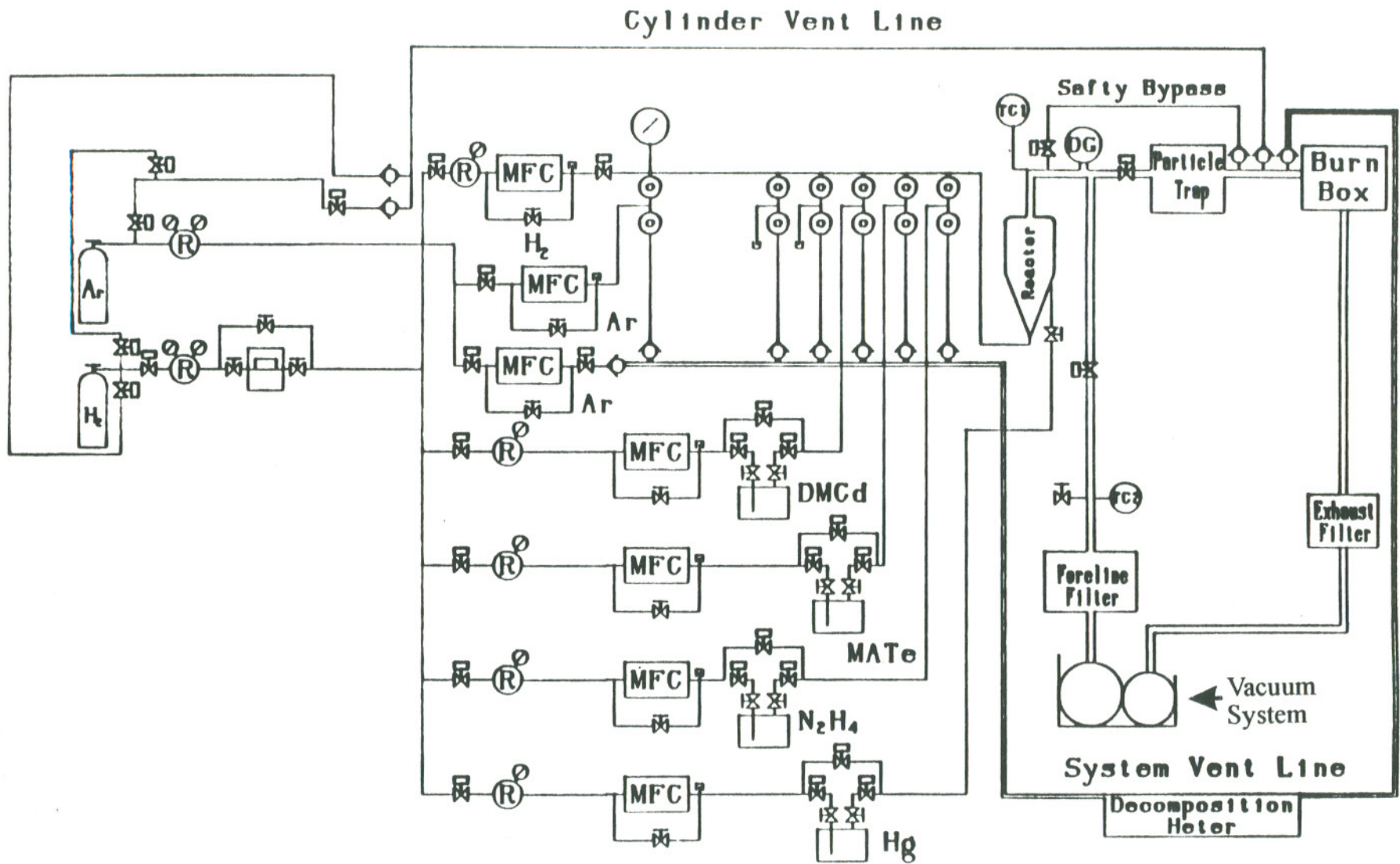


Figure 3.2 Simplified schematic diagram of OMVPE reactor system for II-VI epitaxial growth.

maximize flow-rate control critical to various steps in the OMVPE growth sequence.

### 3.2 ARIIV Reactor Design

There are several fundamental generic problems that have to be overcome in the development of an ideal reactor configuration. The first of these is the intrinsic difficulty of devising a laminar, mass transfer controlled system having a high degree of spatial uniformity. Boundary layer formation in the *entrance regions* would strongly mitigate against achieving such uniformity.

The second of these problems is that in order to achieve thermal decomposition a heated substrate has to be employed; the presence of such heated surfaces will give rise to thermal natural convection, which again tends to produce spatial non-uniformities in the transport rates at the solid surfaces.

The Spire reactor has provided an ingenious solution to this dilemma by seeking to establish a balance between the forced and the buoyancy driven convective flows - achieving good results, but only a partial success. Furthermore, the production of heterostructures with a good degree of abruptness could be quite difficult in such a system.

Numerous recent efforts have been aimed at the utilization of a stagnation flow concept, where a gas stream, possibly a distributed gas stream is made to impinge on a single wafer. These approaches represent promising avenues, but the extent to which the ultimate process objectives can be achieved (i.e. a very high degree of spatial uniformity, in the 1 - 2% range and a high degree of abruptness) is still not clear.

The third problem of conventional  $\text{Hg}_{1-x}\text{Cd}_x\text{Te}$  reactor, whether of the horizontal or the vertical configuration, is the introduction of hot Hg liquid into the upstream portion of the OMVPE reactor that leads to a lack of process control,

because the hot Hg liquid reacts with Te and Cd alkyls. This configuration also should keep the entire reactor warm (about 240 °C), to prevent the elemental Hg condensation in the reactor chamber wall. As result of the hot Hg vapor and the high temperature of hot reactor wall, the pre-crackings of Cd and Te alkyls is produced before the reactant gases reach to the growth surface and causes an unpredictable composition of the  $Hg_{1-x}Cd_xTe$  alloy epilayer.

Considerable attention, therefore, was given to the design of the reactor tube, to facilitate elemental Hg transport to the growth surface in such a way that reactions between hot elemental Hg and organometallics in the system plumbing and upstream portions of the reactor chamber is avoided. Uniformities of thickness, composition and dopant incorporation superior to any other thin film growth process have been demonstrated, repeatably, in the IV reactor [65-67].

The IV reactor assembly includes a reactor tube, a reactor cap, a fused quartz pedestal, a graphite susceptor, and a thermocouple sheath. The key difference between the IV reactor [67] and the ARIIV reactor is the addition of an annular reactant inlet (ARI), shown in Figure 3.3. The Hg delivery approach used here is an important modification to the proven IV reactor design, in order to employ it for  $Hg_{1-x}Cd_xTe$  growth. The unassisted pyrolytic OMVPE approach for  $Hg_{1-x}Cd_xTe$  alloy growth consisted of the utilization of Hg vapor, and Cd and Te alkyls which completely decompose about 100 times faster than their total contact time with a growth surface (substrate) at temperatures of  $\leq 300$  °C. Under these conditions the growth rate is independent of substrate temperature, and it is only necessary to control the flow rates of Hg vapor, and the Cd and Te alkyls in order to control the compositions.

Our unique approach delivers Hg to the growth surface, through an annular reactant inlet, shown in Figure 3.3. This approach permits Cd and Te alkyls to be

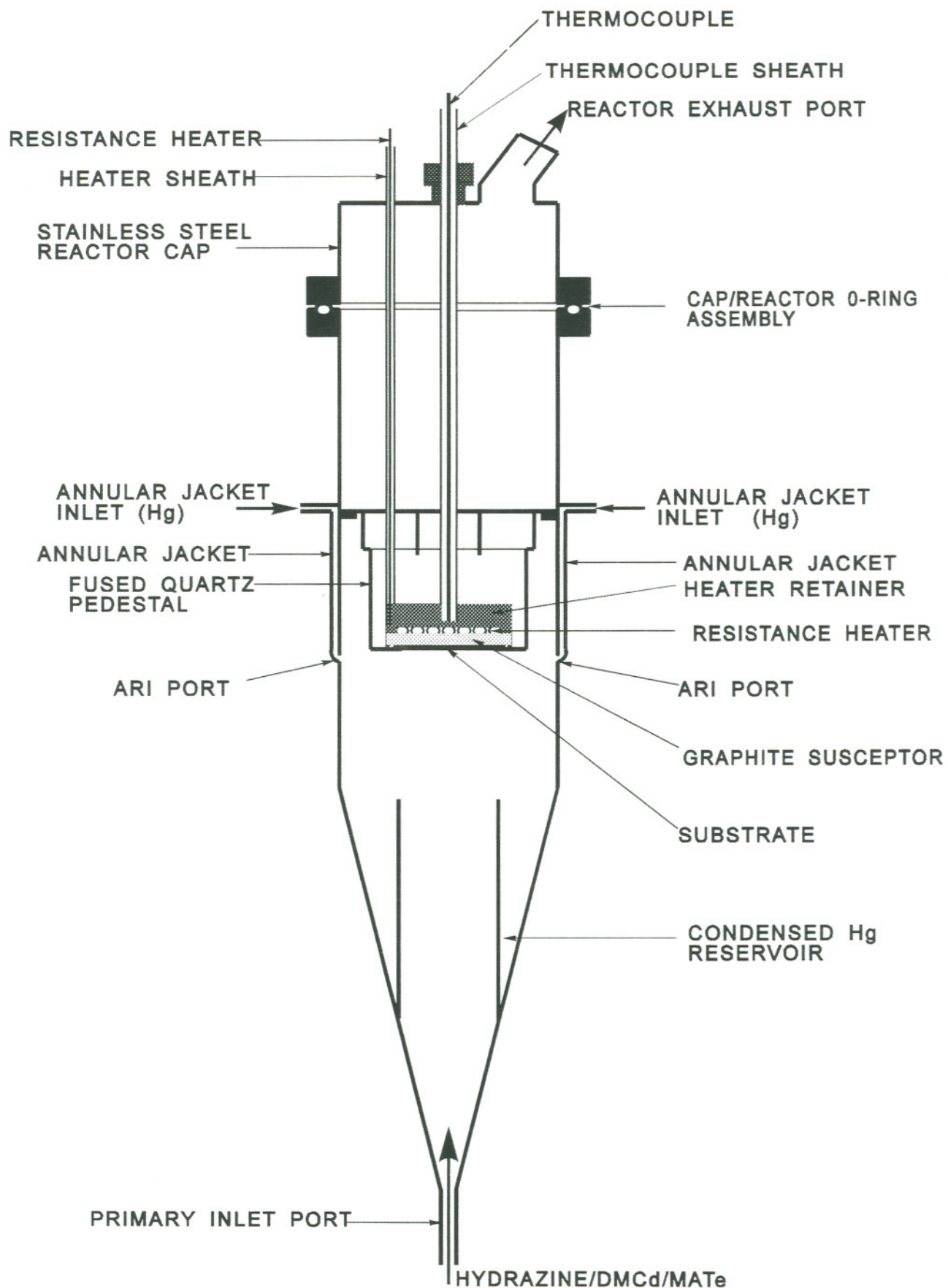


Figure 3.3 Cross-sectional drawing of the ARIIV reactor tube assembly.

introduced in the normal way (from the bottom of the reactor), while heated elemental Hg is introduced into the reactor at the substrate surface through the annular reactant inlet (ARI). This eliminates Hg liquid from the upstream gas flow and increases the impingement of Hg vapor onto the growth surface by a factor of more than 100 for a given Hg vapor flow rate; it also increases the rate at which Hg vapor can be delivered to the growth surface. In addition, this approach facilitates complete mixing of Hg with Cd and Te alkyls over the entire substrate surface.

In the ARIIV reactor, transport of Hg vapor to the ARI port is accomplished by introducing it into an annular reactor tube wall jacket near the top of the reactor. The annular jacket inlet was modified from a single inlet, which was designed at the first stage of system construction, to a double inlet at diametrically opposite locations, in order to provide uniform pressure around the annular jacket. The annular jacket is enclosed by electrical band heater tape to prevent Hg condensation from the jacket wall. The purpose of the vertical offset between the entry port into the jacket and the ARI port is to obtain uniform dispersal of Hg in the jacket before it enters the reactor at the ARI port. The Hg enters the reactor just below the substrate from a 360° arc which lies in a plane perpendicular to the reactor axis. The distance between the outside wall of the reactor tube and the inside wall of the jacket is 2 mm. This cross section is reduced to 1 mm at the ARI port to increase the Hg velocity as it enters the reactor, and to prevent other gases from back-streaming into the ARI port. The ARI port protrudes approximately 1 mm into the reactor and injects Hg into the reactor in a plane perpendicular to the reactor axis.

In the ARIIV reactor arrangement, the inside diameter (ID) of reactor increases from 4 mm at the primary inlet port to a maximum of 89 mm at the top of the funnel shaped portion of the reactor. The angle between the reactor axis

and the reactor tube walls in the funnel shaped portion of the reactor is  $11.5^\circ$ . Above this portion, the reactor the walls are parallel to the reactor axis. An 83 mm ID pedestal support ring is fused to the inner wall of the reactor tube, 70 mm below the mating surface of the reactor tube mating flange. A 45 mm diameter by 105 mm long glass tube is welded to the inside of the reactor, to form a reservoir condensed Hg.

The reactor cap is fitted to the top of the reactor tube by means of mating flanges which are compressionally loaded against a viton gasket to form a vacuum tight seal. A 21 mm ID reactor exhaust port and a 6.3 mm ID thermocouple sheath inlet port are located at the top of the reactor cap. The thermocouple sheath inlet port opening is centered with respect to the reactor tube and it is parallel to the reactor axis. The exhaust port is connected to the system exhaust by a 24 mm ID stainless steel Ultra-Torr fitting. The reactor cap system consists of 316 stainless steel.

The pedestal is a cup-shaped fused quartz cylinder, as shown in Figure 3.4. The pedestal is coaxially supported within the reactor tube by an 86 mm diameter support collar which rests on the top surface of the pedestal support ring. The length and diameter of the pedestal are 59 mm and 74 mm, respectively. The side wall and the bottom surface are 2 mm thick.

The openings in the side wall, at the top of the pedestal, provide a flow path to the reactor exhaust for product gases. This is only one of several possible methods which can be employed to provide a flow path to the reactor exhaust.

The bottom surface (base) of the pedestal has a 46 mm centered circular opening, as indicated in Figure 3.5. The inside surface of the pedestal base has a 0.1 mm deep recess which extends, concentrically, 2.5 mm beyond the 46 mm diameter opening. Substrates (50 to 51 mm diameter) are supported on the 2.5 mm annulus, growth face downward, on the inside bottom of the pedestal. Smaller

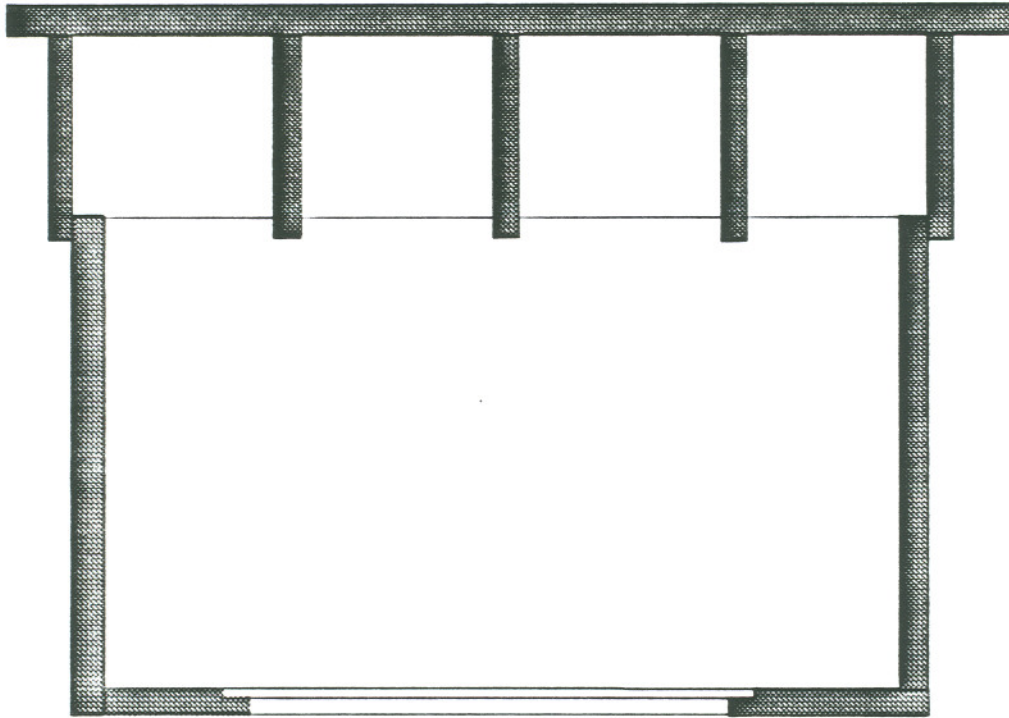


Figure 3.4 Cross-sectional view of fused quartz pedestal.

circular or irregularly shaped substrates are supported on a 51 mm diameter, 1 mm thick molybdenum mask which rests on the 2.5 mm annulus of the pedestal base. In this situation, substrate growth surfaces are exposed to the reactant gases through one or more openings in the mask, as shown Figure 3.5.

Heating is accomplished by a direct resistance pancake heater, which is made of flexible high watt-density electric sheath heater wire coiled in the stainless steel heater retainer. The heater retainer rests on a graphite susceptor which in turn sits directly on the back surface of the substrate and inside the pedestal. The graphite susceptor is 63.5 mm and 57.5 mm in bottom and top diameter, respectively, and 5 mm thick. The bottom of the graphite susceptor also contains a 51 mm diameter concentric recess. A susceptor with a 0.1 mm deep recess is used for mounting 2 inch diameter substrates. The pedestal and susceptor recesses, in conjunction with the substrate (or substrate and mask), form an interlocking arrangement which centers the substrate and susceptor with respect to the reactor tube axis.

In the absence of exhaust pumping, the total flow rate that minimizes back streaming near the reactor tube walls (optimum total flow rate) is determined by the exhaust pressure and by the smallest cross-sectional area through which reactant products must pass, downstream from (above) the primary reactor inlet port. The reactor exhaust pressure for all experiments reported in this paper was 760 Torr. The minimum cross-sectional area for gas flow through the reactor was 3.46 cm<sup>2</sup>, located at the exhaust port. The optimum total flow rate through the reactor is 2.9 standard liters per minute (SLPM). This flow rate minimizes the size of eddy currents, and localizes their position to the reactor tube wall just below the bottom surface of the pedestal.

Another unique aspect of this OMVPE Hg<sub>1-x</sub>Cd<sub>x</sub>Te epilayer growth study, aside from the ARIIV reactor tube, is the hydrazine source, the use of which

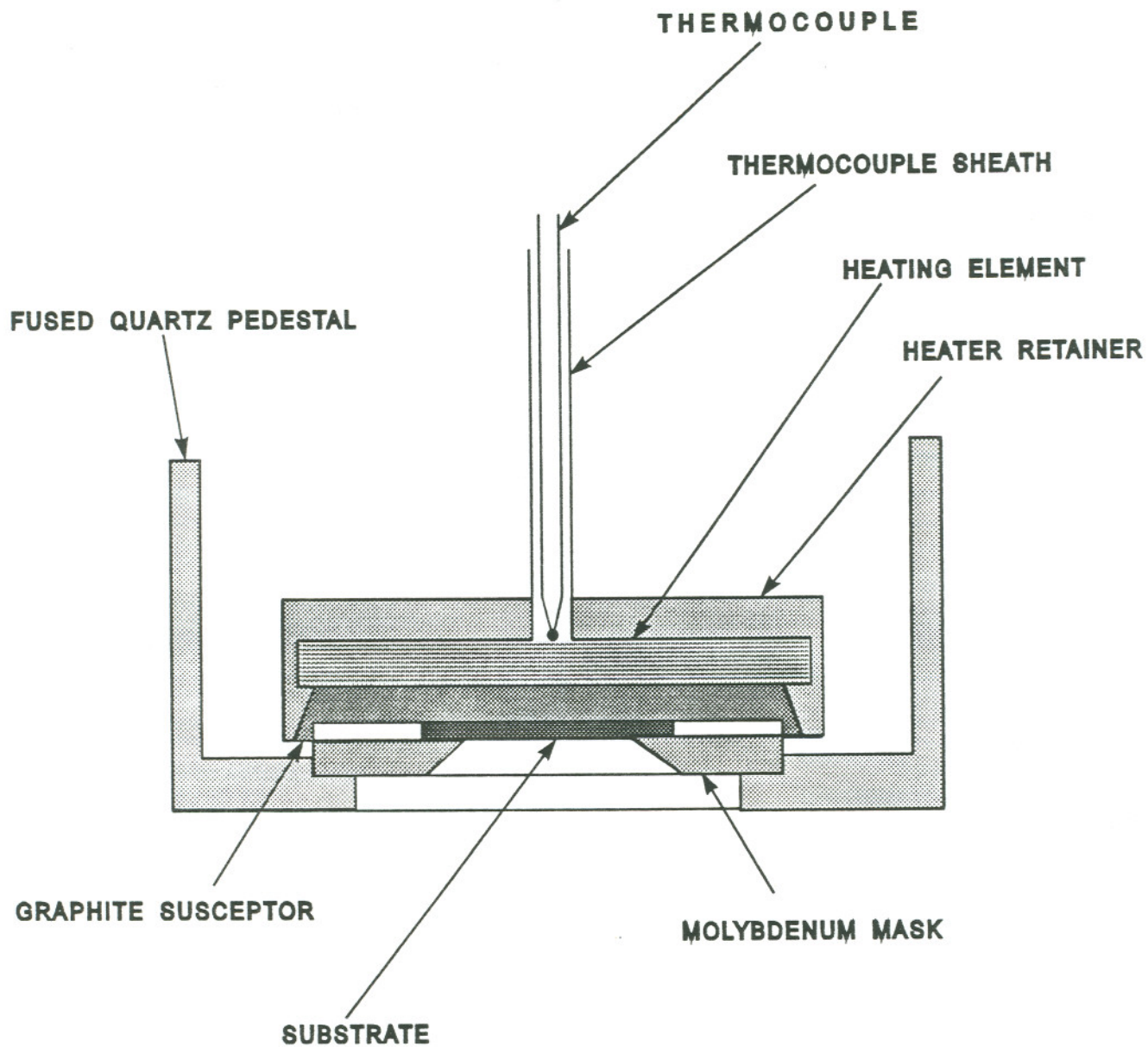


Figure 3.5 Enlarged view of the fused quartz pedestal, substrate, mask, and heater assembly.

results in a profound improvement in  $\text{Hg}_{1-x}\text{Cd}_x\text{Te}$  growth quality, as demonstrated by experiments performed by Dr. Parsons and his group at Hughes Research Labs. This great improvement in results was achieved when a small amount of hydrazine was added to the gas flow to increase the reactivity of Hg at the substrate surface during  $\text{Hg}_{1-x}\text{Cd}_x\text{Te}$  growth. The initial motivation for using hydrazine was to prepare LPE grown  $\text{Hg}_{1-x}\text{Cd}_x\text{Te}$  surfaces for surface passivation coatings. The requirements of this process were that the  $\text{Hg}_{1-x}\text{Cd}_x\text{Te}$  surface, after hydrazine exposure, be clean and that the  $\text{Hg}_{1-x}\text{Cd}_x\text{Te}$  surface concentration must match that of the bulk  $\text{Hg}_{1-x}\text{Cd}_x\text{Te}$ . Hydrazine was chosen because it is an excellent reducing agent, and the atomic hydrogen from the hydrazine molecule reacts with and removes free Te from the  $\text{Hg}_{1-x}\text{Cd}_x\text{Te}$  surface. Results of Electron Spectroscopy for Chemical Analysis (ESCA) measurements showed that hydrazine did an excellent job of cleaning  $\text{Hg}_{1-x}\text{Cd}_x\text{Te}$  surfaces and that it also prevented Hg surface depletion at substrate temperatures up to 300 °C. These results attest that the presence of hydrazine during  $\text{Hg}_{1-x}\text{Cd}_x\text{Te}$  growth: (1) increases the Hg concentration in  $\text{Hg}_{1-x}\text{Cd}_x\text{Te}$  by a factor of 10 for a given Hg vapor concentration at the growth surface, (2) yields  $\text{Hg}_{1-x}\text{Cd}_x\text{Te}$  epilayers with uniform Hg concentrations throughout the epilayer thickness, (3) reduces the carbon and oxygen concentrations in  $\text{Hg}_{1-x}\text{Cd}_x\text{Te}$  to  $< 10^{19}/\text{cc}$  and reduces alkali metal concentrations to  $< 10^{15}/\text{cc}$ , and (4) prevents depletion of Hg near  $\text{Hg}_{1-x}\text{Cd}_x\text{Te}$  epilayer surfaces.

### 3.3 Inverted-Vertical Reactor Design Purpose and Function

The inverted-vertical configuration, wherein reactant gases are introduced below a downward facing substrate and the reactant products are exhausted above the substrate, utilizes the buoyancy effect to remove hot reactant products from the reactor and to suppress the formation of backstreaming eddy currents [67]. The

purpose of the  $11.5^\circ$  angle between the tube wall and the reactor axis is to minimize the dead volume between the inlet port and the substrate. The  $11.5^\circ$  angle was selected because it is the smallest angle that can be reproducibly made by conventional glass shop techniques.

Stagnation point flow and symmetry are the goals of most vertical reactor designs. The IV reactor achieves these goals by virtue of the inverted configuration and the orientation of the substrate surface perpendicular to the gas flow direction. Back-streaming eddy currents do not form at the growth surface because the buoyancy of the hot gases keeps them in contact with a downward facing surface until they are pushed beyond the radius of that surface and permitted to flow in an upward direction.

The reactor exhaust port, in the cap, is not centered with respect to the reactor axis. This asymmetry in the IV reactor design does not effect the growth uniformity when the reactor is used at atmospheric pressure because the pressure gradient in the reactor is created at the inlet port. However, growth uniformity under low pressure operating conditions, where the pressure gradient in the reactor is created at the exhaust port, may require that the exhaust port be concentrically positioned above the pedestal. Concentric positioning of the exhaust port would provide the best possible uniformity in pumping speed about the pedestal radius.

The arrangement of the pedestal, substrate, and susceptor within the reactor performs two functions, aside from the primary function of attaining the IV configuration, which are describe below.

Particulates cannot fall onto the growth surface because the substrate faces downward. Flaking of reactor tube wall deposits rarely occurs, except during very long growth runs, because this reactor tube is designed for cold wall pyrolytic OMVPE growth. When flakes do fall from the reactor tube wall, they remain just above the primary inlet port; where they swirl about in the inlet gas stream. The

flakes do not enter the 4 mm diameter inlet tube until it is disconnected from the 6.3 mm OD stainless steel inlet tube.

Shielding the growth surface from impurities emanating from hot reactor parts is the other function of the pedestal design. The reactant and product gases do not come into contact with any hot surface, except the substrate, until they are downstream from (above) the growth surface. The hot reactor components are located in a region of high velocity (pedestal side walls), or a region of minimal flow (inside the pedestal) which is well isolated from the input gas stream and the growth surface.

## 4. GROWTH AND CHARACTERIZATION PROCEDURES

### 4.1 Substrate and Epilayers Growth Preparation

Growth experiments of CdTe, HgTe, and  $\text{Hg}_{1-x}\text{Cd}_x\text{Te}$  epilayer crystals were performed on 51 mm diameter InSb and 25.4 to 51 mm diameter CdTe substrates. InSb was selected for CdTe epilayer growth study because it has an excellent lattice match ( $\cong 0.05\%$ ) and its thermal expansion coefficient matches that of CdTe. Moreover, it is available in the form of large diameter substrates with good crystal quality. The bulk InSb has fewer defects than CdTe because it is grown at a much lower temperature ( $\approx 530^\circ\text{C}$ ) than bulk CdTe ( $\approx 1090^\circ\text{C}$ ). The full width at half-maximum (FWHM) of x-ray diffraction curves for InSb is typically 10 arc-sec for as-grown materials. The theoretical FWHM of x-ray diffraction curves for CdTe is about 11 arc-sec whereas typical values obtained in high quality, bulk CdTe often exceed 34 arc-sec [68].

High resistivity (100) CdTe wafers,  $5^\circ$  misoriented toward (110), were used as substrate material for epitaxial growth of HgTe and  $\text{Hg}_{1-x}\text{Cd}_x\text{Te}$  layers, in order to study the surface morphologies, the growth rates of HgTe and  $\text{Hg}_{1-x}\text{Cd}_x\text{Te}$  layers, and the electrical studies. InSb (100) substrates were used for CdTe and HgTe growth rates studies. Substrates used for growth runs were degreased in warm trichloroethane (TCE), acetone, and methanol followed by a deionized water rinse and a nitrogen blow dry, before they were chemically etched. Most large area CdTe substrates (larger than  $8\text{ cm}^2$ ) were mechanically repolished for reuse after growth and analysis of  $\text{Hg}_{1-x}\text{Cd}_x\text{Te}$  epilayers, because of the limited availability of CdTe substrates. This procedure was performed by II-VI Crystal Corporation. These reused substrates were degreased in warm TCE, acetone, and methanol for 1 min. each and then chemically etched, to remove the scratched

substrate surface layer, in 2% bromine in methanol solution at room temperature for 20 seconds, followed by a final rinse in deionized water and a dry nitrogen blow, before loading into the reactor. The InSb surfaces were chemically etched in mixture of 63 HF, 36 HAc, and 1.4 HNO<sub>3</sub> solution at room temperature for 14 seconds, followed by a final rinse in deionized water and a dry nitrogen blow.

After loading the substrates, the reactor chamber was first evacuated with a rotary-vane pump, then pressurized to 5 psi with high purity Argon gas (Air Products, research grade) and maintained for 5 min., to check the system for leaks. This procedure was repeated twice and then the reactor chamber was brought to growth temperature under the flow of hydrogen carrier gas (Airco, VLSI grade), which was passed through Nano-Chem 3000 purifier system (Semi-Gas system). The hydrazine, flow rates ( $Q_{NH}$ ) between 0.0012 and 0.012 standard cubic centimeter per minute (sccm), was also introduced at the same time through the primary inlet port of the ARIIV reactor with H<sub>2</sub> carrier gas at the beginning stage of growth runs, in order to etch the substrate internally during the phase of heating the substrate up to growth temperature. When CdTe epilayer growth runs were conducted, 100 sccm H<sub>2</sub> carrier gas was introduced through the Hg delivery inlet to prevent back-streaming into the Hg plumbing.

## 4.2 Cadmium Telluride Growth

The purpose of these experiments was to determine CdTe growth rate as a function of substrate temperature ( $T_s$ ) and MATE alkyl flow rate, and to calibrate the effect of substrate and ratio of the flow rate between DMCD and MATE on surface morphology and crystallinity.

The flow rates of DMCD ( $Q_{Cd}$ ) and MATE ( $Q_{Te}$ ) were stabilized through a vent-run manifold before initiating growth, by simultaneously introducing DMCD and MATE alkyls into the reactor.

One parameter examined in the first CdTe epilayer deposition experiments using the ARIIV reactor was the substrate temperature dependence of the growth rate. The growth rate as a function of  $T_s$  was determined at a constant flow rate ratio of DMCD to MATe between  $290\text{ }^\circ\text{C} \leq T_s \leq 360\text{ }^\circ\text{C}$ . The flow rates of DMCD and MATe precursors were fixed at 0.768 sccm (bubbler maintained at 15 °C) and 0.78 sccm (bubbler maintained at 18 °C), respectively, in these experiments.

The growth rate of CdTe was correlated with ( $T_s$ ), the flow rate of MATe, and the flow rate of hydrogen through the ARI. The purpose of these experiments was to determine the effect of the IV reactor design modifications, and the heating and temperature measurement modifications on results obtained in the IV reactor [63]. Therefore, the growth rate of the CdTe epilayer which was deposited on one quarter of a 2 inch (100) InSb substrate was first evaluated as a function of  $T_s$  by measuring the epilayer thickness on cleaved cross-sections. The CdTe epilayers on (100) CdTe substrates offset  $5^\circ$  towards (110) were also grown for comparison purposes.

The DMCD to MATe flow rate ratio ( $Q_{\text{Cd}}/Q_{\text{Te}}$ ) which yielded the best as-grown surface morphology was determined at  $T_s=300\text{ }^\circ\text{C}$ . The selection of  $T_s=300\text{ }^\circ\text{C}$  was based on HgTe growth results, as discussed below. The pressure during the growth was one atmosphere and the total gas flow through the reactor tube was 2.9 SLPM. The hydrazine, which is a unique reducing agent source in this OMVPE CdTe epilayer growth, was also introduced at the same time through the primary inlet of the reactor tube at a hydrazine flow rate of 0.011 sccm (bubbler maintained at 15 °C).

### 4.3 Mercury Telluride Growth

The HgTe experiments were performed to determine the growth rate of HgTe epilayer as a function of the flow rate of MATe alkyl, the maximum of Hg to Te

ratio that would yield stoichiometric HgTe (free of Te precipitation), and the growth temperature of  $\text{Hg}_{1-x}\text{Cd}_x\text{Te}$  epilayer based on Hg reactivity and vapor pressure properties and pedestal position.

The flow rate of Hg was controlled by the Hg bubbler temperature and the flow rate of  $\text{H}_2$  carrier gas through it. Hg vapor was transported from the bubbler to the inlet port of the annular jacket leading to the ARI port, through 6.4 mm plumbing. The temperature of the plumbing and the annular jacket were kept at least 10 °C higher than the Hg bubbler temperature ( $290 \leq T \leq 310$ ), to prevent Hg condensation on the plumbing and jacket walls. The maximum temperature of the reactor tube wall below the substrate - which was heated by thermal conduction from the annular jacket wall - was less than 90 °C. The hydrazine flow rate of 0.012 (bubbler temperature was increased to 18 °C) was introduced through the primary inlet of the reactor tube in the HgTe epilayer growth experiments. The pressure during the growth run was one atmosphere and the total gas flow through the reactor tube was maintained at 2.9 SLPM.

The ratio of Hg to MATe flow rate which yielded HgTe layers which were not Te rich were determined at  $T_s=300$  °C. The optimum position of substrate which maximize the growth rate of HgTe epilayer was 6.3 mm above the plane of the ARI.

#### 4.4 Mercury Cadmium Telluride Growth

The growth rate and composition of  $\text{Hg}_{1-x}\text{Cd}_x\text{Te}$  epilayers were determined as a function of Cd flow rate at constant Hg flow rate, MATe flow rate, and  $T_s$ . The initial growth runs of  $\text{Hg}_{1-x}\text{Cd}_x\text{Te}$ , therefore, were made with a variation of the Cd flow rate,  $0.0755 \text{ sccm} \leq Q_{\text{Cd}} \leq 0.215 \text{ sccm}$  (bubbler maintained at 10 °C), at the following fixed parameters: the Hg flow rate of 226 sccm (bubbler maintained at

315 °C), flow rate of MATe of 1.55 sccm (bubbler maintained at 18 °C), and  $T_s=300$  °C.

The reason that above parameters were was that these constant parameter gave the highest growth rate of HgTe and the Cd flow rate would control the composition of  $Hg_{1-x}Cd_xTe$  epilayer. After several growth runs of  $Hg_{1-x}Cd_xTe$ , it was found that the small amount of DMCD flux in the gas phase determined the composition of  $Hg_{1-x}Cd_xTe$  epilayer and the surface morphology.

The growth rate of the  $Hg_{1-x}Cd_xTe$  layer as a function of  $T_s$  and a function of MATe flow rate was also determined over a wide range of growth conditions, in order to establish the optimum growth conditions for  $Hg_{1-x}Cd_xTe$  epilayer, based on each growth run result. These growth experiments also gave two important interactions; (1) the substrate temperature determined the composition of as-grown  $Hg_{1-x}Cd_xTe$  epilayers due to the reactions between DMCD alkyl and the increasing cracking rate of MATe alkyl with increasing temperature, and (2) the growth rate of  $Hg_{1-x}Cd_xTe$  epilayers at higher  $T_s$  ( $300$  °C  $< T_s \leq 330$  °C) increased as the MATe flow rate increased, but was lower at  $T_s=300$  °C due to the lower elemental Hg sticking coefficient with increasing temperature.

The optimum relationship between the relative flow rate and Hg concentrations ( $0.2 \leq x \leq 0.3$ ) of  $Hg_{1-x}Cd_xTe$  epilayers was determined, based on the above results, and then the maximum growth rate conditions of  $Hg_{1-x}Cd_xTe$  epilayer were fixed. The reason for focusing on a particular Hg concentration was that this composition range of  $Hg_{1-x}Cd_xTe$  crystals is used for IR detectors and that this would minimize the number of experiments required.

The optimum conditions which could produce the maximum growth rate of  $Hg_{1-x}Cd_xTe$  with  $x \cong 0.2$  were determined as a function of DMCD flow rate; where the flow rates of Hg and MATe were 174 sccm and 1.55 sccm, respectively, and  $T_s$  was 300 °C, and the pedestal was positioned such that the

substrate surface was 6.3 mm above the plane of the ARI. The flow rate of hydrazine (maintained at 18 °C) was 0.012 sccm. The pressure during the growth run was one atmosphere and the total gas flow through the reactor tube was again maintained at 2.9 SLPM, as in the case of CdTe and HgTe growth.

#### 4.5 Characterization Procedures

The single crystallinity of CdTe, HgTe, and  $\text{Hg}_{1-x}\text{Cd}_x\text{Te}$  epilayers grown on InSb or CdTe substrates was confirmed by employing electron contrast channeling patterns (ECCP). The shape or the symmetry of the bright band in ECCP reveals the orientation of the crystal, the width of the bright band reveals the lattice constant (from which the composition of the crystal can be calculated), and the sharpness of the bright band indicates the crystalline quality of the material. The working distance (the distance from the point source to the sample) employed in the ECCP study was 20 mm and the magnification was 15x in the back scattering electron mode.

Thin epilayers of  $\text{Hg}_{1-x}\text{Cd}_x\text{Te}$  (approximately 1000 Å thick to facilitate ellipsometric measurement, because of the absorption of 6328 Å light in  $\text{Hg}_{1-x}\text{Cd}_x\text{Te}$ ) grown on 20 cm<sup>2</sup> CdTe were analyzed by multiple angle of incidence (MAI) ellipsometry [67, 69, 70], using a 0.6328 μm He-Ne laser light source. MAI ellipsometry technique was employed to analyze the thin epilayer (≤1500 Å) composition and compositional uniformity, epilayer thickness and the thickness uniformity, and substrate/epilayer interface abruptness.

The MAI ellipsometry technique is a far more powerful tool for analysis of optically transparent thin films than the standard single angle of incidence ellipsometric technique. A computer program has been developed which permits simultaneous determination of thickness, refractive index (real and imaginary) and birefringence in 3 layers, which are initially assumed to be present. In this case

the 3 layers which will be anticipated, and analyzed if they exist, are (1) a surface contamination layer, (2) the as-grown  $\text{Hg}_{1-x}\text{Cd}_x\text{Te}$  layer, and (3) an interface layer between the  $\text{Hg}_{1-x}\text{Cd}_x\text{Te}$  layer and the substrate.

The composition of as-grown  $\text{Hg}_{1-x}\text{Cd}_x\text{Te}$  layers ( $\geq 3 \mu\text{m}$ ) was determined by a dual beam Fourier transform infrared (FTIR) spectrophotometer. A CdTe substrate was placed in the reference beam to compensate for the transmission from the substrate. The sharpness of the absorption edge of the FTIR spectrum indicates that the layer is reasonably uniform both across the layer and with depth. The periodicity of the interference pattern is directly related to layer thickness, which is given by Equation 2.2 in Chapter 2. The composition of the as-grown  $\text{Hg}_{1-x}\text{Cd}_x\text{Te}$  layer, which is related to the band gap of the  $\text{Hg}_{1-x}\text{Cd}_x\text{Te}$  crystal, was estimated from the measured thickness and the FTIR transmission curve by taking the energy at which  $\alpha=500 \text{ cm}^{-1}$ . The revised empirical relation between the composition and the band gap in the composition range of  $x \leq 0.6$  and  $x=1$ , which is the Equation 2.1[17] in Chapter 2, was employed for the as-grown  $\text{Hg}_{1-x}\text{Cd}_x\text{Te}$  layers.

The morphology of the  $\text{Hg}_{1-x}\text{Cd}_x\text{Te}$  epilayers was examined using a Nomarski contrast microscope and scanning electron microscopy (SEM). Epilayer thickness measurements were also performed by these techniques, which are more accurate than FTIR measurements. Growth rates of CdTe/InSb, HgTe/CdTe or InSb, and  $\text{Hg}_{1-x}\text{Cd}_x\text{Te}/\text{CdTe}$  were determined by measuring the epilayer thickness after the sample was cleaved and the cross-section etched using defect etchant (to be discussed below). The crystalline properties of as grown epilayers were evaluated using double crystal x-ray diffraction (DCXRD).

The crystal defects of as-grown  $\text{Hg}_{1-x}\text{Cd}_x\text{Te}$  epilayer were examined using defect etchant. The most common etchants used for the determination of the dislocation density is  $\text{HF} + \text{H}_2\text{O}_2 + \text{H}_2\text{O}$  [71, 72] for CdTe and  $\text{HNO}_3 + \text{HCl} +$

$\text{H}_2\text{O} + \text{Br}_2$  in  $\text{CH}_3\text{OH}$  or  $+\text{Br}_2$  in  $\text{CH}_3\text{COOH}$  for  $\text{Hg}_{1-x}\text{Cd}_x\text{Te}$  [73]. These defect etchants are known to develop etch pits on only one of the crystallographically opposite (111) surfaces. The Polisar etchant [73] produces etch pits on any plane of  $\text{Hg}_{1-x}\text{Cd}_x\text{Te}$  crystals. A mixture of  $\text{HCl}$ ,  $\text{HF}$ , and chromic acid was proposed for (110) plane of  $\text{Hg}_{1-x}\text{Cd}_x\text{Te}$  [74]. These reported etchants were unsuitable for  $\text{Hg}_{1-x}\text{Cd}_x\text{Te}$  epilayers grown on (100)  $\text{CdTe}$  with  $5^\circ$  offset towards (110) plane, in contrast to those reported by Hähnert *et al* [75]. Therefore, Hähnert etchants were used for the studies of distribution of crystallographic defects.

The etchant for  $\text{Hg}_{1-x}\text{Cd}_x\text{Te}$  epilayer has a basic composition consisting of 1  $\text{HF}$ , 1  $\text{CrO}_3$  (50 wt%  $\text{CrO}_3$  in  $\text{H}_2\text{O}$ ), and 1  $\text{HCl}$ . This mixture was diluted with deionized water. It was found that a dilution of 10 times produced etch pits on the  $\text{Hg}_{1-x}\text{Cd}_x\text{Te}$  epilayers ( $0.0 \leq x \leq 0.4$ ). For the etching procedure, the samples were dipped and stirred in the etching solution for 5 min.

Electrical properties for as-grown  $\text{Hg}_{1-x}\text{Cd}_x\text{Te}$  epilayer were characterized by Hall effect measurements using the van der Pauw technique at temperature variation of 50 - 300 K. Hall effect measurements were performed on  $5 \times 5 \text{ mm}^2$  sections cleaved from as-grown  $\text{Hg}_{1-x}\text{Cd}_x\text{Te}$  epilayers, in order to determine carrier type, carrier concentration, and carrier mobility. Indium point (dot) contacts, 0.3 - 0.5 mm in diameter, were used for the four corners of thin layers using a soldering iron with a small tip. A magnetic field from 1 to 3 K gauss was applied during the Hall effect measurements. The measurements and the calculations were performed by a computer.

## 5. EXPERIMENTAL RESULTS AND DISCUSSION

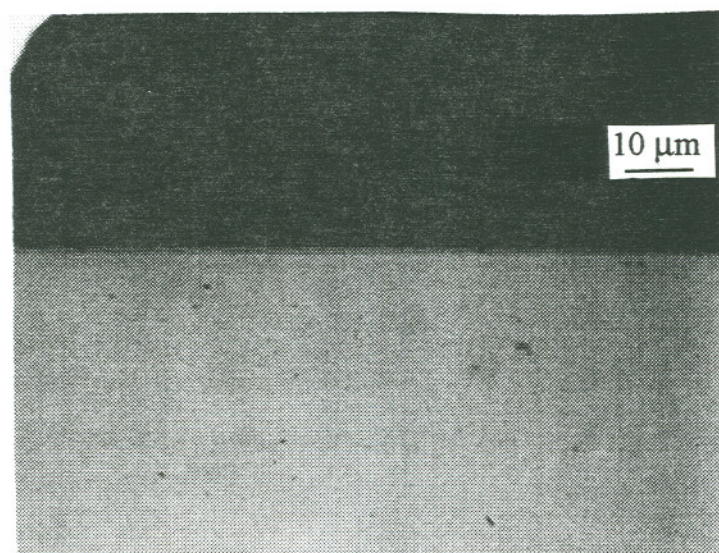
### 5.1 CdTe Epilayer Growth

The cleaved cross-sections used to measure the growth rate of CdTe using a Nomarski contrast microscope is shown in Figure 5.1. The growth rate, plotted in Figure 5.2, increased from 0.5  $\mu\text{m/h}$  at 290  $^{\circ}\text{C}$  to 3  $\mu\text{m/h}$  at 360  $^{\circ}\text{C}$ . The increase in CdTe growth rate with increasing substrate temperature is due to the  $T_s$  dependent decomposition rate of MATE alkyl.

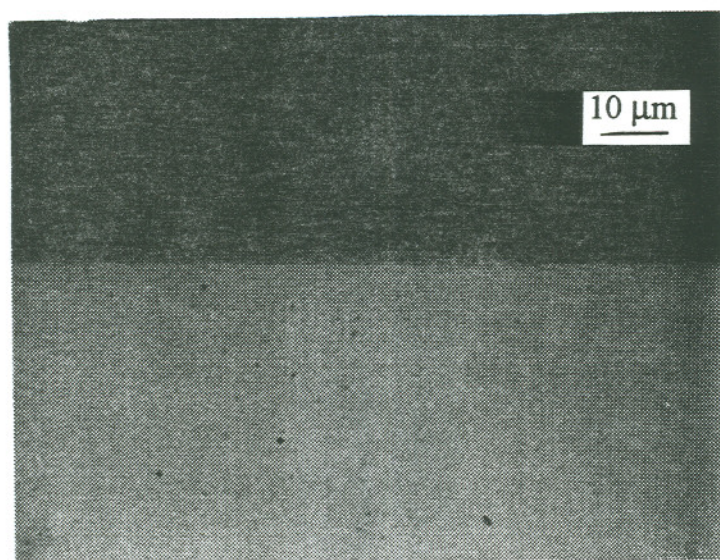
Substrate temperature independent CdTe growth rates were obtained at or above 360  $^{\circ}\text{C}$ . The 60  $^{\circ}\text{C}$  difference in temperature at which  $T_s$  independent CdTe growth rate was obtained in this work, relative to that reported for the IV reactor in reference [65], is attributed to inaccurate  $T_s$  measurement in reference [65]. The accuracy of  $T_s$  measurements reported here were determined to be within  $\pm 1$   $^{\circ}\text{C}$  of the actual  $T_s$  in the following manner. An assembly consisting of a thermocouple (type K: Chromel-Alumel, 0.0762 mm diameter) junction, placed between two 51 mm diameter Si wafers, was mounted in the ARIIV reactor. The substrate temperature was measured in a  $\text{H}_2$  flow rate of 2.9 SLPM through primary inlet port.

The growth rate of CdTe epilayers on InSb substrates increased sublinearly from 3  $\mu\text{m/h}$  to 11  $\mu\text{m/h}$  as the flow rates of hydrogen carrier gas through the bubblers of DMCD and MATE were quadrupled at 360  $^{\circ}\text{C}$ . This result is plotted in Figure 5.3.

The flow rate of diluent  $\text{H}_2$  through the ARI port ( $Q_{\text{H}_2} \leq 1100$  sccm) had no measurable affect on the growth rate of CdTe epilayer. This was confirmed by performing CdTe growth experiments, at identical flow rate and  $T_s$  conditions, in the ARIIV and in the IV reactor configurations.



(a)



(b)

**Figure 5.1** Cleaved cross-sections used to measure the thickness of CdTe/InSb using Nomarski contrast; (a)  $T_s=290$  °C and (b)  $T_s=300$  °C.

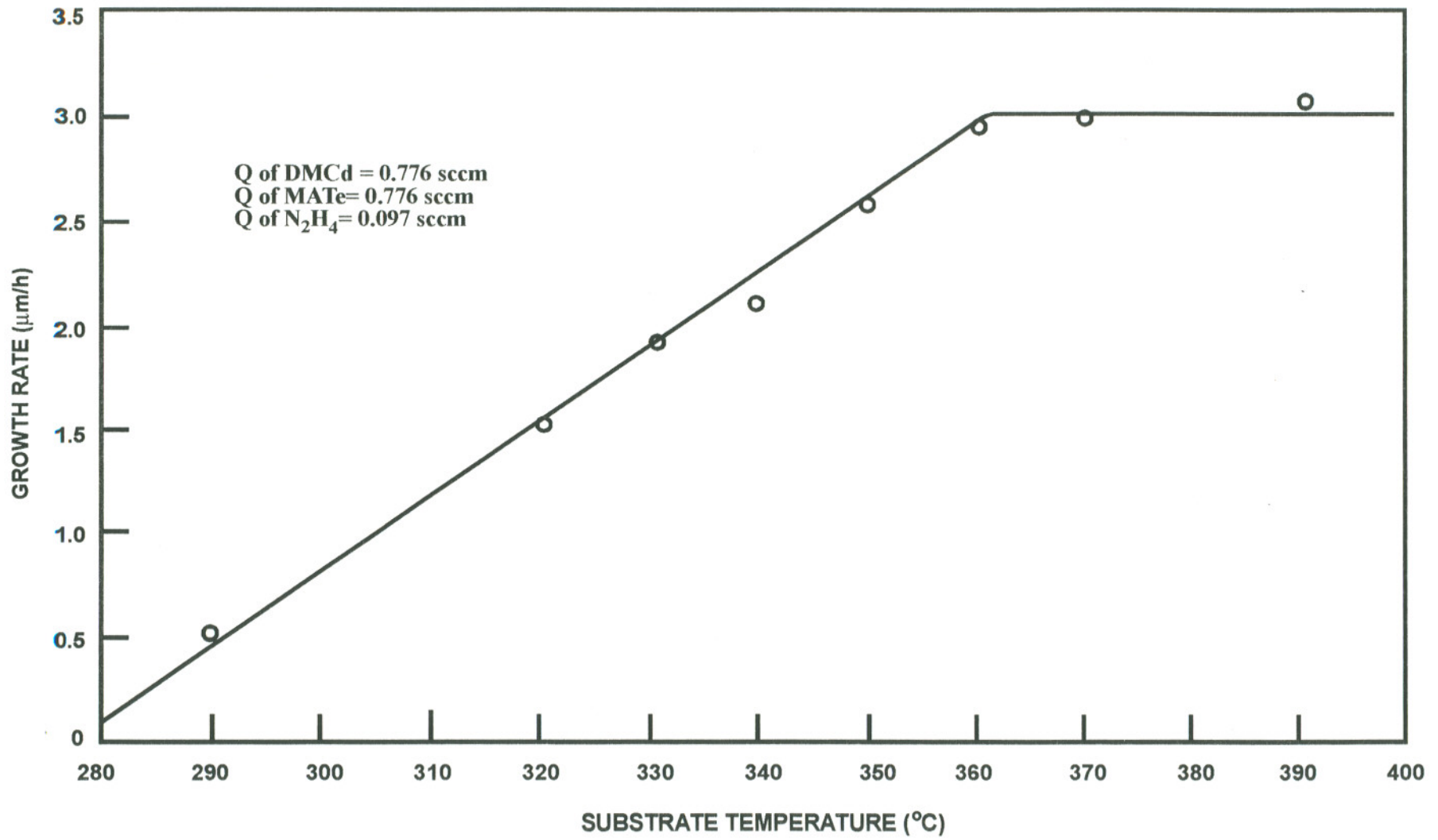


Figure 5.2 Growth rate of CdTe epilayer as a function of substrate temperature.

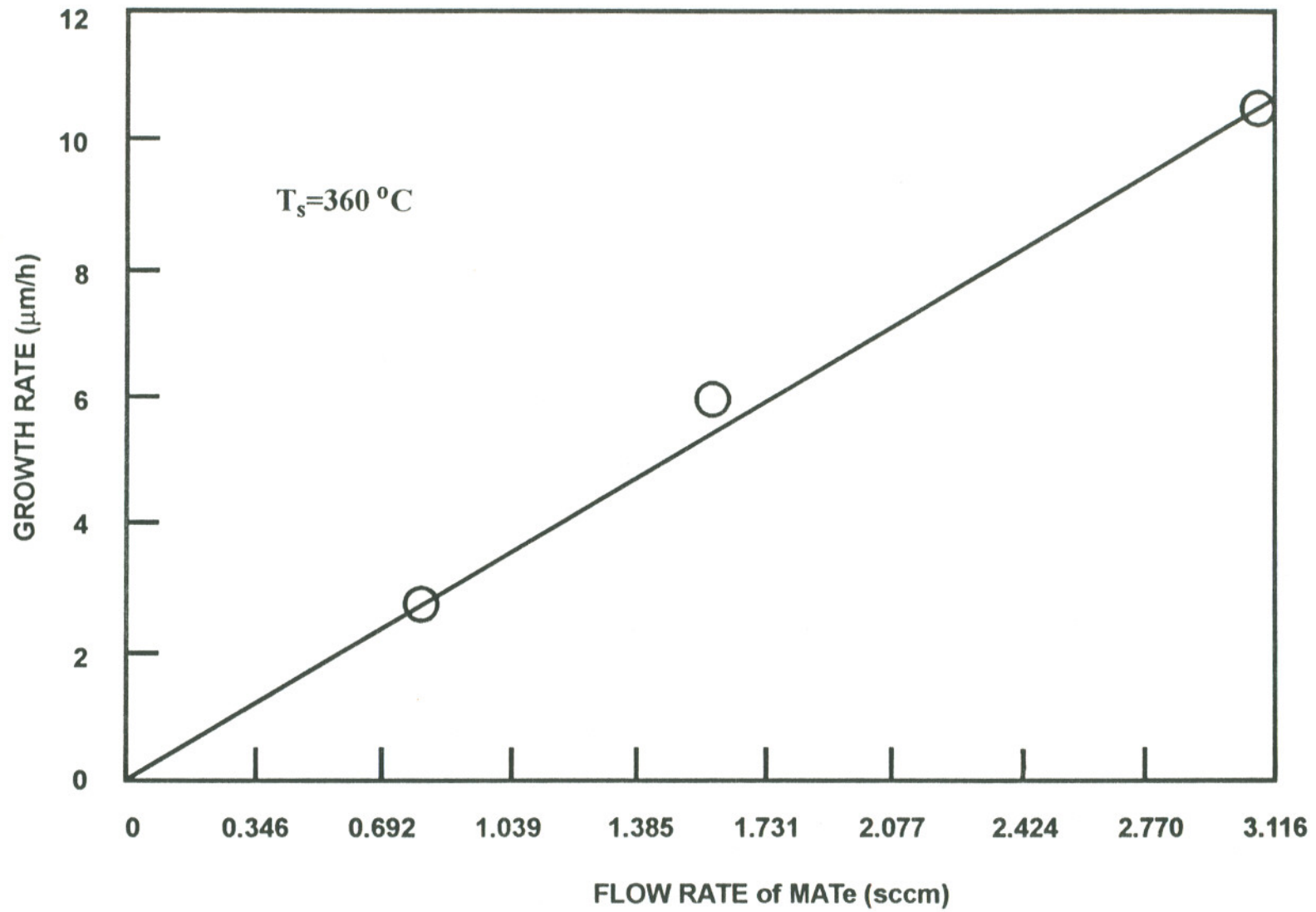


Figure 5.3 Growth rate of CdTe epilayer as a function of the flow rate of MATE .

The crystal quality of CdTe epilayers grown on InSb substrates was evaluated using the DCXRD measurement technique. An example of the DCXRD of 3  $\mu\text{m}$  thick CdTe film grown on a (100) InSb substrate at 360  $^{\circ}\text{C}$  is shown in Figure 5.4. The CdTe epilayer had the same orientation as the (100) InSb substrate. The peak position of the rocking curve of the CdTe epilayer, with respect to the InSb substrate peak, gives an estimate of the lattice mismatch between two materials. In Figure 5.4, multiple peaks due to the presence of low-angle grain boundaries are absent, and the FWHM of the CdTe epilayer rocking curve peak was 92 arc-sec.

This broad angle, compared to the high quality of CdTe/InSb epilayers grown by MOCVD [76] and MBE [77], supports the assumption that the FWHM intensity of the peak can be broadened by misorientation and by the lattice strain of the film in the layer [78]. In addition, it should be noted that the FWHM of the InSb substrates prior to deposition were typically in the 30 to 60 arc-sec range, which are not high quality InSb substrates, and the growth of the films almost doubled this value.

CdTe epitaxial layers at  $T_s = 360$   $^{\circ}\text{C}$  were also grown on (100)  $\rightarrow$  5 $^{\circ}$  (110) CdTe for comparison purposes. It was found that the layers grown on CdTe substrates consistently showed superior morphology to those grown on InSb substrates.

The ECCP photo of the CdTe layer, which confirms the single crystallinity of the layer, is presented in Figure 5.5. About 1 cm wide one-fold bright bands can be seen on the ECCP picture, but the bright bands are not clear enough to be used for calculating composition or comparing crystalline quality of the CdTe epilayer. The reason for the vague ECCP is believed to be due to the limitation of SEM equipment, namely, the electron source of scanning deviates too strongly from the ideal point source.

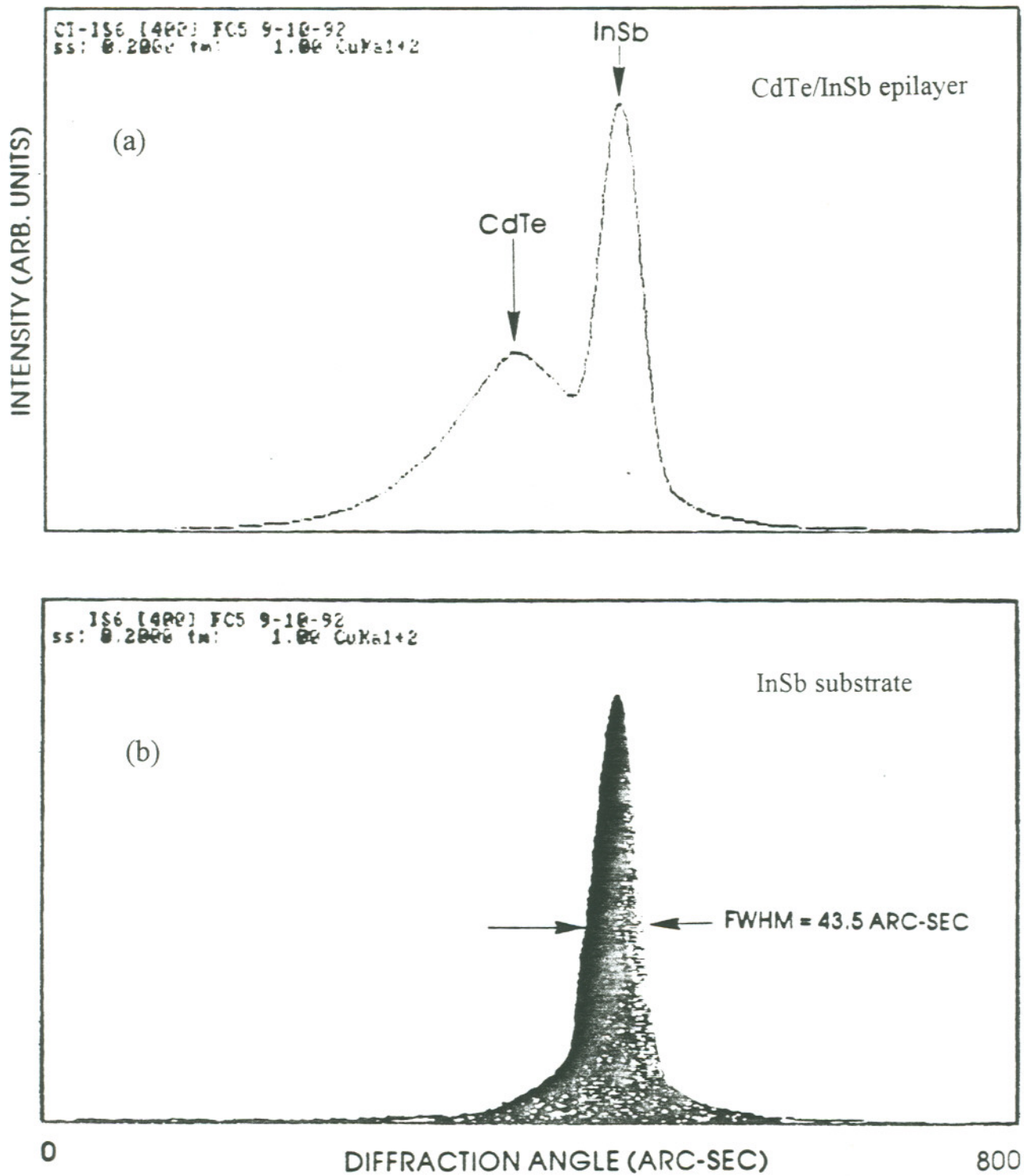
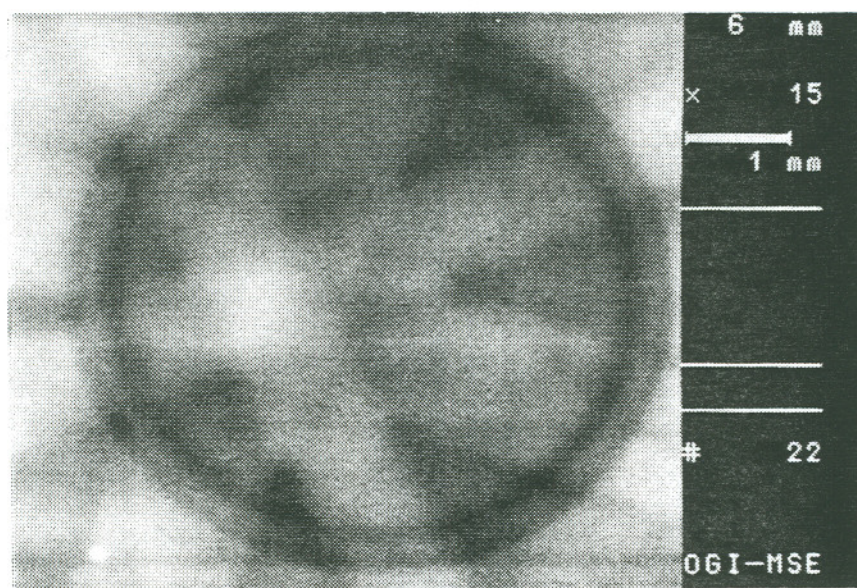


Figure 5.4 Double crystal x-ray rocking diffraction curves for (a) CdTe/InSb epilayer and (b) InSb substrate.



**Figure 5.5** Electron channeling contrast pattern of CdTe epilayer.

The crystal orientation of CdTe epilayers grown on (100) CdTe substrates offset  $5^\circ$  towards (110) at  $T_s = 360^\circ\text{C}$  was also studied as a function of ratio of DMCD to MATE flow rate ( $0.5 \leq Q_{\text{Cd}}/Q_{\text{Te}} \leq 1$ ). Under these conditions, all as-grown CdTe epilayers with different Cd to Te alkyl flow rate showed the same orientation as the substrates, which were analyzed using x-ray diffraction pattern measurements prior to being loaded into the reactor chamber. An example of DCXRD of an as-grown mirror-like CdTe epilayer with  $3\ \mu\text{m}$  thickness is shown in Figure 5.6. The CdTe substrates used for the II-VI epilayer growths showed two main peaks, which were caused by subgrain boundaries of substrate, as shown in Figure 5.6 (b), which is not acceptable in substrates for high quality epilayers. These poor quality CdTe substrates resulted in large FWHM, as shown in (a) of Figure 5.6.

The evaluation of the surface smoothness (morphology grade) of CdTe epilayers grown at  $T_s = 360^\circ\text{C}$  as a function of the ratio of DMCD to MATE flow rate is shown in Figure 5.7. The grades (1 is the best, shiny and mirror-like surface, and 3 the worst, milky, brownish and black surface) shown in Figure 5.7 were determined by Nomarski contrast microscope. Most CdTe epilayers had smooth, mirror-like surfaces, but the CdTe layer with a ratio of 0.75 showed the best surface morphology. A light milky surface morphology was obtained at  $Q_{\text{Cd}}/Q_{\text{Te}}$  greater than 0.75. Brownish, faceted surfaces were obtained at  $Q_{\text{Cd}}/Q_{\text{Te}}$  less than 0.5. A difference in the growth rate of CdTe epilayer was not observed at  $0.5 \leq Q_{\text{Cd}}/Q_{\text{Te}} \leq 1$ .

Some CdTe layer surfaces contained microterraces, hillocks, and pits, which are characteristic of the (100) orientation and appear to be associated primarily with improper surface cleaning, or physical defects in the substrate surface [79]. The microterraces in this study, however, were usually observed at  $Q_{\text{Cd}}/Q_{\text{Te}}$  lower

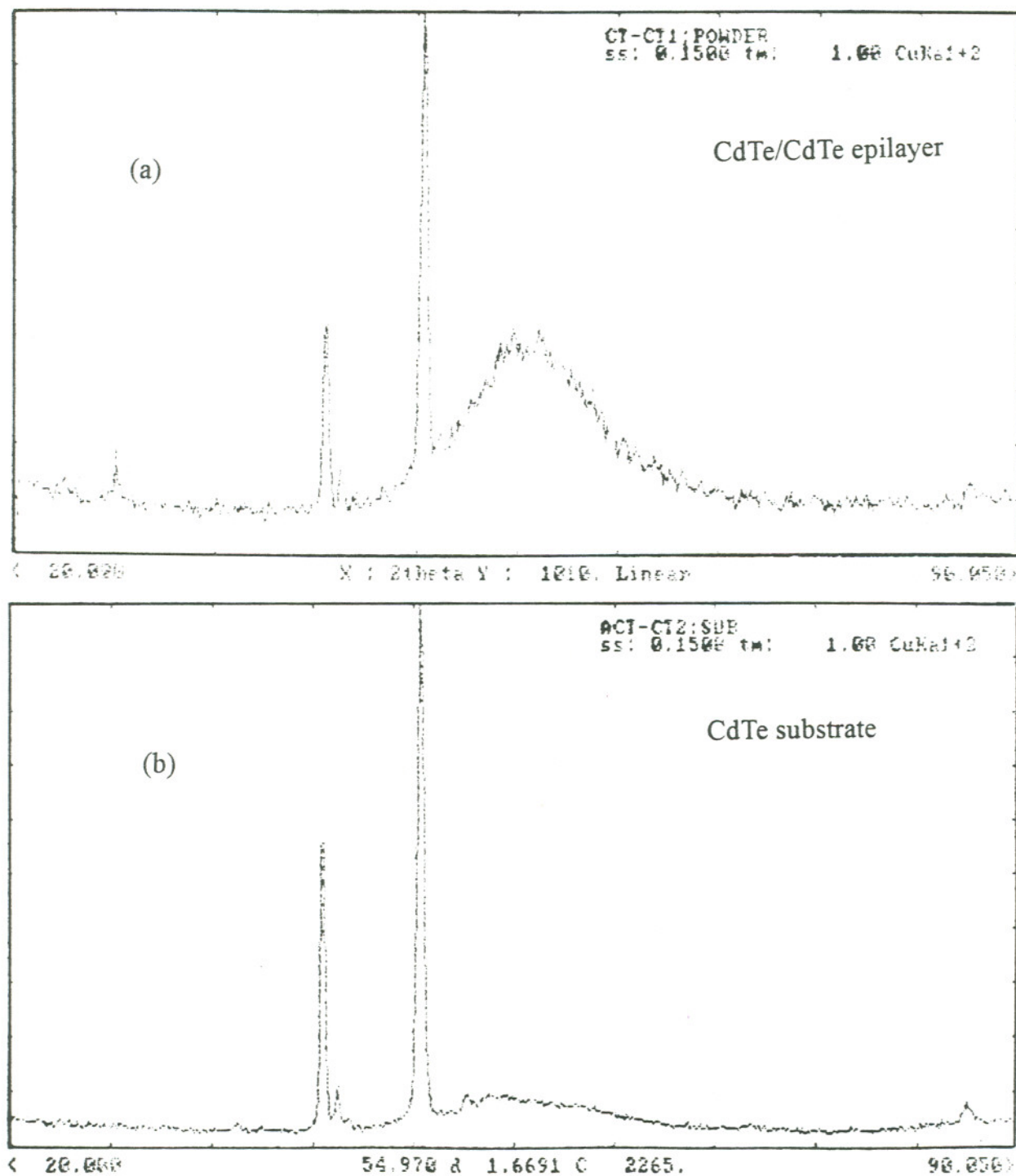


Figure 5.6 Double crystal x-ray rocking diffraction curves for (a) CdTe/CdTe epilayer and (b) CdTe substrate.

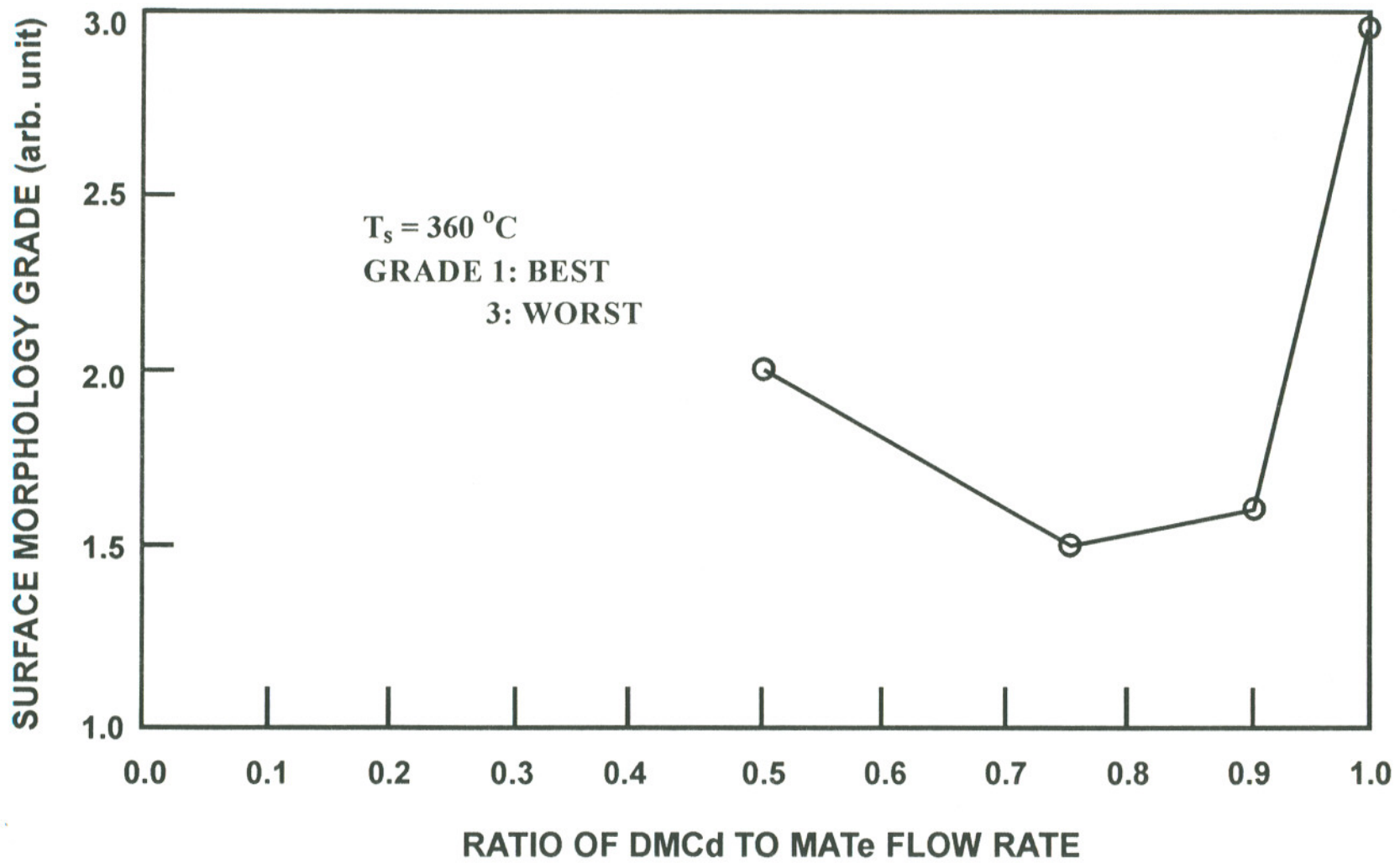


Figure 5.7 Surface morphology grade as a function of ratio of DMCd to MATE flow rate.

than 0.6 and the pits at  $Q_{\text{Cd}}/Q_{\text{Te}}$  greater than 0.8, as shown in Figure 5.8. As-grown CdTe layers with physical defects showed hazy surface structure at the initial stage, but this feature diminished as growth proceeded and then the layers became very smooth after about 2  $\mu\text{m}$  of growth.

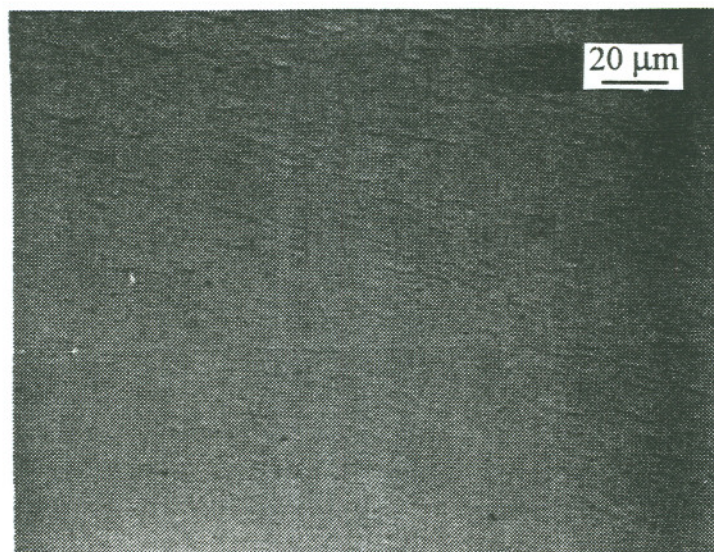
## 5.2 HgTe Epilayer Growth

The growth rate of HgTe was determined as a function of  $T_s$  in the temperature range between 290 - 330  $^{\circ}\text{C}$ . The flow rates of elemental Hg and MATE were fixed at 226.0 sccm (bubbler maintained at 315  $^{\circ}\text{C}$ ) and 1.55 sccm (bubbler maintained at 18  $^{\circ}\text{C}$ ), respectively. These growth conditions yielded HgTe epilayers with mirror-like surfaces.

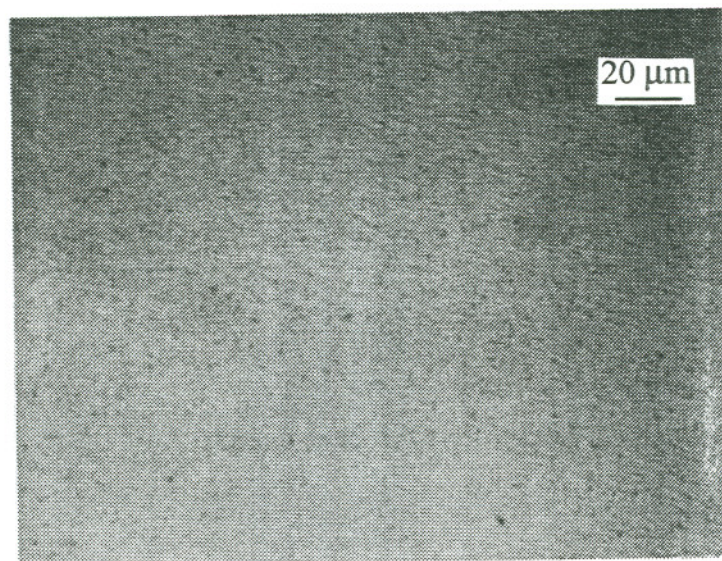
The growth rates of HgTe epilayers grown on (100)  $5^{\circ} \rightarrow (110)$  CdTe substrate ranged from 0.75  $\mu\text{m}/\text{h}$  to 2.7  $\mu\text{m}/\text{h}$ , as plotted in Figure 5.9. The growth rate of HgTe epilayers decreased at  $T_s$  greater than or less than 300  $^{\circ}\text{C}$ . The growth rate as a function of  $T_s$  suggests that below 300  $^{\circ}\text{C}$ , the MATE cracking rate decreases more rapidly than does the Hg volatility; and that above 300  $^{\circ}\text{C}$ , the MATE cracking rate increases less rapidly than does the Hg volatility.

When the flow rate of MATE alkyl was doubled from  $Q_{\text{Te}}=1.55$  sccm to  $Q_{\text{Te}}=3.1$  sccm at  $T_s=300$   $^{\circ}\text{C}$ , the growth rate of HgTe did not change. This result suggested that more Hg was needed to increase the growth rate of HgTe. The growth conditions which gave the highest growth rate of HgTe,  $Q_{\text{Hg}}=226.0$  sccm and  $Q_{\text{Te}}=1.5$  sccm was used for the first  $\text{Hg}_{1-x}\text{Cd}_x\text{Te}$  epilayer growth experiments.

The distance above the plane of the ARI inlet, at which the substrate surface was located, significantly affected to the growth rate of HgTe (about 0.3  $\mu\text{m}/\text{h}$  increment) at above conditions. The separation distance which gave the highest growth rate of HgTe, 6.3 mm, was used to for all HgTe and  $\text{Hg}_{1-x}\text{Cd}_x\text{Te}$  growth experiments.



(a)



(b)

**Figure 5.8** Nomarski contrast micrograph of CdTe epilayers showing microterraces (a) and pits (b).

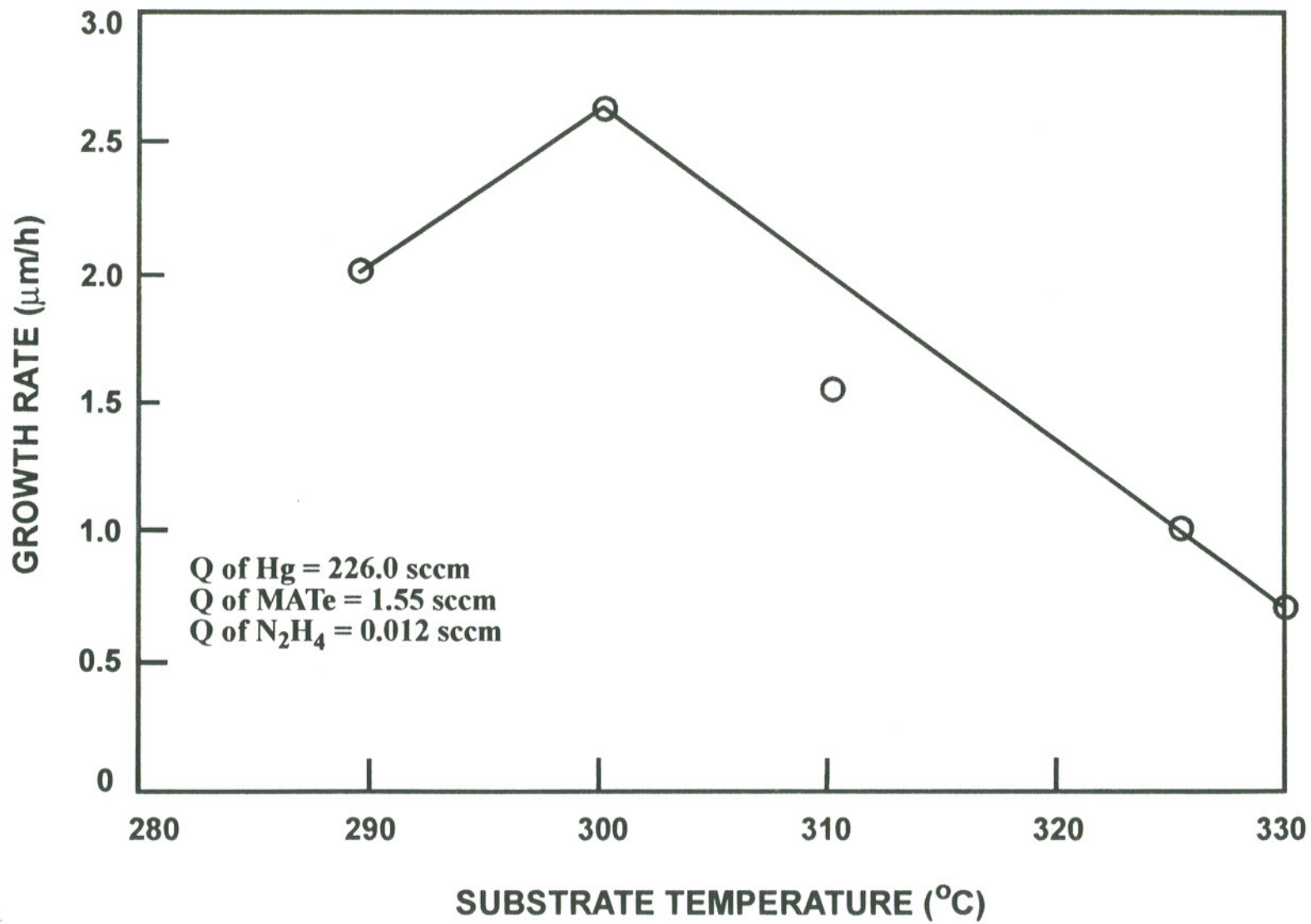


Figure 5.9 Growth rate of HgTe epilayer as a function of substrate temperature.

The as-grown HgTe epilayers grown at  $290\text{ }^{\circ}\text{C} \leq T_s \leq 330\text{ }^{\circ}\text{C}$  were single crystalline. The ECCP showed one-fold bright bands about 1 mm wide, which were single crystalline and indicate a (100) orientation of the grown layer, but as before in the case of CdTe layers the bright bands were not clear enough to be used for comparing crystalline quality of the HgTe layers.

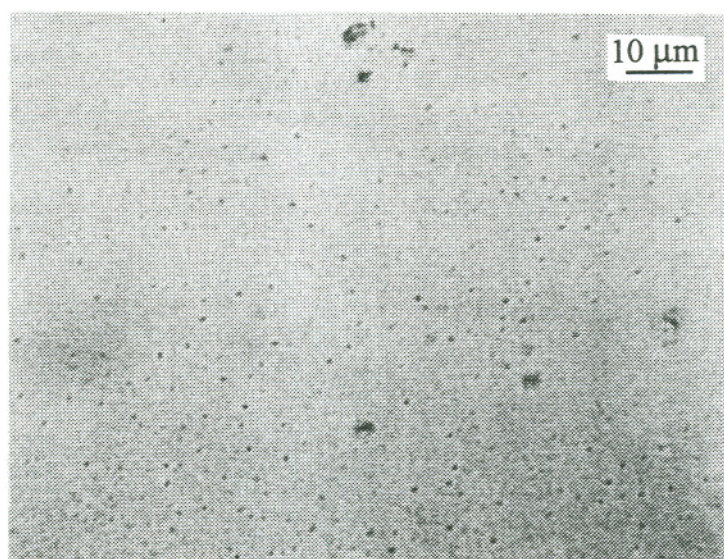
In morphology studies, most HgTe layers grown on CdTe substrates showed smooth and specular surface. Pitted HgTe layers grown at  $T_s=330\text{ }^{\circ}\text{C}$ , shown in Figure 5.10, were observed when the MATE flow rate of 3.1 sccm was used. When the MATE flow rate of 1.55 sccm was introduced at  $T_s=330\text{ }^{\circ}\text{C}$ , the as-grown HgTe surface showed hillocks with the hillock density in the range of 3000 - 5000  $\text{cm}^{-2}$ , as shown in Figure 5.11. However, the HgTe epilayer surfaces grown below  $320\text{ }^{\circ}\text{C}$  did not show pits or hillocks. These results suggest that the lower temperature growth of HgTe gives the better surface morphology and the pits and the hillocks surface are probably related to the Te-rich and Hg-rich surfaces, respectively.

### 5.3 $\text{Hg}_{1-x}\text{Cd}_x\text{Te}$ Epilayer Growth

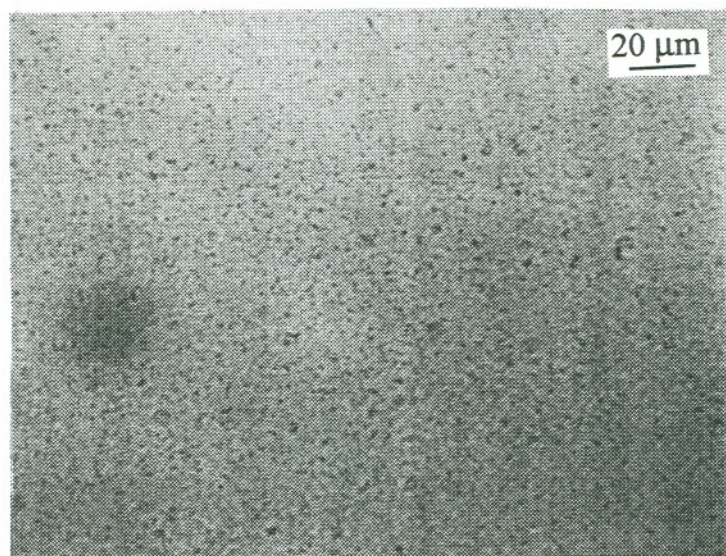
#### 5.3.1 Growth Rate of $\text{Hg}_{1-x}\text{Cd}_x\text{Te}$ Layers

A typical FTIR transmission curve and a representative Nomarski contrast micrograph of a cleaved cross section showing the  $\text{Hg}_{1-x}\text{Cd}_x\text{Te}$  layer, which were used to determine the growth rate and the composition of  $\text{Hg}_{1-x}\text{Cd}_x\text{Te}$  epilayers, are presented in Figure 5.12 and 5.13, respectively. The micrographs show the interface, sufficiently clearly to measure the thickness of the  $\text{Hg}_{1-x}\text{Cd}_x\text{Te}$  epilayer without SEM, when the defect etchant was used [75].

The growth rate and the composition of  $\text{Hg}_{1-x}\text{Cd}_x\text{Te}$  epilayers at  $T_s=300\text{ }^{\circ}\text{C}$  was a function of DMCD flow rate, as shown in Figure 5.14. The  $\text{Hg}_{1-x}\text{Cd}_x\text{Te}$

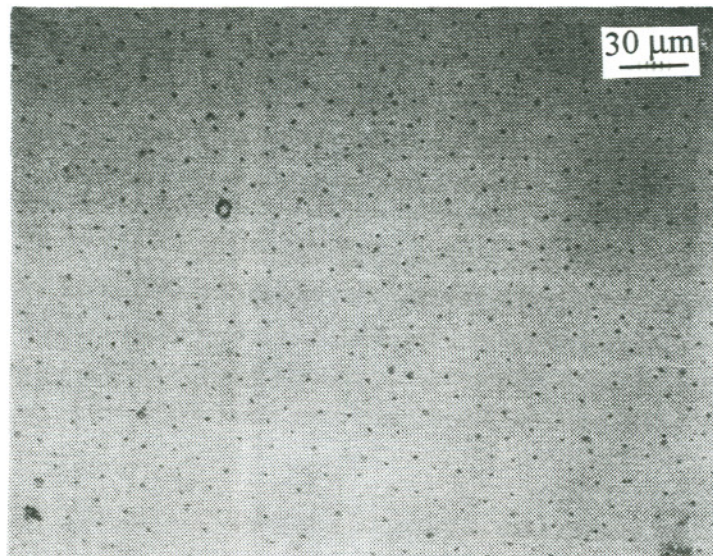


(a)

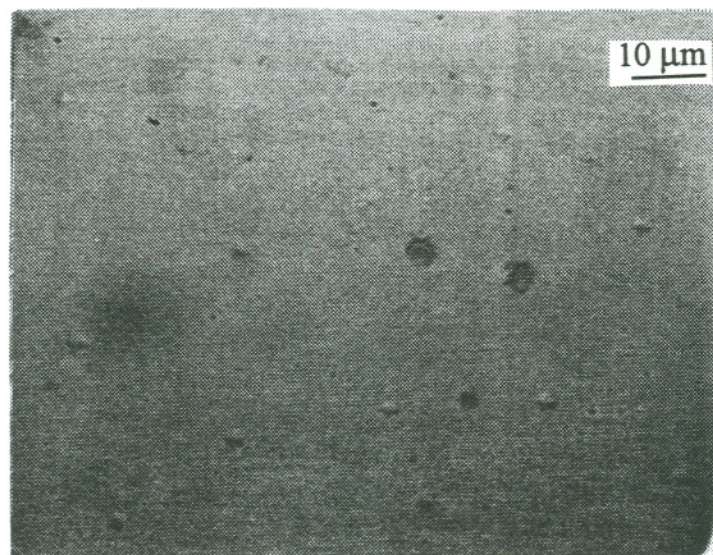


(b)

**Figure 5.10** Nomarski contrast micrograph of HgTe epilayer showing pits (a) 910x and (b) 448 x.



(a)



(b)

**Figure 5.11** Nomarski contrast micrograph of HgTe epilayer showing hillocks; (a) 177 x and (b) 910 x.

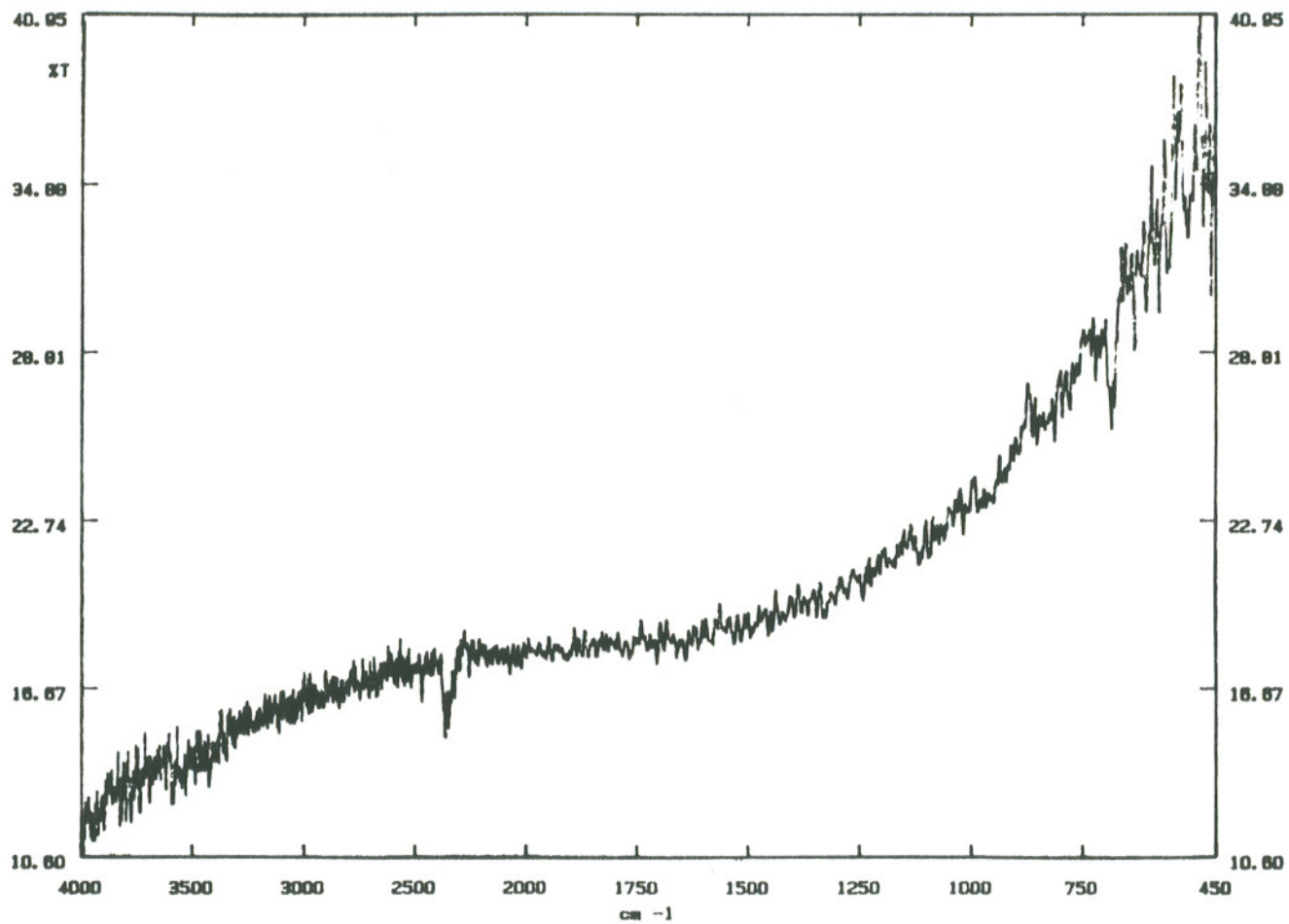
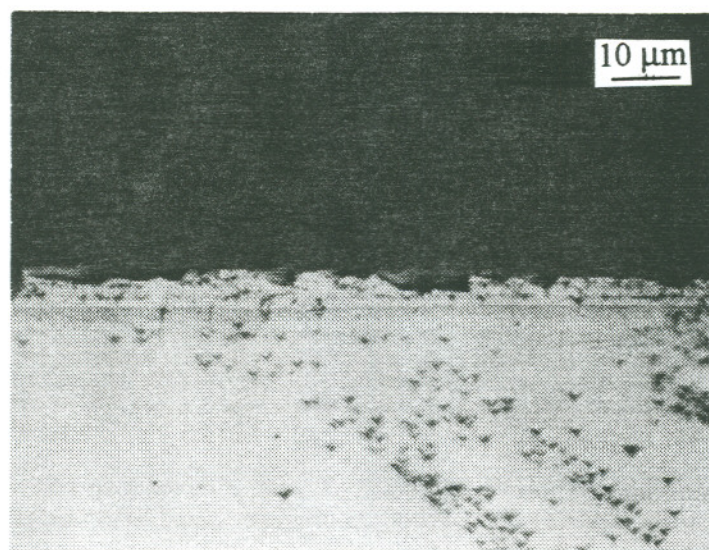
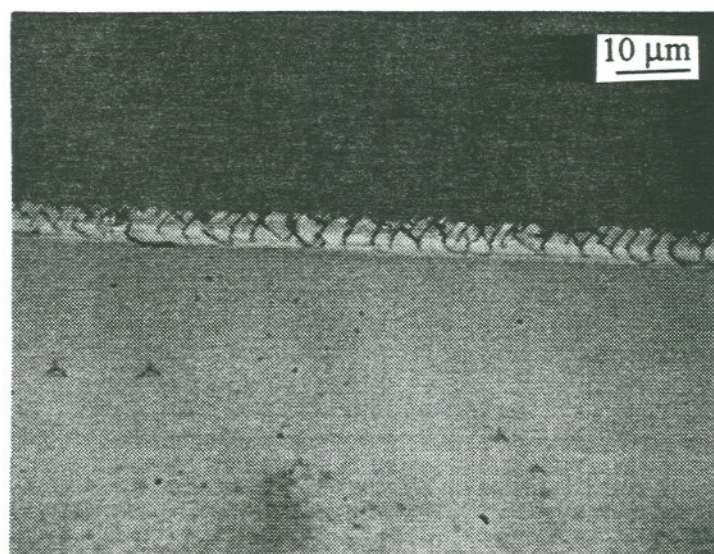


Figure 5.12 Typical Fourier Transform of Infrared transmission curve of  $\text{Hg}_{1-x}\text{Cd}_x\text{Te}$  epilayer grown on CdTe substrate.



(a)



(b)

**Figure 5.13** Nomarski contrast micrograph of cleaved cross-sections on two different composition samples after etching with Hähnert etchant.

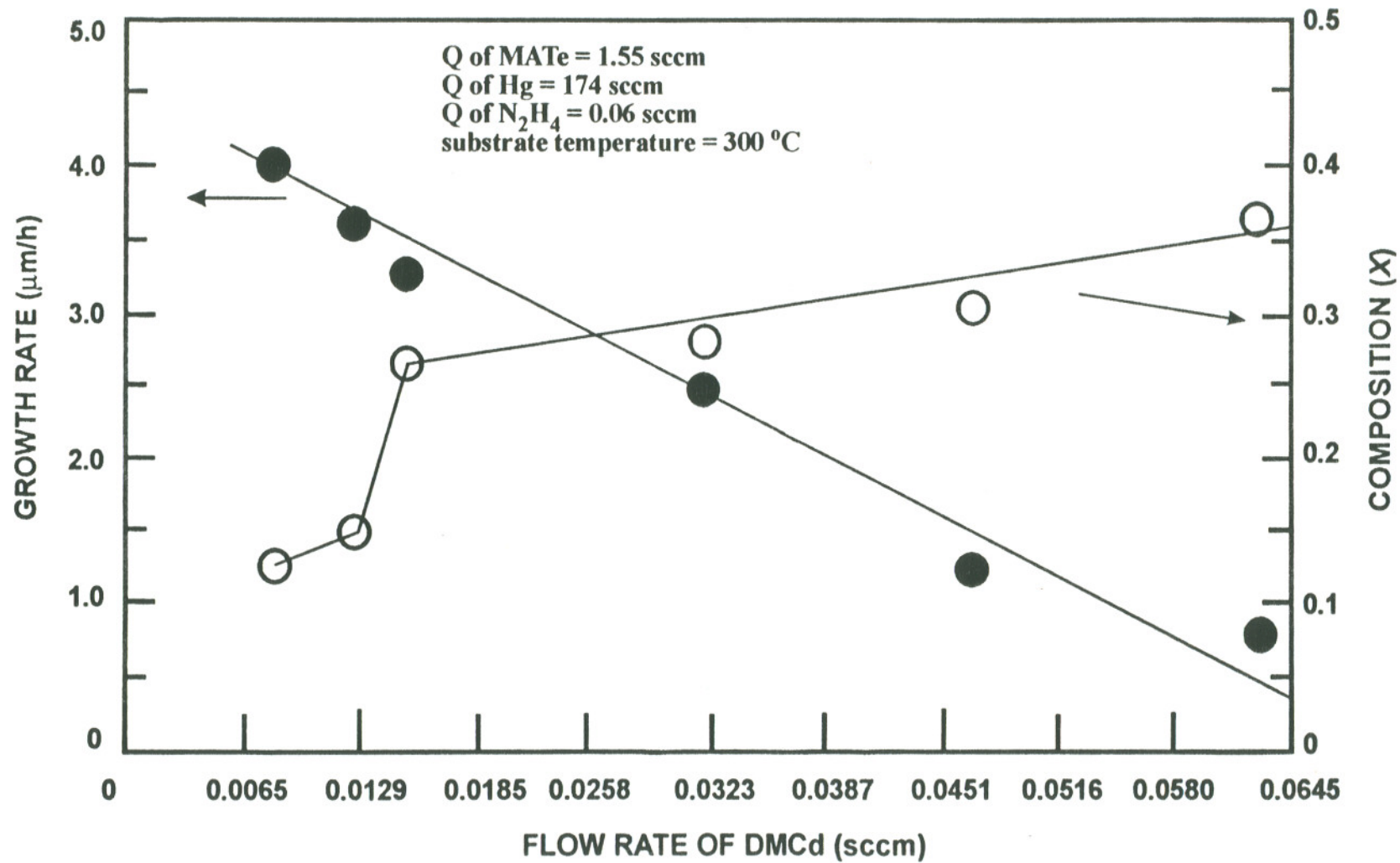


Figure 5.14 Growth rate and composition of Hg<sub>1-x</sub>Cd<sub>x</sub>Te as a function of the flow rate of DMCD.

epilayer growth rate decreased from 4  $\mu\text{m/h}$  at the DMCd flow rate of 0.0075 sccm to 0.75  $\mu\text{m/h}$  at the DMCd flow rate of 0.06 sccm. The composition of  $\text{Hg}_{1-x}\text{Cd}_x\text{Te}$  epilayers increased from  $x=0.126$  to  $x=0.359$  as the flow rate of DMCd increased from 0.0075 sccm to 0.06 sccm. The increase of  $\text{Hg}_{1-x}\text{Cd}_x\text{Te}$  composition, coupled with a decreasing the growth rate of  $\text{Hg}_{1-x}\text{Cd}_x\text{Te}$  at higher flow rate of DMCd, indicates that Cd is interfering with Hg nucleation because of the disparity in bond strength between CdTe and HgTe [13].

The presence of the relatively strongly bonding Cd ( $\cong 23$  kcal/mol) in  $\text{Hg}_{1-x}\text{Cd}_x\text{Te}$  on a growth surface would increase the probability of nucleation of Cd, whereas the more weakly bonding Hg ( $\cong 13$  kcal/mol) would be less likely to nucleate on the growth surface. In the absence of Cd, once a nucleating site is formed, further nucleation of Hg in the vicinity of this site is unlikely due to the weak bond strength between Hg and Te. This weak bonding of Hg would enable any adsorbed Hg atoms to diffuse readily across the crystal surface until they reached a growth step, or even to desorb. The presence of strongly bonding Cd will result in the preferential formation of Cd nucleating sites and result in a higher composition alloy and a lower growth rate in the  $\text{Hg}_{1-x}\text{Cd}_x\text{Te}$  crystal. Therefore, even a small flux of DMCd determines the composition of  $\text{Hg}_{1-x}\text{Cd}_x\text{Te}$  epilayer crystal.

Another  $\text{Hg}_{1-x}\text{Cd}_x\text{Te}$  growth experiments at  $T_s=330$  °C was performed as a function of MATe flow rate at fixed the DMCd flow rate of 0.045 sccm, in order to check the contribution of DMCd alkyls to the growth rate and the composition of as-grown  $\text{Hg}_{1-x}\text{Cd}_x\text{Te}$  epilayer. This result is plotted in Figure 5.15.

The  $\text{Hg}_{1-x}\text{Cd}_x\text{Te}$  growth rate at  $T_s=330$  °C ranged between 0.25 - 0.7  $\mu\text{m/h}$  as the MATe flow rates increased from 0.776 sccm to 3.102 sccm. The growth rate was doubled when the flow rate of MATe was doubled from 0.776 sccm to 1.55 sccm, but the growth rate was not doubled when the flow rate of MATe was

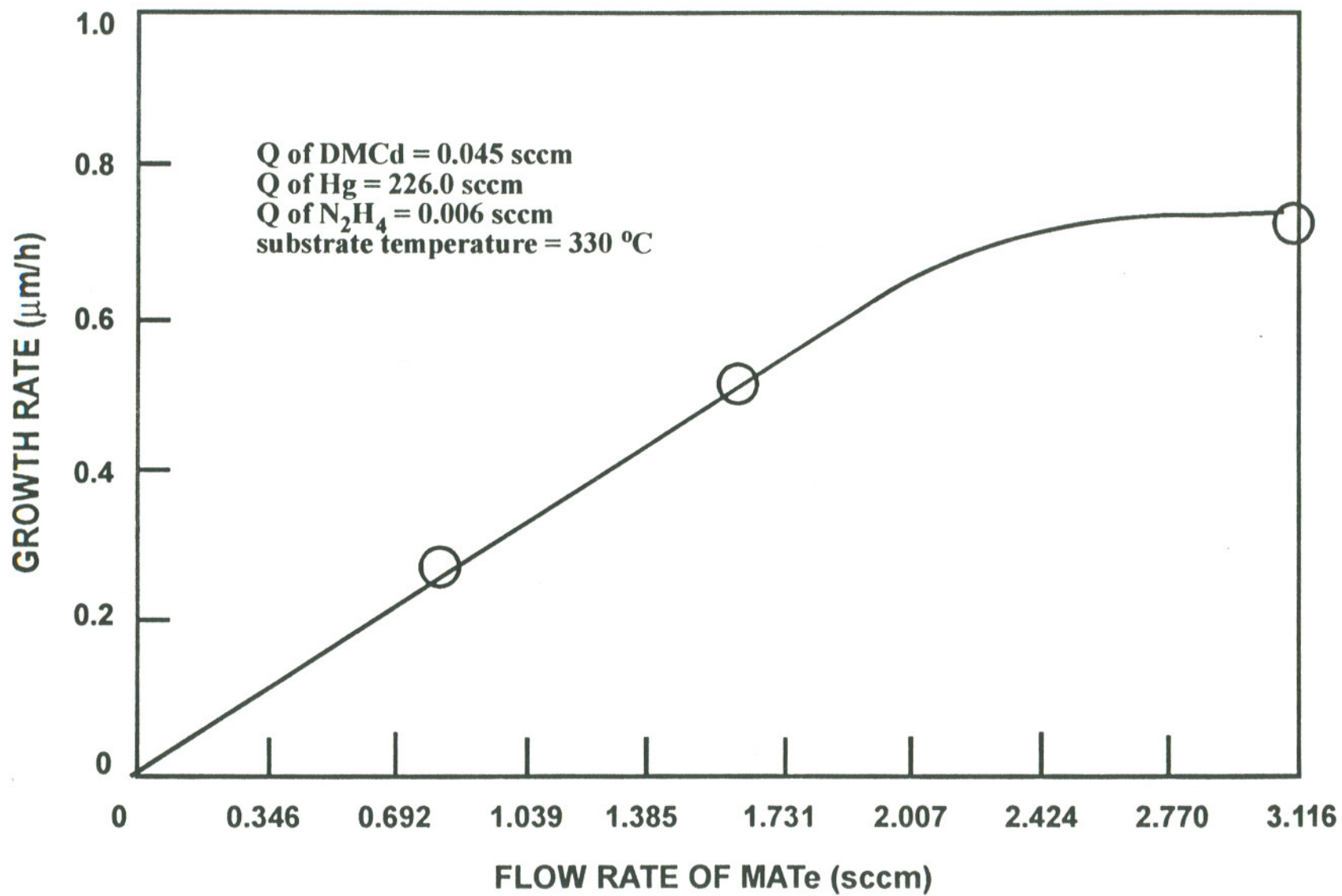


Figure 5.15 Growth rate of Hg<sub>1-x</sub>Cd<sub>x</sub>Te as a function of the flow rate of MAtE.

doubled again from 1.55 sccm to 3.102 sccm. This may be due to the insufficient Hg available for higher  $\text{Hg}_{1-x}\text{Cd}_x\text{Te}$  growth rates. The composition of these  $\text{Hg}_{1-x}\text{Cd}_x\text{Te}$  epitaxial layers was  $x = 0.356 \pm 0.01$  for three different films within the measured MATE flow rate range (a little lower for the lower MATE flux and little higher for the higher MATE flux).

### 5.3.2 Thickness and Composition Uniformity

Thickness and compositional uniformity maps of thin  $\text{Hg}_{1-x}\text{Cd}_x\text{Te}$  epilayers on 20 cm<sup>2</sup> CdTe substrates, which were determined by MAI ellipsometric technique, are shown in Figure 5.16, for the system configurations of both single Hg inlet to the annular jacket and double opposing Hg inlets to the annular jackets. As can be seen in (a) of Figure 5.16, the compositional uniformity is excellent but the thickness uniformity reveals a gradient from 1101 Å to 1009 Å ( $\cong$  10 % variation) when the single Hg inlet port configuration was employed. The composition of the thin  $\text{Hg}_{1-x}\text{Cd}_x\text{Te}$  epitaxial layer obtained from the real part of refractive index from MAI ellipsometry data was  $x=0.92$ , which is not shown in Fig 5.14.

The highest growth rate of  $\text{Hg}_{1-x}\text{Cd}_x\text{Te}$  epilayer was obtained on the side of the layer which was nearest the annular jacket inlet port and the lowest growth rate of  $\text{Hg}_{1-x}\text{Cd}_x\text{Te}$  epilayer was obtained on the side of the layer farthest from the annular jacket inlet port. This result suggested that the Hg vapor was entering the reactor primarily from the side of the ARI opposite the annular jacket inlet port. The second inlet port, therefore, was added to the annular jacket.

When the single Hg inlet port to ARIIV was modified to the double Hg inlet configuration, the thickness uniformity improved to 4 % variation, from 1008 Å to 970 Å over the 20 cm<sup>2</sup> substrate, but the compositional uniformity deteriorated somewhat to  $x=0.602 \pm 0.002$ , as shown in (b) of Figure 5.16. From a comparison

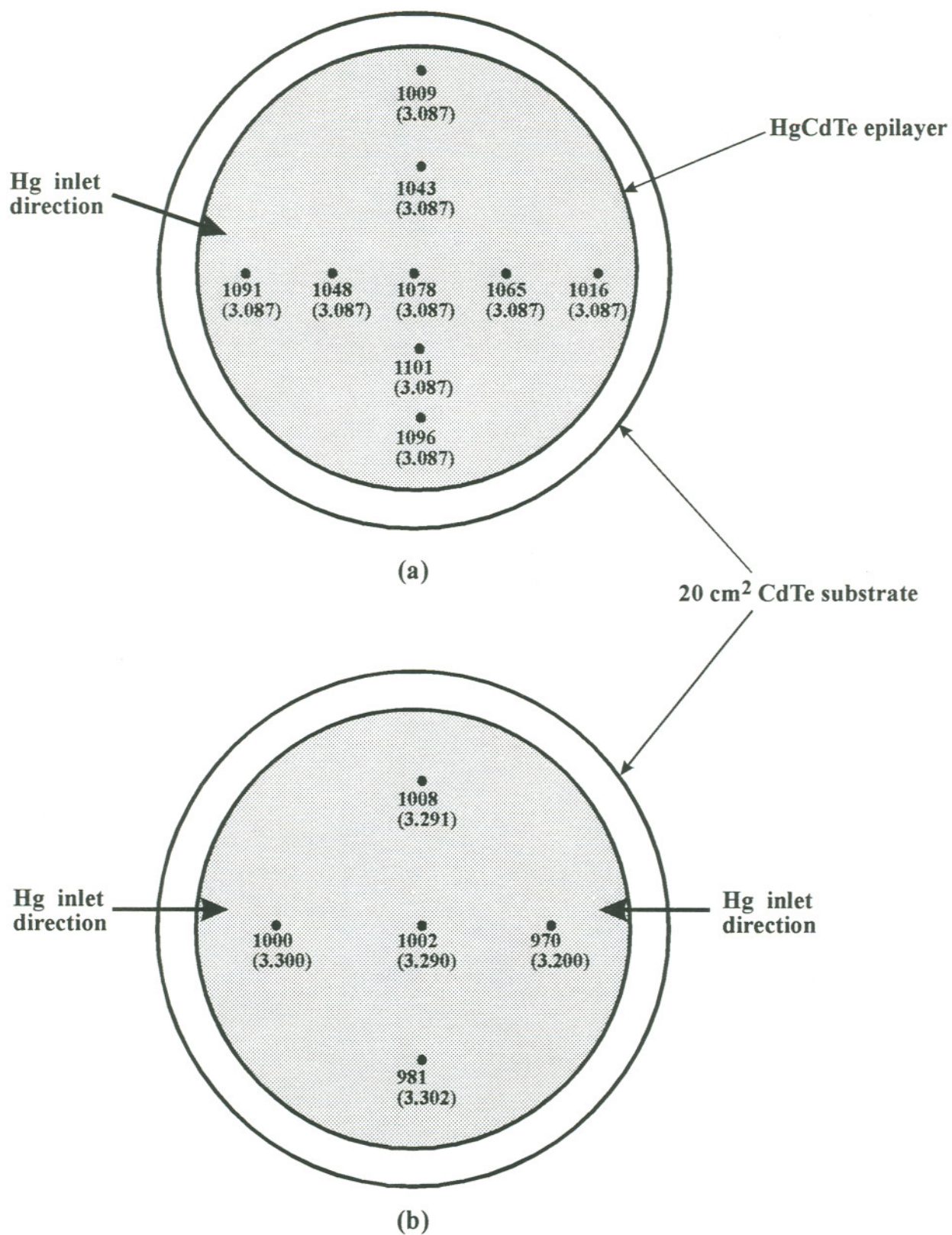


**Figure 5.16** Thickness ( $\text{\AA}$ ) and compositional uniformity (refractive index) maps of thin  $\text{Hg}_{1-x}\text{Cd}_x\text{Te}$  epilayer when (a) single Hg inlet and (b) dual Hg inlets were used. The refractive index of  $\text{Hg}_{1-x}\text{Cd}_x\text{Te}$  in parenthesis.

of the single and double inlet configurations, even though two different growth recipes were used, it can be seen that the double Hg inlet ARIIV reactor improved the thickness uniformity but showed some variation in the compositional uniformity. However, it should be noted that the compositional uniformity was generally improved as the  $x$ -value increased, but it was difficult to find evidence that the thickness uniformity depended on the Cd concentrations as the growth of  $\text{Hg}_{1-x}\text{Cd}_x\text{Te}$  epitaxial layers proceeded.

In order to determine if the excellent compositional uniformity of initial stage growth was maintained as growth proceeded, the compositional uniformity for a 4  $\mu\text{m}$  thick  $\text{Hg}_{1-x}\text{Cd}_x\text{Te}$  epilayer ( $x=0.152$ ) grown on a 6.45  $\text{cm}^2$  CdTe substrate was measured by FTIR, as described in Section 3.4. The compositional profile for this  $\text{Hg}_{0.848}\text{Cd}_{0.152}\text{Te}$  epitaxial single crystal showed excellent uniformity within the error  $x = 0.152 \pm 0.002$ , as presented in Figure 5.17.

This uniformity results using the ARIIV reactor are equal to or better than MBE uniformity [79] for substrate sizes of 2-4 cm and exceeds the uniformity achieved by the IMP growth technique [79], which has previously been considered to be superior in compositional uniformity to the DAG process. To our knowledge, this is the first time that state-of-the-art thickness and compositional uniformities have been obtained by DAG technique for  $\text{Hg}_{1-x}\text{Cd}_x\text{Te}$  epitaxial layer by OMVPE.

### 5.3.3 Surface Morphology

The morphology of  $\text{Hg}_{1-x}\text{Cd}_x\text{Te}$  epilayers ( $0.1 \leq x \leq 0.4$ ) grown at  $T_s=300$  °C and 330 °C consisted of specular surfaces with a notable absence of ridges, which are usually observed when DIPTe or DETe is used as the Te reactant organometallic source [64, 76].

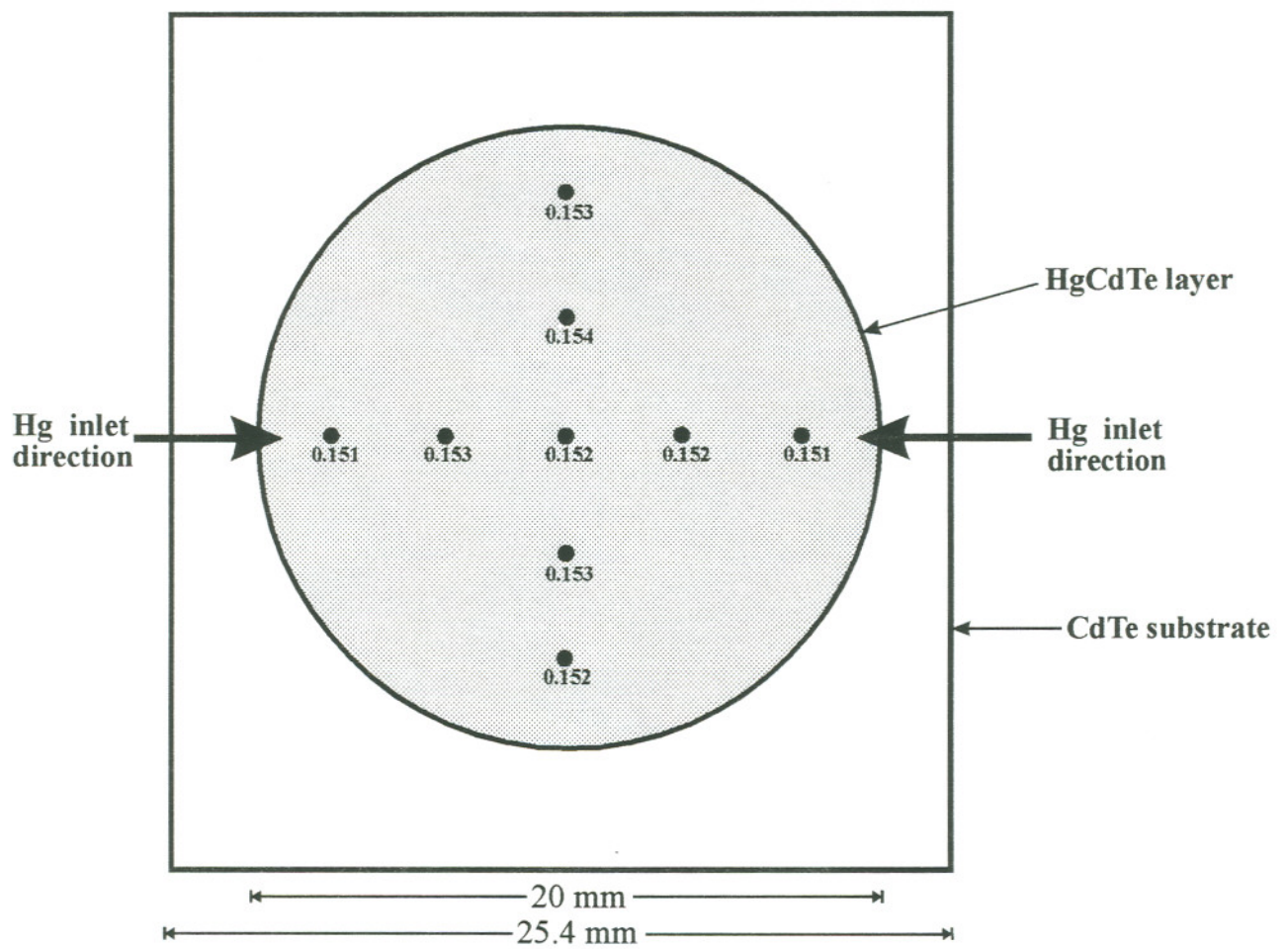


**Figure 5.17** Compositional ( $x$ ) uniformity of  $4\ \mu\text{m}$  thick  $\text{Hg}_{1-x}\text{Cd}_x\text{Te}$  epitaxial layer over  $6.45\ \text{cm}^2$  CdTe substrate.

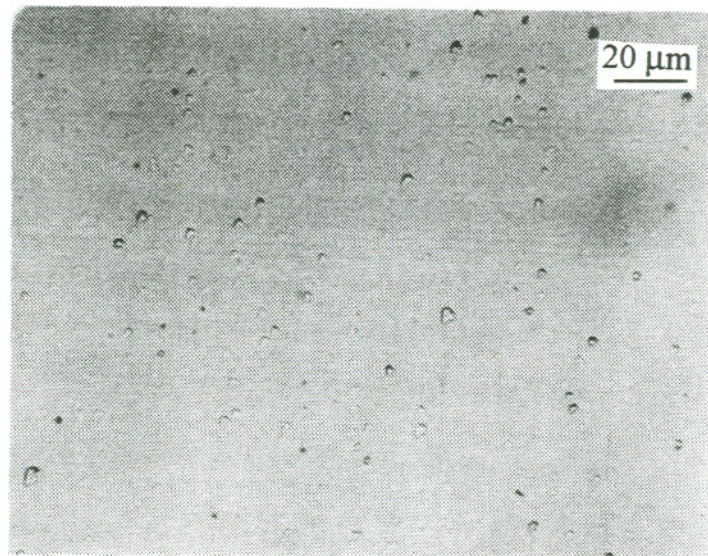
The surface of  $\text{Hg}_{1-x}\text{Cd}_x\text{Te}$  ( $x \geq 0.6$ ) epitaxial layers grown at 330 °C contained hillocks, hillock densities in the range of 200 to 400  $\text{cm}^{-2}$ , as shown in Figure 5.18 (a). This value is an order of magnitude lower than that obtained in  $\text{HgTe}$  epitaxial layers grown at 330 °C (normally 3000-5000  $\text{cm}^{-2}$ ). At  $T_s=300$  °C the surface of  $\text{Hg}_{1-x}\text{Cd}_x\text{Te}$  layers did not contain hillocks. This confirms that the improvement of morphology in  $\text{Hg}_{1-x}\text{Cd}_x\text{Te}$  epilayers grown is primarily due to the lower growth temperature.

When the flow rates of hydrogen through MATe and DMCD bubblers were doubled and the growth temperature was kept 330 °C, the hillock density was increased to 2000  $\text{cm}^{-2}$ , as shown in Figure 5.18 (b). The increment of hillock density at higher flow rates of both MATe and DMCD is considered to be due to Cd-rich characteristics in OMVPE [79], because a doubling of MATe and DMCD increases the Cd concentration of the  $\text{Hg}_{1-x}\text{Cd}_x\text{Te}$  layer due to the higher Cd partial pressure.

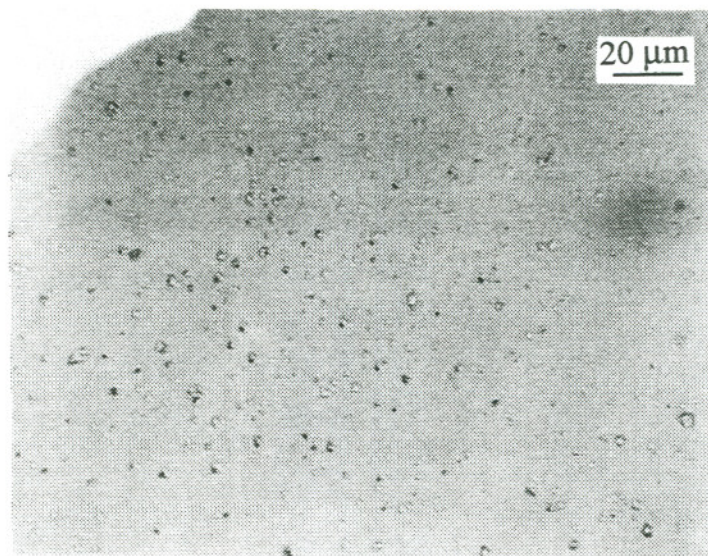
Specular surface was obtained in  $\text{Hg}_{1-x}\text{Cd}_x\text{Te}$  ( $x \leq 0.4$ ) at 300 °C. Micro terraces, hillocks, or pits were not observed in any  $\text{Hg}_{1-x}\text{Cd}_x\text{Te}$  ( $0.152 \leq x \leq 0.356$ ) layers, Figure 5.19 (a).

Some elemental Hg splatters on the  $\text{Hg}_{1-x}\text{Cd}_x\text{Te}$  grown layers were observed when the growth time was more than 3 hrs, as shown in Figure 5.19 (b). This was due to the condensed Hg in the primary inlet port, and the ARI port. This configuration problem of the ARIIV reactor tube can be eliminated by changing the primary inlet and the ARI port configuration, as shown in Figure 5.20.

The single crystallinity of  $\text{Hg}_{1-x}\text{Cd}_x\text{Te}$  epilayers grown on CdTe substrates was confirmed by ECCP. One-fold bright bands about 1 mm wide were observed on the ECCP picture, confirming that the layer was monocrystalline, but the bright bands were not clear enough to be used for calculating composition of  $\text{Hg}_{1-x}\text{Cd}_x\text{Te}$  crystal. An ECCP photo of a  $\text{Hg}_{1-x}\text{Cd}_x\text{Te}$  epilayer is shown in Figure 5.21.

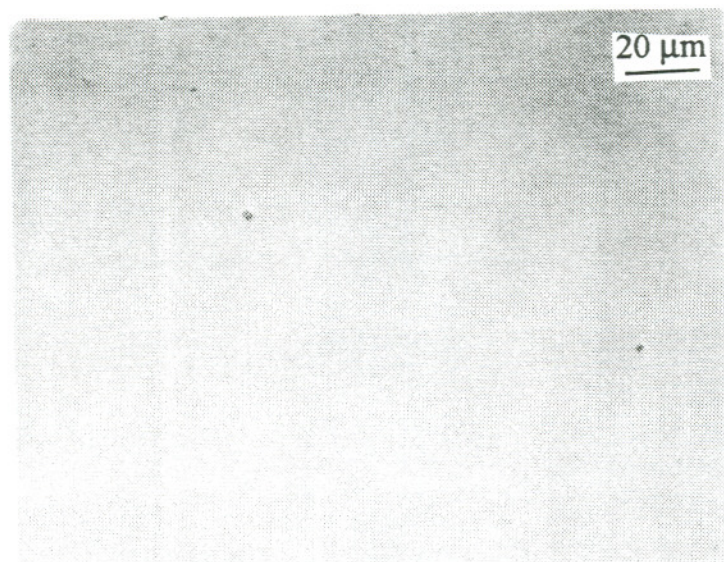


(a)

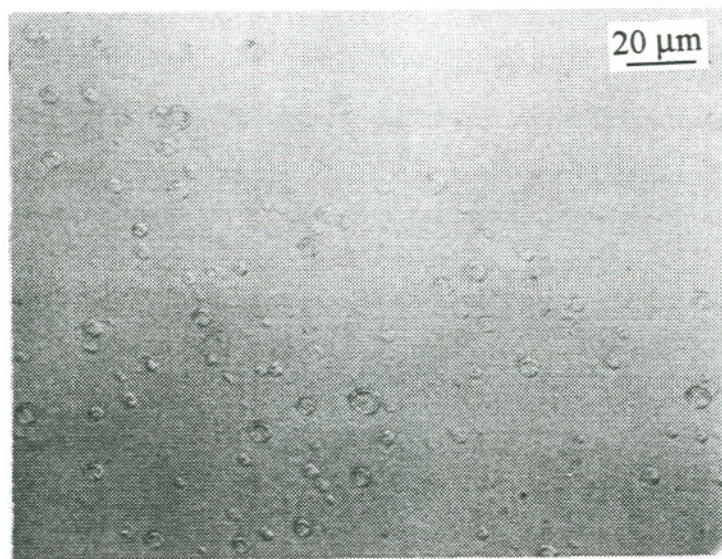


(b)

**Figure 5.18** Nomarski contrast micrograph of  $\text{Hg}_{1-x}\text{Cd}_x\text{Te}$  epilayer showing hillocks; (a)  $Q_{\text{Te}}=1.55$  sccm and (b)  $Q_{\text{Te}}=3.1$  sccm at  $T_s=330$  °C.



(a)



(b)

**Figure 5.19** Nomarski contrast micrograph of  $\text{Hg}_{1-x}\text{Cd}_x\text{Te}$  epitaxial layers showing (a) as-grown  $\text{Hg}_{1-x}\text{Cd}_x\text{Te}$  and (b) Hg-splattered  $\text{Hg}_{1-x}\text{Cd}_x\text{Te}$  surface.

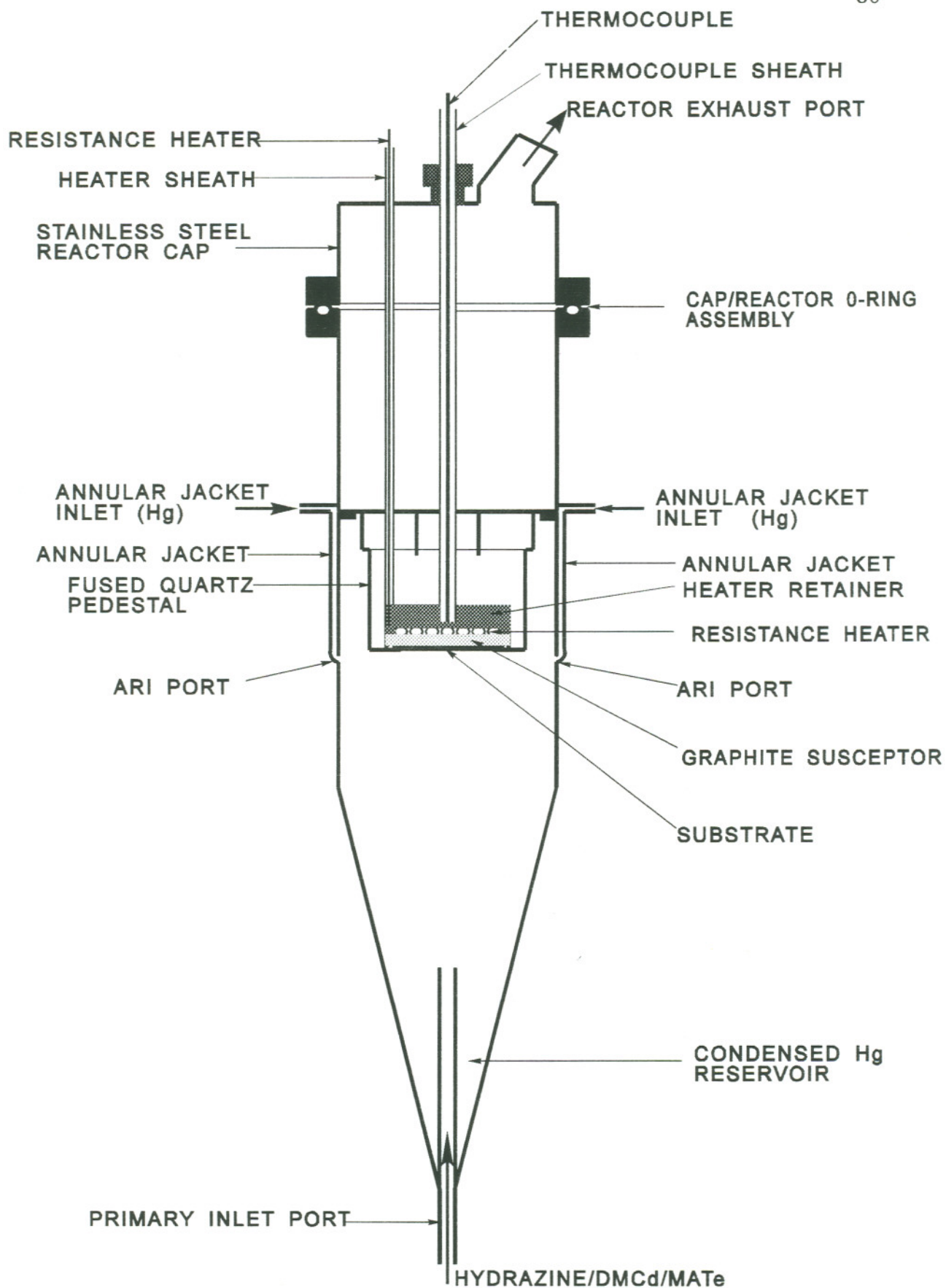
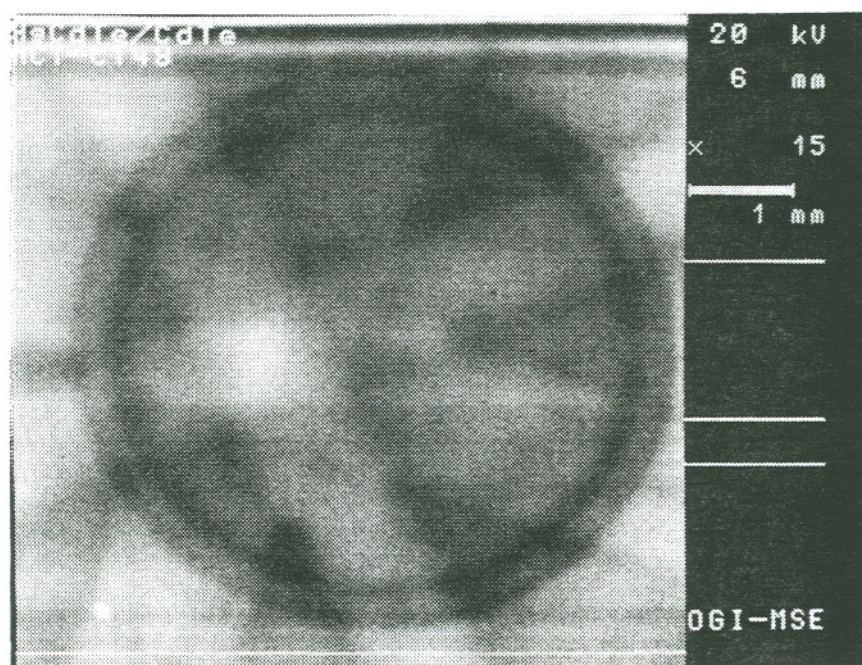


Figure 5.20 Cross-sectional drawing of the modified ARIIV reactor tube assembly.



**Figure 5.21** Electron channeling contrast pattern of  $\text{Hg}_{1-x}\text{Cd}_x\text{Te}$  epitaxial layer grown on  $\text{CdTe}$  substrate.

### 5.3.4 Defect Etching

A chemical etching technique was used to determine the distribution of crystallographic defects (dislocations, subgrain boundaries, or inclusions) in  $\text{Hg}_{1-x}\text{Cd}_x\text{Te}$  [75]. Shown in Figure 5.22 (a) and (b), are representative etch patterns of epitaxial layers of  $\text{Hg}_{1-x}\text{Cd}_x\text{Te}$  on (100)  $5^\circ \rightarrow (110)$  CdTe substrates.

The morphology and the size of the pits with square shape are clearly observed. The etch pits are so small ( $\sim 5\mu\text{m}$ ) and have such uniform tops, that it is possible to observe etch pit densities up to  $10^4 - 10^5 \text{ cm}^{-2}$ . The etch pit distribution was investigated after successive etching procedures, to determine whether the origin of subgrains in  $\text{Hg}_{1-x}\text{Cd}_x\text{Te}$  epilayers was due to grown-in dislocations or subgrain boundaries in the CdTe substrate. Subgrain boundaries of the CdTe substrate after several successive etchings are shown in Figure 5.22 (c). The result of the final etching confirmed that the origin of the subgrains in  $\text{Hg}_{1-x}\text{Cd}_x\text{Te}$  epilayers was due to subgrains in CdTe substrates. These subgrains result in lower mobilities and higher carrier concentrations (as discussed in the next section).

### 5.3.5 Electrical Properties of $\text{Hg}_{1-x}\text{Cd}_x\text{Te}$ Epilayers

For *n*-type  $\text{Hg}_{1-x}\text{Cd}_x\text{Te}$  samples, measurements at a few temperatures between 50 - 300 K can provide enough data for sample evaluation. *P*-type samples, on the other hand, require a detailed plot over this temperature range. Anomalous results often arise in higher *x* layers ( $x \geq 0.25$ ) which are subject to surface inversion.

The effects of temperature on the Hall coefficient  $R_H$  for a representative as-grown *n*-type  $\text{Hg}_{1-x}\text{Cd}_x\text{Te}$  sample ( $x=0.126$ ) is plotted in Figure 5.23. This coefficient is negative at low temperatures, because an excess of donors dominates extrinsic conduction; and remains negative in the intrinsic range at higher temperatures, because the electron mobility is greater than the hole mobility.

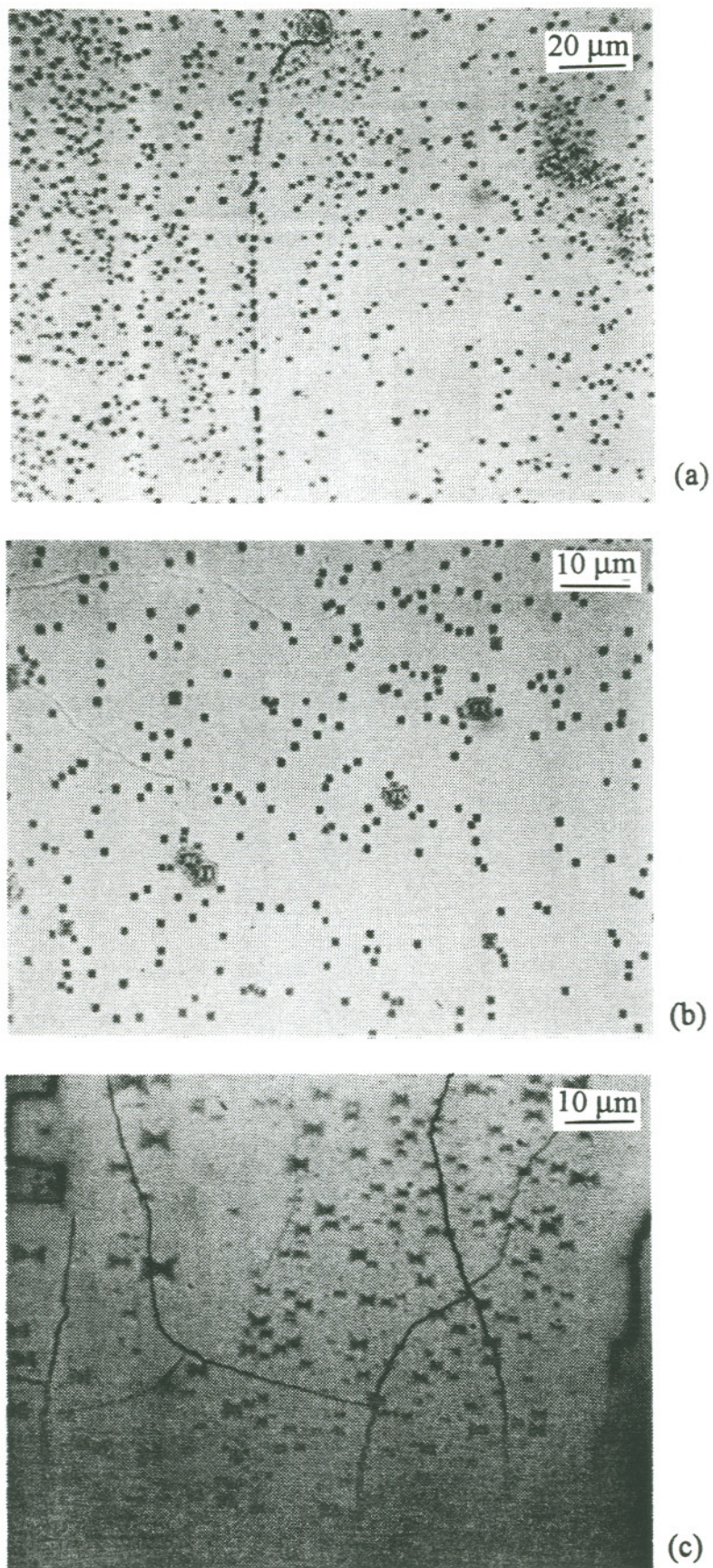


**Figure 5.22** Normarski contrast micrograph showing subgrain boundaries  $\text{Hg}_{1-x}\text{Cd}_x\text{Te}$  (a,b) and subgrain boundaries CdTe substrate (c).

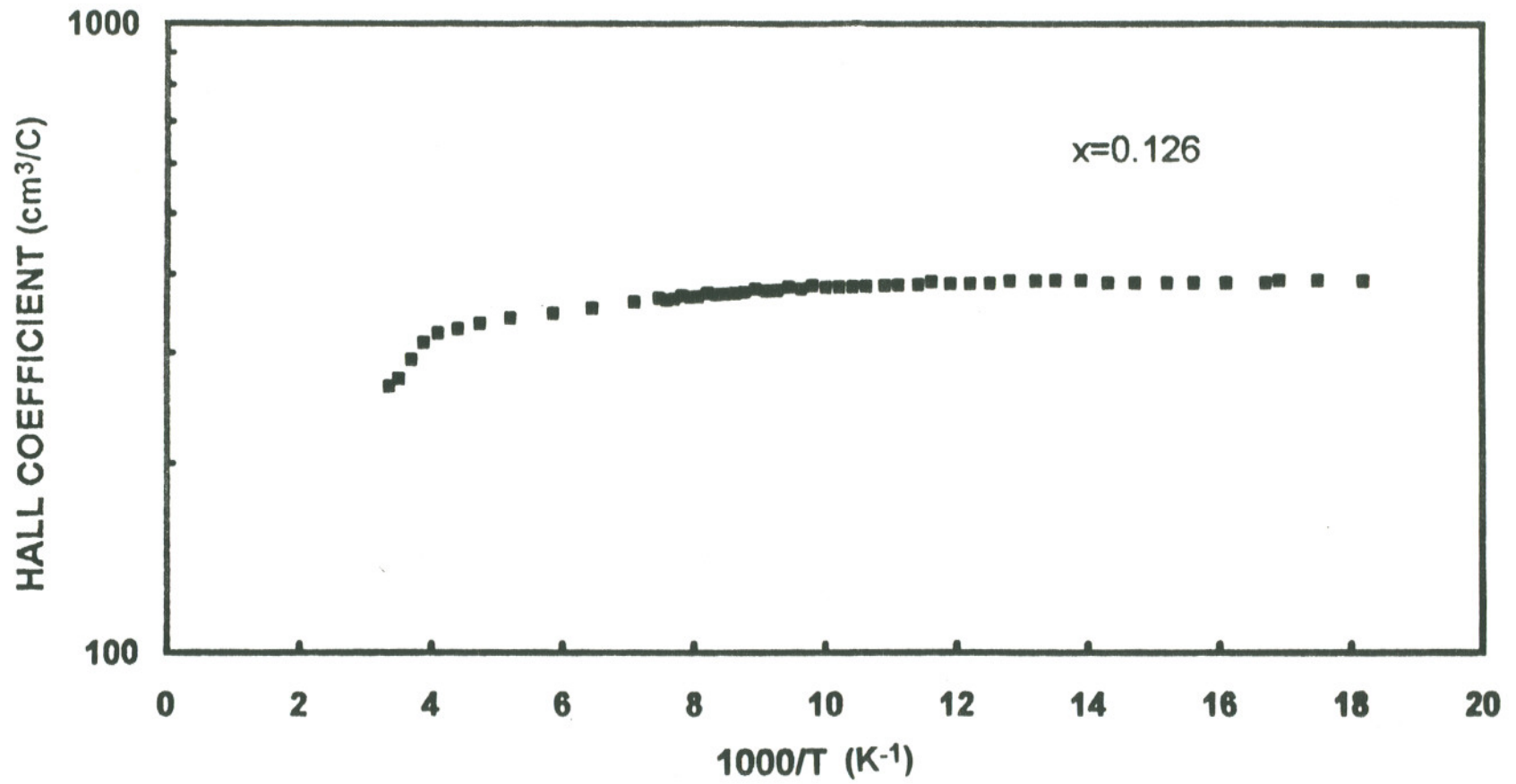


Figure 5.23 The Hall coefficient  $R_H$  as a function of reciprocal temperature for  $n$ -type  $\text{Hg}_{1-x}\text{Cd}_x\text{Te}$  ( $x=0.126$ ) sample.

The variation of Hall mobility as a function of temperature for this  $\text{Hg}_{1-x}\text{Cd}_x\text{Te}$  ( $x=0.126$ ) sample is shown in Figure 5.24. The rapid decrease of the electron mobility at temperatures above approximately 180 K is due to the dominance of lattice scattering mechanisms above this temperature. The slight fall in electron mobility at low temperature ( $\leq 70$  K) can best be explained by taking ionized impurity scattering effects into account [20]. The effects of these two scattering mechanisms result in a maximum in the mobility characteristic at around 80 K. The mobility of this sample fell by only about 6% when the applied magnetic field was increased from 0.5 to 3 kG, thus confirming that the material is truly extrinsic. The basic carrier concentrations  $|N_a - N_d|$  were in the range  $(1.8 - 3.0) \times 10^{16} \text{ cm}^{-3}$ , as shown in Figure 5.24.

The reason that as-grown *n*-type  $\text{Hg}_{1-x}\text{Cd}_x\text{Te}$  layers with  $x=0.126$  displayed a relatively constant carrier concentration and rather poor mobilities was determined to be subgrain boundaries in the CdTe substrates, as evidenced in Figure 5.22 (c) and from the 2 peaks in the DCXRC, Figure 5.6 (b).

The *p*-type  $\text{Hg}_{1-x}\text{Cd}_x\text{Te}$  layers were obtained when the composition of as-grown materials was over  $x=0.25$ . The Hall coefficient and the hole mobility and carrier concentrations versus reciprocal temperature for a *p*-type  $\text{Hg}_{1-x}\text{Cd}_x\text{Te}$  layer ( $x=0.266$ ) is presented in Figures 5.25 and 5.26, respectively. The Hall coefficient is negative at higher temperatures because the material become intrinsic and the electron mobility is higher than the hole mobility. The change-over from negative to positive Hall coefficient takes place at about 130 K. The hole mobility is about  $110 \text{ cm}^2/\text{V} \cdot \text{s}$  with  $|N_a - N_d| = 3 \times 10^{16} \text{ cm}^{-3}$ . No clear extrinsic region in the Hall coefficient is seen, probably because the extrinsic region and the region at which  $R_H$  reverses sign overlap. The mechanism which accounts for the anomalous behavior of *p*-type  $\text{Hg}_{1-x}\text{Cd}_x\text{Te}$  materials was explained in detail in Chapter 2.

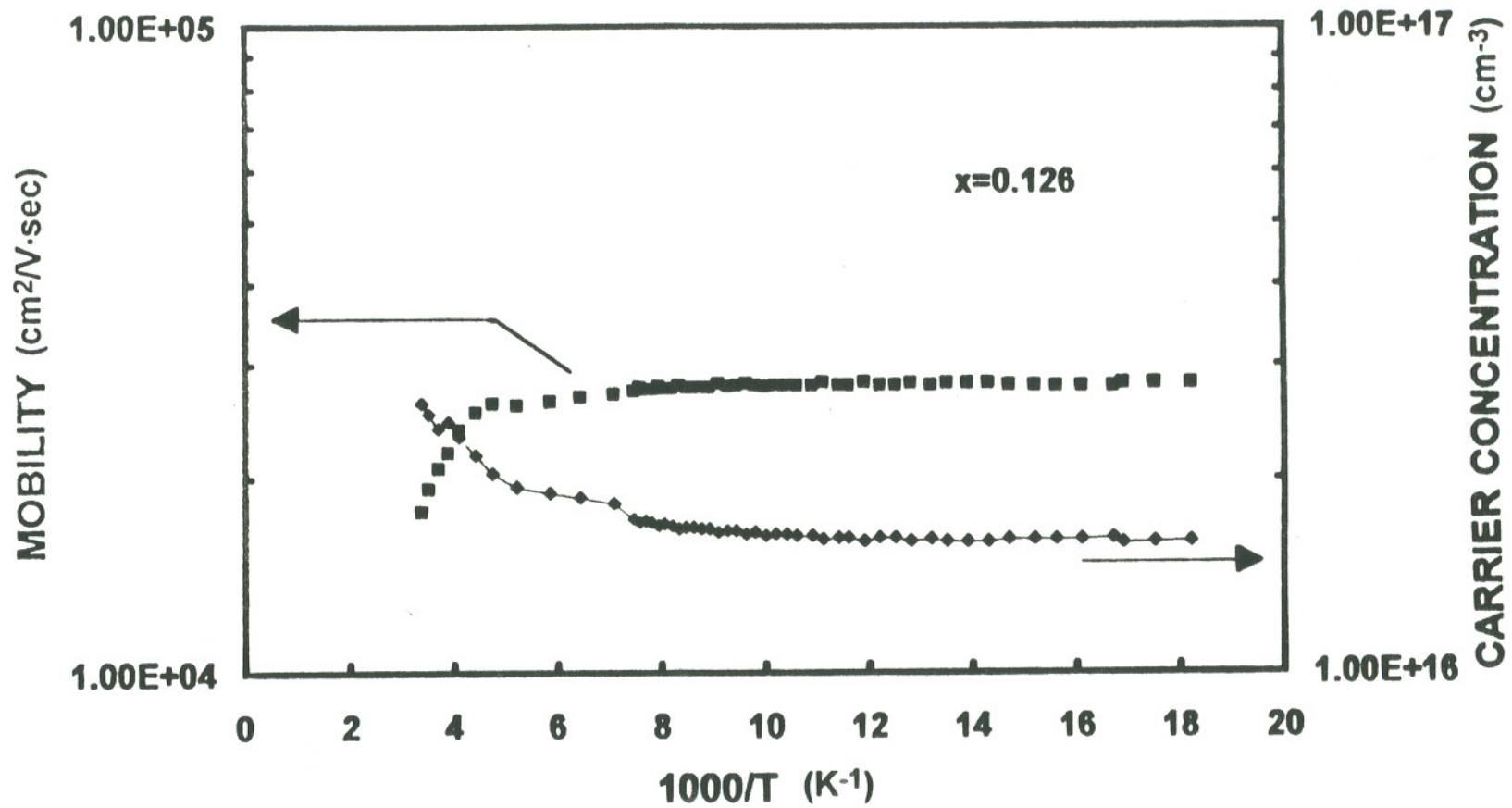


Figure 5.24 The Hall mobility and the Hall carrier concentration as a function of reciprocal temperature for *n*-type  $\text{Hg}_{1-x}\text{Cd}_x\text{Te}$  ( $x=0.126$ ) sample.

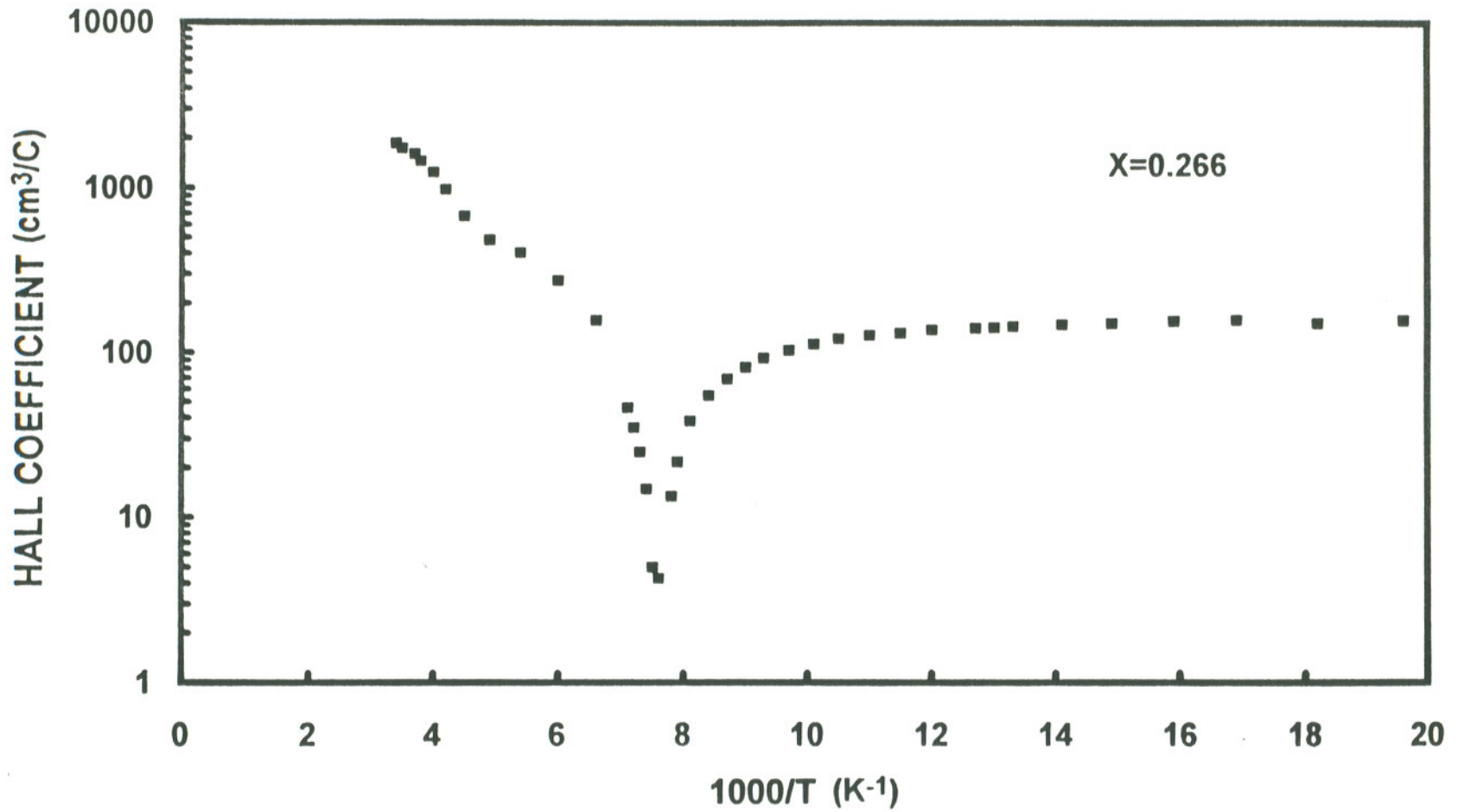
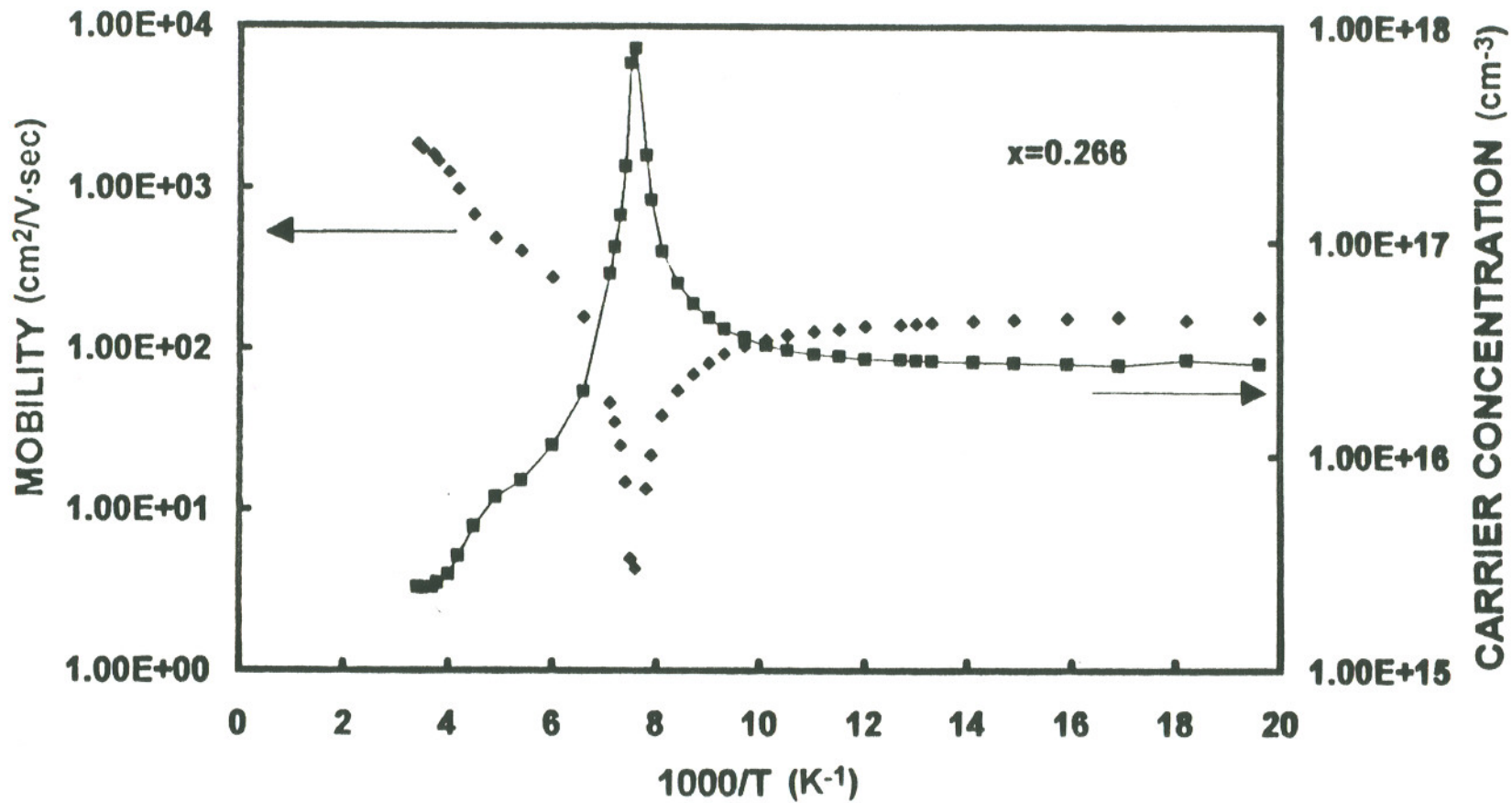


Figure 5.25 The Hall coefficient  $R_H$  as a function of reciprocal temperature for  $p$ -type  $Hg_{1-x}Cd_xTe$  ( $x=0.266$ ) sample.



**Figure 5.26** The Hall mobility and the Hall carrier concentration as a function of reciprocal temperature for *p*-type  $\text{Hg}_{1-x}\text{Cd}_x\text{Te}$  ( $x=0.266$ ) sample.

The electrical data on  $\text{Hg}_{1-x}\text{Cd}_x\text{Te}$  grown in the ARIIV reactor OMVPE system are summarized in Table 5.1. These data indicate that the n- or p-type behavior of  $\text{Hg}_{1-x}\text{Cd}_x\text{Te}$  layers is attributable to a number of factors: 1) the use of a low growth temperature of  $\text{Hg}_{1-x}\text{Cd}_x\text{Te}$  crystals results in a low concentration of Hg vacancies, which are acceptors, and 2) the lattice mismatch and subgrains in the CdTe substrate result in defects that are active and probably *n*-type, as evidenced by the low value of mobility and the higher carrier concentrations.

**Table 5.1** Electrical data of  $\text{Hg}_{1-x}\text{Cd}_x\text{Te}$  grown by cold wall, pyrolytic OMVPE.

sample #	$Q_{\text{H}_2\text{-DMCd}}$ (sccm)	composition ( $x$ )	thickness ( $\mu\text{m}$ )	type	mobilities ( $\text{cm}^2/\text{V}\cdot\text{s}$ )	carr. cont. ( $\text{cm}^{-3}$ )
mct-ct35	0.6	0.126	5	n	$1.8 \times 10^4$ (300 K) $2.7 \times 10^4$ (77 K)	$2.5 \times 10^{16}$ (300 K) $1.7 \times 10^{16}$ (77 K)
mct-ct47	0.6	0.352	4	n	?	$7.0 \times 10^{16}$ (300 K)
mct-ct46	0.9	0.152	4	n	$2.0 \times 10^4$ (77 K)	$4.0 \times 10^{15}$ (77 K)
mct-ct36	1.2	0.126	4	n	$2.5 \times 10^4$ (300 K) $4.1 \times 10^4$ (77 K)	$6.2 \times 10^{16}$ (300 K) $2.6 \times 10^{16}$ (77 K)
mct-ct37	1.2	0.266	3	p	$1.8 \times 10^3$ (300 K) $1.5 \times 10^2$ (77 K)	$2.6 \times 10^{15}$ (300 K) $2.7 \times 10^{16}$ (77 K)
mct-ct45	1.8	?	4		?	?
mct-ct41	2.4	0.288	1.2	p	$1.4 \times 10^3$ (300 K)	$2.3 \times 10^{16}$ (300 K)
mct-ct43	3.6	0.297	0.9	p	$2.1 \times 10^3$ (300 K)	$1.7 \times 10^{16}$ (300 K)

## 6. CONCLUSIONS

With a new ARIIV reactor a breakthrough in the composition and the thickness uniformities of  $\text{Hg}_{1-x}\text{Cd}_x\text{Te}$  epilayers by the DAG process OMVPE was achieved for the first time.

The epilayer growth performance of the ARIIV reactor using  $\text{DMCd}$ ,  $\text{MATE}$ , and elemental  $\text{Hg}$  as OMVPE reactant sources was characterized by growth rate and surface morphology studies for  $\text{CdTe}$  and  $\text{HgTe}$  epilayers.

Optimum flow rates, substrate temperature, and reactor conditions were experimentally determined for  $\text{Hg}_{1-x}\text{Cd}_x\text{Te}$  epilayer growth at  $300\text{ }^\circ\text{C}$ ; where,  $T_s$  was determined by the cracking properties of  $\text{MATE}$  alkyl. The thickness and compositional uniformities of  $16\text{ cm}^2$   $\text{Hg}_{1-x}\text{Cd}_x\text{Te}$  epilayers were better than  $\pm 2\%$  and  $\pm 0.002$  in  $x$ , respectively.

The Hall effect measurements on as-grown  $\text{Hg}_{1-x}\text{Cd}_x\text{Te}$  showed  $n$ -type characteristics for less than  $x=0.25$  and  $p$ -type characteristics for greater than  $x=0.25$ . The electron carrier concentrations and the electron mobilities for  $n$ -type  $\text{Hg}_{1-x}\text{Cd}_x\text{Te}$  materials were in the range  $(0.4 - 2.6) \times 10^{16}\text{ cm}^{-3}$  and  $(2.0 - 4.1) \times 10^4\text{ cm}^2/\text{V.s}$ , respectively, at  $77\text{ K}$ . The higher value of electron concentrations and the lower value of electron mobilities for  $n$ -type  $\text{Hg}_{1-x}\text{Cd}_x\text{Te}$  were due to the subgrain boundaries in the available  $\text{CdTe}$  substrates.

## 7. BIBLIOGRAPHY

1. J.B. Mullin, S.J. Irvine, and D.J. Ashen, *J. Cryst. Growth* **55**, 92 (1981).
2. J.B. Mullin and S.J. Irvine, *J. Phys. D* **14**, L149 (1981).
3. J.B. Mullin and S.J. Irvine, *J. Vac. Sci. Technol.* **21**, 178 (1982).
4. P. Knowles, GEC, *J. Research* **2**, 141 (1982).
5. J.T. Longo, D.T. Cheung, A.M. Andrews, C.C. Wang, and J.M. Tracy, *IEEE Transactions on Electronic Devices* **Ed-25**, 213 (1978).
6. P. Capper, C.L. Jones, E.J. Pearce, and M.J.T. Quelch, *J. Cryst. Growth* **62**, 487 (1983).
7. C.L. Jones, P. Capper, J.J. Gosney, G. Ard, and I. Kenworthy, *J. Cryst. Growth* **64**, 403 (1983).
8. J.C. Clayton, M.C. Davidson, D.C. Gillics, and S.L. Lehoczky, *J. Cryst. Growth* **60**, 374 (1982).
9. M.J. Brau, *U. S. Patent #* 3 656 944 (1972).
10. R. Triboulet, T. Nguyen Duy, and A. Durand, *J. Vac. Sci. Technol.* **A 3** (1), 95 (1985).
11. R.B. Maciolek and C.J. Speerschneider, *U. S. Patent #* 3 902 924 (1975).
12. G.W. Manley, P.S. McDermott, E.S. Pan, and R.J. Riley, *U. S. Patent #* 3 619 282 (1971).
13. S.J. Irvine and J.B. Mullin, *J. Cryst. Growth* **55**, 107 (1981).
14. W.F. Lawson, S. Nielson, E.H. Putly, and A.S. Young, *J. Phys. Chem. Solids* **9**, 325 (1959).
15. E.O. Kane, *Semiconductors and Semimetals, The k.p method*, **Vol.1**, Academic Press, New York, (1966).
16. D. Long, *Energy Bands in Semiconductors*, Wiley, New York, (1968).

17. G.L. Hansen, J.L. Schmit, and T.N. Casselman, *J. Appl. Phys.* **53**, 7099 (1982).
18. J. Brice and P. Capper, *Properties of Mercury Cadmium Telluride, EMIS Datareviews Series 3*, Inspec, New York, (1987).
19. Keun-Mook Kim, Ph.D thesis, Yonsei University, Seoul (1987).
20. D. Long and J.L. Schmit, *Mercury Cadmium Telluride and Closely Related Alloys, Semiconductors and Semimetals Vol 5*, Academic Press, New York (1970).
21. J.C. Wooley and B. Ray, *J. Phys. Chem. Solids* **13**, 151 (1960).
22. W.F.H. Mickelthwait, *The Crystal Growth of Cadmium Mercury Telluride, Semiconductors and Semimetals, Vol. 18*, Academic Press, New York, (1981).
23. D. Kranzer, *J. Phys. Chem. Solids* **34**, 9 (1973).
24. S.H. Shin, M. Chu, A.H.B. Vanderwyck, M. Lanir, and C.C. Wang, *J. Appl. Phys.* **51**, 3772 (1980).
25. P. Capper, *J. Cryst. Growth* **57**, 280 (1982).
26. L.F. Lou and W.H. Rrye, *J. Appl. Phys.* **56**, 2253 (1984).
27. W. Scott and R.J. Hager, *J. Appl. Phys.* **42**, 803 (1971).
28. Y.G. Arapov, B.B. Ponikarov, I.M. Tsidikovskii, and N.G. Schelushinina, *Sov. Phys. Semicond.* **13**, 1126 (1979).
29. J.B. Mullin, A. Royle, J. Giess, J.S. Gough, and S.J.C. Irvine, *J. Cryst. Growth* **77**, 460 (1986).
30. J.R. Dixon, *J. Appl. Phys.* **30**, 1412 (1959).
31. G.L. Hansen and J.L. Schmit, *J. Appl. Phys.* **54**, 1639 (1983).
32. A. Zemel, A. Sher, and D. Eger, *J. Appl. Phys.* **62** (5), 1861 (1988).
33. P.W. Kruse, *Semiconductors and Semimetals-Mercury Cadmium Telluride*, Academic Press, New York, pp 572-577 (1981).

34. J.L. Schmit and C.J. Speerscheider, *Infrared Physics* **8**, 247 (1968).
35. K. Shinohara, R. Ueda, O. Ohtsuki, and Y. Ueda, *Jpn. J. Appl. Phys.* **11**, 273 (1972).
36. B.E. Bartlett, P. Capper, J.E. Harris, and M.J.T. Quelch, *J. Cryst. Growth* **46**, 623 (1979).
37. B. E. Bartlett, P. Capper, J.E. Harris, and M.J.T. Quelch, *J. Cryst. Growth* **47**, 341 (1979).
38. T.C. Harman, *J. Electron. Mater.* **2** (1), 230 (1972).
39. G.A. Wolf and A.I. Mlavsky, *Crystal Growth, Ed. C.H.L. Goodman Vol. 1*, Plenum, New York, 193 (1974).
40. R. Triboulet, T. Nguyen-Duy, and A. Durand, *J. Vac. Sci. Technol.* **A 3**(1), 95 (1985).
41. K.M. Kim, S.R. Hahn, S.K. Noh, H.L. Park, and C.H. Chung, *J. Mat. Sci. Lett.* **6**, 1205 (1987).
42. J. Reno, I.K. Sou, P.S. Wijewarnasuriya and J.P. Faurie, *Appl. Phys. Lett.* **47**, 1168 (1985).
43. J.P. Faurie, J. Reno, S. Sivananthan, I.K. Sou, X. Chu, M. Boukerche, and P.S. Wijewarnasuriya, *J. Vac. Sci. Technol.* **A 4**, 2067 (1986).
44. K.A. Harris, S. Hwang, Y. Lansari, R.P. Burns, J.W. Cook Jr, and J.F. Schetzina, *J. Vac. Sci. Technol.* **B 5**, 699 (1987).
45. X. Chu, S. Sivananthan, and J.P. Faurie, *Appl. Phys. Lett.* **50**, 597 (1987).
46. K.A. Harris, S. Hwang, Y. Lansari, J.W. Cook Jr, J.F. Schetzina, and M. Chu, *J. Vac. Sci. Technol.* **A 5**, 3085 (1987).
47. J.D. Murphy, *Proc.SPIE* **659**, 2 (1986).
48. F. Bailly, G. Cohen-Solal, and Y. Marfaing, *C. R. Acad. Sci., Paris* **257**, 103 (1963).
49. G. Cohen-Solal, Y. Marfaing, and F. Bailly, *Rev. Phys. Appl.* **1**, 11 (1966).

50. W.E. Hoke and P.J. Lemonias, *Appl. Phys. Lett.* **46(4)**, 398 (1985).
51. J. Tunncliffe, S.J.C. Irvine, O.D. Dosser, and J.B. Mullin, *J. Cryst. Growth* **68**, 245 (1984).
52. G.N. Pain, C. Sandford, G.K.G. Smith, L.S. Wielunski, S.P. Russo, G.K. Reeves, and R. Elliman, *J. Cryst. Growth* **107**, 610 (1991).
53. G. Cinader, A. Raizman, and A. Sher, *J. Vac. Sci. Technol.* **B 9**, 1634 (1991).
54. W.E. Hoke, P.J. Lemonias, and R. Taczewski, *Appl. Phys. Lett.* **45**, 1092 (1984).
55. J.L. Schmit, *J. Vac. Sci. Technol.* **A 3**, 89 (1985).
56. S.K. Ghandi and I. Bhat, *Appl. Phys. Lett.* **44**, 779 (1984).
57. N.W. Cody, Ph.D thesis, Oregon Graduate Institute, Beaverton, OR (1992).
58. N.R. Tasker, I.B. Bhat, K.K. Parat, D. Terry, H. Ehsani, and S.K. Ghandi, *J. Vac. Sci. Technol.* **A 7**, 281 (1989).
59. R. Korenstein, P. Hallock, B. MacLeod, W. Hoke, and S. Oguz, *J. Vac. Sci. Technol.* **A 8**, 1039 (1990).
60. D.D. Edwall, J. Bajaj, and E.R. Gertner, *J. Vac. Sci. Technol.* **A 8**, 1045 (1990).
61. W.E. Hoke, P.J. Lemonias, and R. Korenstein, *J. Mater. Res.* **3**, 329 (1988).
62. R. Korenstein, W.E. Hoke, P.J. Lemonias, K.T. Higa, and D.C. Harris, *J. Appl. Phys.* **62**, 4929 (1987).
63. L.S. Lichtmann, J.D. Parsons, and E.H. Cirlin, *J. Cryst. Growth*, **86**, 217 (1988).
64. I.B. Bhat, H. Ehsani, and S.K. Ghandi, *J. Vac. Sci. Technol.* **A 8(2)**, 1054 (1990).
65. L.S. Lichtmann and J.D. Parsons, *U. S. Patent #. 4 828 938* (1989).
66. A.H. Dilawari and J. Szekely, *J. Cryst. Growth* **108**, 491 (1991).
67. J.D. Parsons, *J. Cryst. Growth* **16**, 387 (1992).

68. R.F.C Farrow, *J. Vac. Sci. Technol. A* **3**(1), 60 (1985).
69. R.S. Rosler and R.W. East, *U. S. Patent* #. 4 232 063 (1980).
70. T. Kusumoto, T. Hayashi, and S. Komiya, *Japan. J. Appl. Phys.* **24**, 620 (1985).
71. K. Nakagawe, K. Maeda, and S. Takeuchi, *Appl. Phys. Lett.* **34**, 574 (1979).
72. R.K. Bagai, G.L. Seth, and W.N. Borle, *J. Cryst. Growth* **91**, 605 (1988).
73. E.L. Polisar, N.M. Boinikh, G.V. Indenbaum, A.V. Vanyukov, and V.P. Shastlivin, *Izv. Vysshch. Uchebn. Zaved. Fiz.* **6**, 81 (1968).
74. J.I. Zvadanovich, L.J. Kusnezova, A.M. Sokolov, and J.G. Puchov, *SU patent HOIL 21/465*.
75. I. Hähnert and M. Schenk, *J. Cryst. Growth* **101**, 251 (1990).
76. S.K. Ghandhi, I.B. Bhat, H. Ehsani, D. Nucciarone, and G. Miller, *Appl. Phys. Lett.* **55**(2), 137 (1989).
77. Z.C. Feng, A. Mascarenhas, W.J. Choyke, R.F.C. Farrow, F.A. Shirland and W.J. Takei, *Appl. Phys. Lett.* **47**, 24 (1985).
78. W.J. Bartels and W. Nijman, *J. Cryst. Growth* **44**, 518 (1978).
79. W.E. Tennant, C.A. Cockrum, J.B. Gilpin, M.A. Kinch, M.B. Reine, and R.P. Ruth, *J. Vac. Sci. Technol. B* **10**(4), 1359 (1992).

## 8. VITA

The author was born on September 21, 1958 in Jeongju, Korea. He received the B.S. and the M.S. degree in physics from Chonnam National University, Kwangju, Korea, in 1981 and 1983, respectively. He served as the second lieutenant on active military duty as Korean Republican Army in 1983. His professional interests are in the field of semiconductor physics. He worked at the semiconductor laboratory of Yonsei University, Seoul, Korea, 1984-1987, as research assistant on  $\text{Hg}_{1-x}\text{Cd}_x\text{Te}$  bulk crystal growth program. In 1987, he enrolled at the Oregon Graduate Institute, where his research projects involved OMVPE growth of CdTe, HgTe, and  $\text{Hg}_{1-x}\text{Cd}_x\text{Te}$  epilayers.